

Alma Mater Studiorum – Università di Bologna

DOTTORATO DI RICERCA IN
INGEGNERIA BIOMEDICA, ELETTRICA E DEI SISTEMI

Ciclo XXX

Settore Concorsuale: 09/G2

Settore Scientifico Disciplinare: ING-INF/06

Computational modeling of human sinoatrial node:
what simulations tell us about pacemaking

Presentata da: Alan Fabbri

Coordinatore Dottorato

Prof. Daniele Vigo

Supervisore

Stefano Severi, PhD

Esame finale anno 2018

*Alla mia famiglia,
che mi ha sempre sostenuto*

Al nonno Lino

A Paola

*...e a chi, seppure in sei ore,
le maratone le finisce*

KEYWORDS

Cardiomyocytes

Computational models

Human sinoatrial node

Pacemaking modulation

Table of contents

GENERAL ABSTRACT	2
INTRODUCTION	5
PHD THESIS OUTLINE	8
REFERENCES	9
CHAPTER 1	
DEVELOPMENT OF THE SINGLE CELL HUMAN SINOATRIAL NODE ACTION POTENTIAL MODEL	10
ABSTRACT	11
1.1 INTRODUCTION	12
1.2 METHODS	15
1.2.1 MODEL DEVELOPMENT	15
1.2.2 AUTOMATIC OPTIMIZATION PROCEDURE	16
1.2.3 CELL CAPACITANCE AND DIMENSIONS	17
1.2.4 MEMBRANE CURRENTS	17
1.2.4.1 FUNNY CURRENT (I_F)	19
1.2.4.2 RAPID DELAYED RECTIFIER K^+ CURRENT (I_{KR})	19
1.2.4.3 SLOW DELAYED RECTIFIER K^+ CURRENT (I_{KS})	20
1.2.4.4 ULTRARAPID DELAYED RECTIFIER K^+ CURRENT (I_{KUR})	20
1.2.4.5 TRANSIENT OUTWARD K^+ CURRENT (I_{TO})	20
1.2.4.6 SODIUM/POTASSIUM PUMP CURRENT (I_{NAK})	21
1.2.4.7 SODIUM CURRENT (I_{NA})	21
1.2.4.8 T-TYPE CA^{2+} CURRENT (I_{CAT})	21
1.2.4.9 L-TYPE CA^{2+} CURRENT (I_{CAL})	21
1.2.4.10 SODIUM/CALCIUM EXCHANGE CURRENT (I_{NACA})	22
1.2.5 CALCIUM HANDLING	22
1.2.5.1 SR CA^{2+} UPTAKE (J_{UP})	22
1.2.5.2 SR CA^{2+} RELEASE (J_{REL})	23
1.2.5.3 CA^{2+} DIFFUSION AND CA^{2+} BUFFERS	23
1.2.6 ION CONCENTRATIONS	23
1.2.7 SENSITIVITY ANALYSIS	24
1.2.8 CALIBRATION OF THE POPULATION OF MODELS	24
1.2.9 HARDWARE AND SOFTWARE	25

1.3 RESULTS	26
HUMAN SAN MODEL BEHAVIOUR IN BASAL CONDITIONS	26
1.3.1 SIMULATED AP AND CALCIUM TRANSIENT	26
1.3.2 IONIC CURRENTS DURING THE DD PHASE	30
1.3.3 SENSITIVITY ANALYSIS	31
1.3.4 CALIBRATION OF THE POPULATION OF MODELS	35
1.4 DISCUSSION	36
1.4.1 CONSTRUCTION OF THE MODEL	37
1.4.2 SENSITIVITY ANALYSIS AND CALIBRATION OF THE POPULATION OF MODELS	38
1.5 LIMITATIONS AND FUTURE DEVELOPMENTS	39
REFERENCES	40
CHAPTER 2	
MODEL BASED ANALYSIS: EFFECTS OF I_f, Ca^{2+} HANDLING AND AUTONOMIC SYSTEM MODULATION OF PACEMAKING	45
ABSTRACT	46
2.1 INTRODUCTION	48
2.2 METHODS	51
2.2.1 BLOCKADE OF FUNNY CURRENT (I_f) AND Na^+/Ca^{2+} EXCHANGER CURRENT (I_{NaCa})	51
2.2.2 AUTONOMIC MODULATION	51
2.3 RESULTS	52
2.3.1 CONTRIBUTION OF I_f TO PACEMAKING	52
2.3.2 CONTRIBUTION OF I_{NaCa} TO PACEMAKING AND SPONTANEOUS CALCIUM OSCILLATIONS	54
2.3.3 AUTONOMIC MODULATION OF PACEMAKING	56
2.4 DISCUSSION	60
REFERENCES	63
CHAPTER 3	68
MODEL VALIDATION THROUGH THE SIMULATION OF ION CHANNEL MUTATIONS	68
ABSTRACT	69
3.1 INTRODUCTION	70
3.2 METHODS	72
3.2.1 FUNCTIONAL EFFECTS OF MUTATIONS	72
3.2.2 HCN4 MUTATIONS AND AUTONOMIC MODULATION	73

3.3 RESULTS	78
3.3.1 MODEL VALIDATION THROUGH THE SIMULATION OF ION CHANNEL MUTATIONS	78
3.3.2 EFFECTS OF I_f MUTATIONS	80
3.3.3 <i>HCN4</i> MUTATIONS AND AUTONOMIC MODULATION	81
3.3.4 EFFECTS OF I_{Na} MUTATIONS	83
3.3.5 EFFECTS OF I_{Ks} MUTATIONS	85
3.4 DISCUSSION	86
3.4.1 <i>HCN4</i> MUTATIONS	86
3.4.2 <i>SCN5A</i> MUTATIONS	87
3.4.3 <i>KCNQ1</i> MUTATIONS	88
3.4.4 GENERAL REMARKS	88
REFERENCES	89
CHAPTER 4	93
<u>EFFECTS OF THE SMALL AND LARGE CONDUCTANCE CALCIUM-ACTIVATED POTASSIUM CURRENTS (I_{SK} AND I_{BK}) IN HUMAN SINOATRIAL NODE</u>	93
ABSTRACT	94
4.1 INTRODUCTION	95
4.2 METHODS	97
4.2.1 MATHEMATICAL DESCRIPTION OF I_{SK}	97
4.2.2 MATHEMATICAL DESCRIPTION OF I_{BK}	99
4.2.3 OPTIMIZATION OF THE MODEL WHEN INCLUDING I_{SK}	101
4.3 RESULTS	102
4.3.1 EFFECTS OF I_{SK} ON AP AND CALCIUM TRANSIENT IN THE HUMAN SAN	102
4.3.2 EFFECTS OF I_{SK} ON AP AND CALCIUM TRANSIENT IN THE RABBIT SAN	104
4.3.3 EFFECTS OF I_{BK} ON AP AND CALCIUM TRANSIENT IN THE HUMAN SAN	106
4.3.4 EFFECTS OF I_{BK} ON AP AND CALCIUM TRANSIENT IN THE RABBIT SAN	107
4.3.5 COMBINING I_{SK} AND I_{BK} IN THE HUMAN AND IN THE RABBIT SAN	110
4.3.6 FEATURES AND PARAMETERS OF THE MODELS AFTER THE OPTIMIZATION PROCEDURE	113
4.4 DISCUSSION	118
4.4.1 EFFECTS OF THE INCLUSION OF I_{SK} IN HUMAN AND RABBIT SAN MODELS	118
4.2 EFFECTS OF THE INCLUSION OF I_{BK} IN HUMAN AND RABBIT SAN MODELS	120
4.3 COMBINING I_{SK} AND I_{BK} IN THE SAN MODELS	122
4.4 OPTIMIZED MODELS	122
4.5 FINAL REMARKS	122
REFERENCES	123

CHAPTER 5

PACE-AND-DRIVE OF THE HUMAN SINOATRIAL NODE

A PRELIMINARY COMPUTATIONAL INVESTIGATION	126
ABSTRACT	127
5.1 INTRODUCTION	128
5.2. METHODS	129
5.2.1 COUPLING OF DISCRETE SINOATRIAL NODE AND ATRIAL REGIONS	129
5.2.2 1D TISSUE STRAND	130
5.3 RESULTS	132
5.3.1 COUPLING OF DISCRETE SINOATRIAL NODE AND ATRIAL REGIONS	132
5.3.2 1D TISSUE STRAND	133
5.4 DISCUSSION	137
REFERENCES	139
GENERAL CONCLUSION	141
REFERENCES	145
APPENDIX 1: MODEL PARAMETERS AND EQUATIONS	146
MODEL PARAMETERS	146
CELL COMPARTMENTS	146
FIXED ION CONCENTRATIONS, mM	146
VARIABLE ION CONCENTRATIONS, mM	147
IONIC VALUES	147
SARCOLEMMA ION CURRENTS AND THEIR CONDUCTANCES	147
MODULATION OF SARCOLEMMA ION CURRENTS BY IONS	148
NA ⁺ /CA ²⁺ EXCHANGER (NACA) FUNCTION	148
CA ²⁺ DIFFUSION	148
SERCA PUMP	149
RYR FUNCTION	149
CA ²⁺ AND MG ²⁺ BUFFERING	149
MODEL EQUATIONS	150
MEMBRANE POTENTIAL	150
ION CURRENTS	150
HYPERPOLARIZATION-ACTIVATED, "FUNNY CURRENT" (I_F)	150
L-TYPE CA ²⁺ CURRENT (I_{CAL})	151
T-TYPE CA ²⁺ CURRENT (I_{CAT})	152
RAPIDLY ACTIVATING DELAYED RECTIFIER K ⁺ CURRENT (I_{KR})	153
SLOWLY ACTIVATING DELAYED RECTIFIER K ⁺ CURRENT (I_{KS})	154
<i>ACh</i> -ACTIVATED K ⁺ CURRENT ($I_{K,ACh}$)	154
<i>TRANSIENT OUTWARD</i> K ⁺ CURRENT (I_{TO})	155
NA ⁺ CURRENT (I_{NA})	156
NA ⁺ /K ⁺ PUMP CURRENT (I_{NAK})	157

NA ⁺ /CA ²⁺ EXCHANGER CURRENT (I_{NACA})	157
ULTRA-RAPID ACTIVATING DELAYED RECTIFIER K ⁺ CURRENT (I_{KUR})	158
CA ²⁺ RELEASE FLUX (J_{REL}) FROM SR VIA RYRS	159
INTRACELLULAR CA ²⁺ FLUXES	160
CA ²⁺ BUFFERING	160
DYNAMICS OF CA ²⁺ CONCENTRATIONS IN CELL COMPARTMENTS	161
RATE MODULATION EXPERIMENTS	162
APPENDIX 2: AUTOMATIC OPTIMIZATION PROCEDURE	163
PARAMETERS SELECTED FOR AUTOMATIC OPTIMIZATION	163
ACTION POTENTIAL FEATURES USED TO CONSTRAIN MODEL PARAMETERS	163
CALCIUM TRANSIENT FEATURES USED TO CONSTRAIN MODEL PARAMETERS	163
COST FUNCTION	164
SEARCH METHOD AND STOP CRITERION	165
PARAMETER CONSTRAINING	165
RINGRAZIAMENTI	167
ACKNOWLEDGMENTS	170

General Abstract

This PhD dissertation deals with the mathematical modeling of the electrophysiology of cardiac cells, in particular the human sinoatrial node (SAN).

The SAN is the primary pacemaker in physiological conditions. To carry out this function, SAN tissue is characterized by auto-rhythmicity, i.e. it does not need external stimuli to initiate the electrical signal that must be spread out through the whole heart. At the single cell level, the auto-rhythmic behavior is due to the spontaneous slow depolarization during the diastolic phase. Understanding the biophysical mechanisms at the base of diastolic depolarization (DD) is crucial to modulate the heart rate (HR). In turn, HR modulation is fundamental to treat cardiac arrhythmias, so that atria and ventricles can fill properly and pump the blood into the cardiovascular system.

The overall aim of this PhD thesis is the investigation of the underlying mechanisms that are responsible for the pacemaking in human. To this end, a human computational model of the action potential (AP) of the SAN was developed.

The faced fields of interest concerned:

- Pacemaking modulation at single cell level
- Effects of ion channel mutations on the beating rate
- Propagation of the electrical trigger from SAN to atrial tissue

The human single cell SAN model was developed starting from the state-of-art rabbit SAN by Severi *et al.*; the parent model was updated with experimental data and automatic optimization in order to match the AP features reported in literature. A sensitivity analysis was then performed in order to identify the most influencing parameters.

The investigation of pacemaking modulation was carried out through the simulation of current blockade and mimicking the stimulation of the autonomic nervous system.

The model was validated comparing the simulated electrophysiological effects due to ion channel mutations on beating rate with clinical data of symptomatic subjects carriers of the mutation.

More insights on pacemaking mechanisms were obtained thanks to the inclusion of calcium-activated potassium currents, which link changes in the intracellular calcium to the membrane.

Finally, the propagation of the action potential from the SAN to the atrial tissue and the source-sink interplay was investigated employing a mono-dimensional strand composed by SAN and atrial computational model.

The human SAN model developed in this dissertation showed the main AP features in agreement with the experimental data reported in literature and allowed to provide insights about the modulation of the beating rate, and thus, the macroscopic heart rate. The human SAN model developed in this dissertation showed the main AP features in agreement with the experimental data reported in literature and allowed to provide insights about the modulation of the beating rate, and thus, the macroscopic heart rate.

The effects of ion channels mutations affecting the “funny current”, the sodium current, and the slowly delayed rectifier potassium current simulated by the SAN model were consistent with the variations of heart rate observed in clinical studies. The validation, therefore, stated that the model provides a reliable description of SAN activity and represents an useful tool for scientific community.

The investigation of underlying mechanisms of pacemaking highlighted the capability of I_f to finely control the diastolic depolarization; furthermore it contributed to autonomic modulation with $I_{K,ACh}$ and I_{CaL} for the vagal and adrenergic stimulation respectively.

The inclusion of I_{SK} showed the capability of that current to affect diastolic depolarization in a relevant manner, especially when present in large amount. On

the contrary, the contribution of I_{BK} in beating rate modulation was almost negligible.

The carried out study about electrical conduction highlighted the capability of human SAN model of successfully driving the atrial tissue for a wide range of coupling. The extent of that range was dependent by the number of SAN cells that compose the electrical source. The presence of an electrical load, due to the atrial tissue, revealed that the model can show, with the same set of parameters, “central cell” and “peripheral cell” morphology thanks to the activity of I_{Na}

Several results here proposed have to be meant as predictions since human specific experimental data are still scarce. In this way the human computational AP model can be used as useful tool to gain knowledge about pacemaking phenomena, through the interaction between experiments and modeling.

Introduction

The sinoatrial node (SAN) is the primary pacemaker, responsible for the heart rate in physiological conditions. In other words, it is what keeps the heart ticking.

Galen (129-200 A.D.) first, and twelve centuries later Leonardo da Vinci (Noble, 1966; Opthof, 1988) described the auto-rhythmicity of the heart. However only in 1907 the SAN was anatomically identified as “*a small condensed area of tissue, just where the cava sank into the auricle*” by Sir Arthur Keith and Martin Flack (Keith & Flack, 1907); four years later, in 1911, SAN was indicated as the point of the initial cardiac stimulation (Monfredi *et al.*, 2010).

SAN cells are electrical specialized myocytes, i.e. they carry out the task of generating and spreading out the electrical impulse to the whole heart. This particular function makes the action potential (AP) waveform of SAN, its “electrical signature”, profoundly different from the one of working myocytes, as atrial and ventricular cells. When they are not stimulated, working myocytes show stable negative resting potential, whereas SAN cells are characterized by an unstable diastolic phase, that makes the membrane potential to slowly move to less negative (depolarized) values. This characteristic phase of pacemaker cells is called spontaneous diastolic depolarization (DD).

The main characteristic of SAN cells is their auto-oscillating nature, i.e. they do not need any external stimulus to trigger the AP. The spontaneous DD is driven by a small inward current, result of a sophisticated balance of several inward and outward currents. The “Funny current” (I_f), the transient, long lasting calcium currents (I_{CaT} and I_{CaL}) and the sodium-calcium (Na^+Ca^{2+}) exchanger (I_{NaCa}) contribute to the depolarization, carrying sodium (Na^+) and calcium (Ca^{2+}) into the cell, whereas outward potassium (K^+) currents, as the rapid (I_{Kr}) and the slow delayed rectifier (I_{Ks}) participate to the repolarization. A stronger contribution of inward currents shortens the duration of DD thus allowing a faster rate of the spontaneous APs. On the other hand, a stronger outward current causes a DD prolongation, which leads to a slower rate.

The pharmacological modulation of the heart rate is used in clinical practice to treat cardiac arrhythmias. Current blockers are chemical species able to reduce the activity of ion channels: by targeting the currents involved during DD it is possible to control its steepness, and thus its duration. Electrophysiological studies and clinical trials showed the capability of ivabradine, a I_f blocker, to slowdown the heart beat without any side-effect thanks to its high selectivity (see the BEAUTIFUL study).

The experimental quantification of current contributions during DD is often a challenging task: ion channel blockers can often affect more than one target and several unpredictable interactions can occur. Mathematical and computational modeling, thanks to simplification and abstraction, can help to disclose and to describe quantitatively the mechanisms in biophysical systems.

The first mathematical description of the rhythmicity of the heart was formulated by van der Pol and van der Mark (1928). Such model was able to reproduce the key properties of nerves and heart cells as excitable elements, i.e. the stimulus threshold, the membrane excitability and refractoriness. The main conceptual limit is the absence of a link between the electrical activity and the underlying biophysical phenomena.

The investigation on the squid giant axon carried out by Hodgkin & Huxley (1952) represents a milestone in electrophysiology and AP modeling. They represented the behavior of the cellular membrane and ion channels as the behavior of an electrical circuit composed by a capacitance in parallel to a variable conductance; the variation of the membrane voltage is proportional to the sum of the inward and outward currents. The time- and voltage-dependent conductance of ion channels was achieved through the activation and inactivation of gating variables, described by differential equations. In this way, Hodgkin & Huxley (1952) were the firsts who linked the flux of Na^+ and K^+ through the membrane to the electrical activity of the cell.

The Hodgkin-Huxley paradigm was then extended to cardiac excitable cells. The Purkinje fibers model by Noble (1960, 1962) was the first cardiac computational model. Several years after, Yanagihara & Irisawa (1980) published the first computational model based on rabbit SAN electrophysiological data.

The refinement of electrophysiological measurements and cell preparation techniques (e.g. the capability of measuring single currents, to obtain isolated cells) allowed investigating more in details the mechanisms of pacemaking and formulating more comprehensive models, by introducing new current formulations and ionic concentration dynamics.

In spite of the abundance of *in vitro* data, the principal mechanism responsible for the initiation and modulation of the heartbeat is still debated.

The “Membrane clock” theory is the most consolidated one with strong experimental evidences that support it. Recently, the “Ca²⁺ clock” theory was proposed. On one hand, the “Membrane clock” theory confers the primary role in membrane automaticity and pacemaking modulation to ion channels, especially to I_f. Indeed, the biophysical properties of I_f (e.g. activation at potentials compatible with DD, inward contribution, enhancement in β-adrenergic stimulation), make it a strong candidate to the spontaneous DD initiation and modulation. On the other hand, the “Calcium clock” theory is based on the spontaneous release of Ca²⁺ from the sarcoplasmic reticulum. Ca²⁺ cycling is able to change the membrane voltage through the ignition of the Na⁺-Ca²⁺ exchanger. The experimental and computational work by Himeno *et al.*, (2011) highlighted that the chelation of cytosolic Ca²⁺, and thus an impairment of Ca²⁺ clock did not affect the heart rate in guinea pig SAN, suggesting a predominant role of “membrane clock”.

The state-of-the-art models (Maltsev & Lakatta, 2009; Himeno *et al.*, 2011; Severi *et al.*, 2012) are based on plethora of animal experimental data (in particular rabbit and guinea pig) and they allow to describe relevant phenomena; unfortunately, way less data are available on human SAN cells. Such shortage of human data is because, usually failing explanted hearts do not contain the SAN, since it remains inside the chest of the receiver of the new functional heart during transplantation. The unique electrophysiological work on adult human SAN was carried out by Verkerk *et al.* (2007), whereas Chandler *et al.* (2009) characterized the human SAN through gene expression, quantifying the mRNA in SAN cells. In this way, the limited availability of human specific data hampered the development of a computational model of human SAN.

Mathematical modeling provides a simplification and abstraction to the description of biophysical phenomena, and can be exploited as a white box to observe the mechanisms that are responsible for the emergent behavior. Cardiac cells are strongly non-linear dynamical systems and often it is challenging to predict or explain the effects consequent to drug administration or blockade of currents.

The lack of human electrophysiological data for SAN is a critical obstacle to the formulation of a comprehensive human specific model. Luckily, optimization techniques represent useful tools to fill this gap of knowledge, using the available experimental data as a tight constraints.

The development of a human SAN model, based on the human-specific available current formulations could allow to “dissect” the net current in all its components, providing an estimation of the contribution to pacemaking of each current.

The knowledge about the mix of currents during DD can therefore help to identify pharmacological targets to modulate the heart rate, the macroscopic marker used in clinical practice.

The overall aim of this PhD dissertation is the investigation of the underlying pacemaking mechanisms involved in the human SAN.

To this end, a computational human SAN single cell model able to reproduce (i) the experimental data in physiological conditions, (ii) the effects of administration of drugs, and (iii) the changes in beating rate, due to ion channel mutations, was developed.

PhD Thesis Outline

The first step to investigate the mechanisms at the base of human pacemaking was the development of the mathematical AP model of human SAN at the single cell level (**Chapter 1**). The rabbit SAN model by Severi *et al.* (2012), was

adopted as parent model. It was updated using (i) electrophysiological human specific data, (ii) gene expression mRNA quantities to scale ion channel conductance; (iii) an automatic optimization procedure was performed to tune parameters on which no experimental data were available. The simulated waveform and the extracted features were compared to experimental data. A sensitivity analysis was then carried out in order to identify the parameters that mostly influence the behavior of the AP model.

In **Chapter 2** the impact on heart rate due to the modulation of the two main actors of “membrane clock” and “calcium clock” theories, namely I_f and I_{NaCa} was investigated. Moreover, the effects of autonomic stimulation were assessed simulating the effects due to the administration of acetylcholine (vagal stimulation) and isoprenaline (to mimic the adrenergic stimulation).

The validation of the model was performed reproducing the effects on beating rate of ion channel mutations (**Chapter 3**). To this end, the electrophysiological characterization of a selection of mutation affecting I_f , the fast Na^+ current (I_{Na}) and I_{Ks} were implemented in the SAN model. Furthermore the effects of three mutations affecting I_f (G480R, A485V and 695X) were assessed at low, basal and high rates.

In **Chapter 4** the impact of the inclusion of new currents was investigated. The small (I_{SK}) and large conductance (I_{BK}) K^+ Ca^{2+} -dependent currents were added to the original model and a preliminary sensitivity analysis was performed

Finally, the focus was moved on how the SAN impulse spread out, investigating how a small tissue as SAN can drive a larger one as atrial tissue (**Chapter 5**). A mono-dimensional strand composed by SAN and atrial cells was built and a study of the propagation of the electrical stimulus was carried out varying the strength of electrical coupling and the number of SAN and atrial cell mix.

References

Himeno Y, Toyoda F, Satoh H, Amano A, Cha CY, Matsuura H & Noma A (2011). Minor contribution of cytosolic Ca^{2+} transients to the pacemaker rhythm in guinea pig sinoatrial node cells. *Am J Physiol - Heart Circ Physiol* 300, H251–H261.

- Hodgkin AL & Huxley AF (1952). A quantitative description of membrane current and its application to conduction and excitation in nerve. *J Physiol* 117, 500–544.
- Keith A & Flack M (1907). The Form and Nature of the Muscular Connections between the Primary Divisions of the Vertebrate Heart. *J Anat Physiol* 41, 172–189.
- Maltsev VA & Lakatta EG (2009). Synergism of coupled subsarcolemmal Ca²⁺ clocks and sarcolemmal voltage clocks confers robust and flexible pacemaker function in a novel pacemaker cell model. *Am J Physiol - Heart Circ Physiol* 296, H594–H615.
- Monfredi O, Dobrzynski H, Mondal T, Boyett MR & Morris GM (2010). The Anatomy and Physiology of the Sinoatrial Node—A Contemporary Review. *Pacing Clin Electrophysiol* 33, 1392–1406.
- Noble D (1960). Cardiac Action and Pacemaker Potentials based on the Hodgkin-Huxley Equations. *Nature* 188, 495.
- Noble D (1962). A modification of the Hodgkin—Huxley equations applicable to Purkinje fibre action and pacemaker potentials. *J Physiol* 160, 317–352.
- Noble D (1966). The initiation of the heart beat. *Adv Sci* 23, 412–418.
- Opthof T (1988). The mammalian sinoatrial node. *Cardiovasc Drugs Ther* 1, 573–597.
- Pol van der B & Mark van der J (1928). LXXII. The heartbeat considered as a relaxation oscillation, and an electrical model of the heart. *Lond Edinb Dublin Philos Mag J Sci* 6, 763–775.
- Severi S, Fantini M, Charawi LA & DiFrancesco D (2012). An updated computational model of rabbit sinoatrial action potential to investigate the mechanisms of heart rate modulation. *J Physiol* 590, 4483–4499.
- Verkerk AO, Wilders R, Borren MMGJ van, Peters RJG, Broekhuis E, Lam K, Coronel R, Bakker JMT de & Tan HL (2007). Pacemaker current (I_f) in the human sinoatrial node. *Eur Heart J* 28, 2472–2478.
- Yanagihara K & Irisawa H (1980). Potassium current during the pacemaker depolarization in rabbit sinoatrial node cell. *Pflüg Arch Eur J Physiol* 388, 255–260.

Chapter 1

Development of the single cell human sinoatrial node action potential model

The content of this chapter is published in:

“Computational analysis of the human sinus node action potential: model development and effects of mutations”

Alan Fabbri¹, Matteo Fantini¹, Ronald Wilders² and Stefano Severi¹

¹ Computational Physiopatology Unit, Department of Electrical, Electronic and Information Engineering “Guglielmo Marconi”, University of Bologna, Cesena, Italy

² Department of Anatomy, Embriology and Physiology, Academic Medical Center, University of Amsterdam, Amsterdam, The Netherlands

The Journal of Physiology, J Physiol 2017, 595 (7) 2365-2396

Abstract

The sinoatrial node (SAN) is the normal pacemaker of the mammalian heart. Over several decades, a large amount of data on the ionic mechanisms underlying the spontaneous electrical activity of SAN pacemaker cells has been obtained, mostly in experiments on single cells isolated from rabbit SAN. This wealth of data has allowed the development of detailed mathematical models of the electrical activity of rabbit SAN pacemaker cells.

The present study aimed to construct a comprehensive model of the electrical activity of a human SAN pacemaker cell using recently obtained electrophysiological data from human SAN pacemaker cells.

We based our model on the recent Severi–DiFrancesco model of a rabbit SAN pacemaker cell; updates of formulation concerning currents, pump and exchangers were implemented including electrophysiological and gene expression data collected from human SAN cells present in literature. The tuning of parameters of which no experimental data were available was carried out through an automatic optimization procedure. A sensitivity analysis was performed in order to identify the most influencing parameters on AP features.

The model showed AP features in accordance with experimental data (CL = 814 vs 828 ± 21 ms, $APD_{90} = 161.5$ vs 143.5 ± 49.3 ms, $DDR_{100} = 48.1$ vs 48.9 ± 25.4 mV/s) and qualitative reproduction of the experimentally observed calcium transient time course.

Sensitivity analysis highlighted a remarkable influence of I_{CaL} and I_{Kr} on AP waveform and AP duration, respectively.

1.1 Introduction

There is no need to explain the important role of the sinoatrial node (SAN) in cardiac function. Many studies have focused on this small but crucial piece of cardiac tissue and provided detailed knowledge of the physiological processes governing its function. Yet we still have an incomplete understanding of the cellular basis of the pacemaker activity of the SAN and, specifically, the degree of contribution of the different mechanisms involved is still debated (Lakatta & DiFrancesco, 2009; DiFrancesco, 2010; Lakatta, 2010; Maltsev & Lakatta, 2010; Noble *et al.*, 2010; Verkerk & Wilders, 2010; Himeno *et al.*, 2011; DiFrancesco & Noble, 2012; Lakatta & Maltsev, 2012; Rosen *et al.*, 2012; Monfredi *et al.*, 2013; Yaniv *et al.*, 2013, 2015).

To date, almost all experiments on SAN electrophysiology have been carried out on animals, particularly rabbits. These experiments have shed light on several aspects, such as characteristics of membrane currents, effects of ion channel blockers, calcium handling and beating rate modulation. This considerable amount of data has allowed the development of increasingly comprehensive and detailed action potential (AP) models (Wilders, 2007) subsequent to the first mathematical models reproducing pacemaker activity being created (McAllister *et al.*, 1975; Yanagihara *et al.*, 1980; Noble & Noble, 1984; DiFrancesco & Noble, 1985).

Recently, novel SAN AP models have been proposed, incorporating detailed calcium-handling dynamics and providing in-depth descriptions of the underlying events at the cellular level in guinea-pig, mouse and rabbit (Himeno *et al.*, 2008; Maltsev & Lakatta, 2009; Kharche *et al.*, 2011; Severi *et al.*, 2012).

However, the translation of animal data/models to humans is not straightforward (probably even less so for SAN pacemaker cells than working myocardial cells), given the big difference in their main ‘output’ (i.e. pacing rate) between human and laboratory animals.

Very few measurements are available for human SAN cells because failing explanted hearts, as obtained during heart transplantation, usually do not contain

the SAN region, which remains inside the receiver's chest. Drouin (1997) was the first to record human adult APs from SAN tissue, obtained from four subjects affected by left ventricle infarction. Ten years later Verkerk *et al.* (2007b) investigated the electrophysiological properties of three isolated SAN cells from a woman who underwent SAN excision because of a paroxysmal non-treatable tachycardia. They recorded APs and characterized the funny current using whole-cell patch clamp in current clamp and voltage clamp mode. In a subsequent study (Verkerk *et al.*, 2013), the same group reported further data from the same patient, regarding the calcium transient (CaT) measured by indo-1 fluorescent dye.

Some proof-of-concept attempts have been made to model spontaneous activity in human cardiac pacemaker cells. Seemann *et al.* (2006) presented the first human SAN AP model as part of a wider 3D model of human atria. Their model started from the model of Courtemanche *et al.* (1998) of the human atrial AP and achieved automaticity by including rabbit SAN currents (e.g. I_f , I_{CaT} , etc.), formulated in accordance with Zhang *et al.* (2000). Unfortunately, no reliable experimental comparisons could be made with the model of Seemann *et al.* (2006). Chandler *et al.* (2009) described the 'molecular architecture' of adult human SAN tissue obtained from healthy hearts, comparing it to the non-specialized tissue of the right atrium. They developed a SAN model, again starting from the model of Courtemanche *et al.* (1998); by scaling the maximal conductances based on mRNA data, they provided a proof of concept that automaticity can be the result of the specific gene expression pattern of human SAN tissue. However, some mechanisms were not included, and no quantitative AP features were computed or compared with the human data available at that time. Accordingly, as Chandler *et al.* (2009) themselves affirmed, 'the resulting model cannot be considered definitive and is a guide only'.

Recently, Verkerk & Wilders (2015) computationally investigated mutations affecting hyperpolarization-activated cyclic nucleotide-gated cation channel 4 (HCN4) channels, but they '... preferred to study I_f in simulated action potential clamp experiments, thus ensuring that the action potential followed the course of that of a human SAN pacemaker cell' because a human SAN AP model was not formulated yet. Thus, they highlighted the need for such a model.

Much more recent is the human SAN AP model formulated by Pohl *et al.* (2016). In their model, to investigate the cardiac neuromodulation (as exerted by vagal stimulation) that aims to reduce heart rate, they focused their attention on the effects that acetylcholine has on the rate. Starting from the rabbit SAN model reported by Dokos *et al.* (1996) they updated current formulations, integrating data from human SAN cells (Verkerk *et al.* 2007b) and human ion channels expressed in heterologous systems (HEK or tsA-201 cells, *Xenopus* oocytes, etc.). The simulated cycle length (CL) was in accordance with the experimental recordings of human SAN cell APs by Verkerk *et al.* (2007b) but, unfortunately, the AP morphology, both during the diastolic depolarization (DD) phase and AP, was very unlike that obtained experimentally.

The main aim of the present study is the formulation of a human SAN AP model strictly based on and constrained by the available electrophysiological data. We started from the recent rabbit SAN model by Severi *et al.* (2012), which integrates the two principal mechanisms that determine the beating rate: the ‘membrane clock’ and ‘calcium clock’ (Maltsev & Lakatta, 2009; Lakatta *et al.*, 2010). Several current formulations were updated based on available measurements. A set of parameters, for which no specific data were available, were tuned to reproduce the measured AP and calcium transient data. We then used the model to assess the effects of several mutations affecting heart rate and investigated the rate modulation in some relevant conditions (see Chapter 2 and 3).

1.2 Methods

1.2.1 Model development

The starting point of our work was the rabbit SAN cell model by Severi *et al.* (2012). Several currents, pumps and exchangers were reviewed, based on electrophysiological data from human SAN cells (Verkerk *et al.*, 2007b), self-beating embryonic human cardiomyocytes (Danielsson *et al.*, 2013), as selected for their automaticity, and data on gene expression patterns in SAN vs. atrial human cells (Chandler *et al.* 2009). Specifically, the model was constrained by: AP parameters obtained from three isolated human SAN pacemaker cells by Verkerk *et al.* (2007b); the voltage clamp data on I_f in the same three cells (Verkerk *et al.*, 2007b); the effect of 2 mM Cs^+ , as an I_f blocker, on the AP of a single isolated human SAN pacemaker cell (Verkerk *et al.* 2007b); and the Ca^{2+} transient data of a single isolated human SAN pacemaker cell (Verkerk *et al.*, 2013). For a small set of parameters for which no specific experimental data were available, values were obtained via an automatic optimization procedure (see below).

Figure 1.1 shows a schematic diagram of the human SAN AP model. The compartmentalization, essential for the calcium handling description, is inherited from the parent model, as were the sarcolemmal ionic currents, pumps and exchangers. The ultra-rapid delayed rectifier K^+ current (I_{Kur}) was developed independently. Table 1.1 reports the changes with respect to the rabbit SAN model and the rationale for each. All model equations and parameter values are provided in Appendix 1.

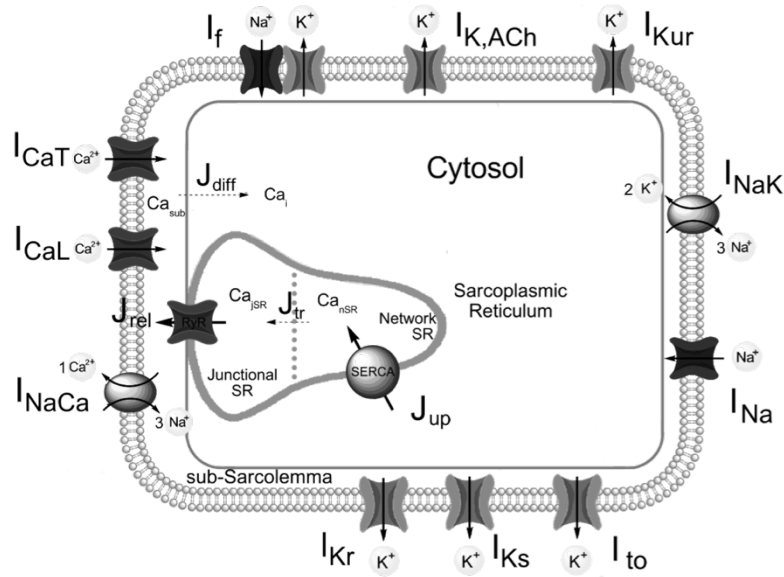


Figure 1.1: Schematic diagram of the human SAN cell model. The cell is divided in three compartments: sub-sarcolemma, cytosol, and sarcoplasmic reticulum (SR), which is subdivided in junctional and network SR. Ca^{2+} handling is described by: two diffusion fluxes (J_{diff} from the subsarcolemmal space to the cytosol and J_{tr} from the network SR to the junctional SR), the Ca^{2+} uptake from the cytosol into the network SR by the SERCA pump (J_{up}), and the Ca^{2+} release (J_{rel}) from the junctional SR into the subsarcolemmal space by the ryanodine receptors (RyRs). Sodium, calcium, and potassium ions pass the sarcolemmal membrane through 11 different ionic channels, pumps and exchangers, as indicated.

1.2.2 Automatic optimization procedure

An automatic optimization was performed to tune the parameters for which human experimental data were not available to fit the recorded AP and cytosolic calcium transient traces (Verkerk *et al.* 2007b, 2013).

The cost function of the optimization procedure was based on quantitative data on AP features [action potential amplitude (APA), maximum diastolic potential (MDP), cycle length (CL), maximum rate of rise of membrane potential $[(dV/dt)_{max}]$, action potential duration (APD₂₀, APD₅₀, APD₉₀), diastolic depolarization rate (DDR₁₀₀), intracellular calcium transients [diastolic $[\text{Ca}^{2+}]_i$, systolic $[\text{Ca}^{2+}]_i$, intracellular CaT duration (TD₂₀, TD₅₀, TD₉₀)] and the effect of the administration of 2 mM Cs^+ , a funny current blocker, on CL (Verkerk *et al.* 2007b, 2013). The most critical features (CL, MDP and CL prolongation in

response to Cs^+) were weighted more heavily. After each simulation, the set of quantitative descriptors was extracted and compared with the experimental data.

If a particular observed feature fell out of the experimental mean \pm SEM range, the contribution of this feature to the overall cost was increased in a linear way; otherwise, no handicap was added. The search for the optimal solution was conducted using the Nelder–Mead simplex method (Lagarias *et al.*, 1998).

The obtained parameters are shown in Table 1.1. Further details on the optimization procedure are reported in Appendix 2.

1.2.3 Cell capacitance and dimensions

We assumed a membrane capacitance (C_m) of 57 pF, and a cylindrical cell shape with a length of 67 μm and a diameter of 7.8 μm , in accordance with the experimental data of Verkerk *et al.* (2007b), who reported values of 56.6 ± 8.7 pF, 66.7 ± 6.3 μm and 7.8 ± 0.4 μm (mean \pm SEM, $n = 4$), respectively. The dimensions of the intracellular compartments, expressed as a percentage of cell volume, were adopted from the parent model.

1.2.4 Membrane currents

Here, we specify each of the sarcolemmal currents flowing through the ionic channels, pumps and exchangers shown in Fig. 1.1. The outward acetylcholine-activated potassium current $I_{K,ACh}$, will be described in Chapter 2, in the section related to the autonomic modulation. All membrane currents were scaled up by the new value of the cell capacitance, aiming to maintain the conductance densities adopted from the parent model. Changes to the conductance densities, as a result of parameter tuning, are reported in the corresponding current subsections.

Table 1.1 - Changes with respect to the parent model.

	Updates	Rationale
Cell Capacitance and dimensions	$C_m=57$ pF, $L_{cell}=67$ μm , $R_{cell}=3.9$ μm	Human SAN data (Verkerk <i>et al.</i> , 2007b)
I_f	New formulation	Human SAN data (Verkerk <i>et al.</i> , 2007b)
I_{Kr}	New steady-state activation, $g_{Kr}=+10\%$	Embryonic human data (Danielsson <i>et al.</i> , 2013)
I_{Ks}	New steady-state activation, $g_{Ks}=-78\%$	Embryonic human data (Danielsson <i>et al.</i> , 2013)
I_{Kur}	Added, $g_{Kur}=6\%$ of atrial Formulation from Maleckar <i>et al.</i> (2009) atrial cell model	Gene expression data (Chandler <i>et al.</i> , 2009) and automatic optimization (APD)
I_{to}	$g_{to}=-1.5\%$	Automatic optimization (OS)
$I_{K,ACh}$	$g_{K,ACh}=-77.5\%$	Fitting of ACh effects in rabbit
I_{NaK}	$g_{NaK}=-28\%$	Automatic optimization (CL)
I_{CaL}	$V_{\frac{1}{2},dL}=-16.45$ mV, $k_{dL}=4.32$ mV (dL gate) $P_{CaL}=+28.5\%$	Automatic optimization (CL)
I_{CaT}	$P_{CaT}=+15\%$	Automatic optimization (Early DD)
I_{NaCa}	$K_{NaCa}=-53\%$	Automatic optimization (diastolic $[Ca^{2+}]_i$)
SR uptake (J_{up})	Sigmoidal formulation	Fitting of diastolic $[Ca^{2+}]_i$
SR release (J_{rel})	$k_s=1.48 \cdot 10^8$ s ⁻¹ $k_{om}=660$ s ⁻¹	Automatic optimization (Ca _i range)
Calmodulin	$kf_{CM}=1.64 \cdot 10^6$ (mM s) ⁻¹	Automatic optimization (Ca _i range)
Calsequestrin	$kf_{CQ}=175$ (mM s) ⁻¹	Automatic optimization (Ca _i range)
Calcium diffusion	$\tau_{diffCa}=5.47 \cdot 10^{-5}$ s	Automatic optimization (Ca _i range)
Intracellular Na	Fixed at 5 mM	As used in human SAN experiments (Verkerk <i>et al.</i> , 2007b)

C_m , membrane capacitance; L_{cell} , R_{cell} , length and radius of the cell; g_i , maximal conductance for the i type channel; P_{CaT} , P_{CaL} , permeability for the T and L-type calcium currents; $V_{\frac{1}{2},dL}$, k_{dL} , half-activation potential and slope factor for voltage dependent d_L gate; K_{NaCa} , maximal current of NCX; k_s , maximal rate of calcium release from RyR channels; k_{om} , transition rate from open (O) to resting (R) state of RyR channels; kf_{CM} , kf_{CQ} , association constant for calmodulin and calsequestrin. The reported features in brackets (APD, CL, Ca_i range, DD, OS) are those on which each parameter had a larger impact during the automatic optimization procedure.

1.2.4.1 Funny current (I_f)

From their experiments on human SAN cells, Verkerk *et al.* (2007b) reported a maximal I_f conductance of 75.2 ± 3.8 pS/pF (mean \pm SEM, $n = 3$). Consequently, we assumed a maximal I_f conductance (g_f) of 4.3 nS, given our C_m of 57 pF. The funny current was implemented by splitting it into Na^+ and K^+ components, with a $\frac{g_{fNa}}{g_{fK}}$ conductance ratio of 0.5927, thus arriving at an I_f reversal potential (E_f) of -22 mV, in accordance with the experimentally determined value of -22.1 ± 2.4 mV (mean \pm SEM, $n = 3$) (Verkerk *et al.* 2007b). A first-order Hodgkin and Huxley-type kinetic scheme was assumed for I_f activation, as described by the formulations presented by Verkerk *et al.* (2007a) and Verkerk & Wilders (2010). The activation time constant τ_y was formulated in accordance with Verkerk *et al.* (2007a), who used a Dokos *et al.* (1996)-type equation to fit the experimental data obtained from three human adult SAN cells by Verkerk *et al.* (2007b).

1.2.4.2 Rapid delayed rectifier K^+ current (I_{Kr})

The steady-state activation curve of I_{Kr} (pa gate) was fitted to data from embryonic human cardiomyocytes by Danielsson *et al.* (2013). The measured tail current density following activation pulses from -70 to $+50$ mV was normalized with respect to the maximal measured value and then fitted with a Boltzmann equation. The conductance g_{Kr} was set to 4.2 nS (+10% compared to parent model) to hyperpolarize the maximum diastolic potential (MDP) and obtain the value experimentally observed in human SAN (Drouin, 1997; Verkerk *et al.*, 2007b).

1.2.4.3 Slow delayed rectifier K^+ current (I_{Ks})

The steady-state activation curve for I_{Ks} (n gate) was updated in accordance with the experimental data of Danielsson *et al.* (2013). The reported current density vs. voltage data were normalized to the maximal measured value and subjected to square-root, in line with the second-order Hodgkin and Huxley-type kinetic scheme. Data were then fitted with a Boltzmann equation. The conductance g_{Ks} was set to 0.65 nS (11.4 pS/pF), -78% with respect to the parent model, as a result of the automatic optimization procedure. On one hand, Chandler *et al.* (2009) reported an mRNA expression level in the human SAN equal to 69% of that in non-specialized atrium cells. On the other hand, very discordant values have been reported for g_{Ks} in human atrial cells up to now, ranging from 3.5 pS/pF (Grandi *et al.*, 2011) to 20 pS/pF (Nygren *et al.*, 1998), whereas g_{Ks} was adjusted to 129 pS/pF in the model of Courtemanche *et al.* (1998) simply to match AP duration.

1.2.4.4 Ultrarapid delayed rectifier K^+ current (I_{Kur})

Chandler *et al.* (2009) reported the expression of $K_{V1.5}$ channels, responsible for I_{Kur} , in human SAN tissue. Because I_{Kur} was not present in the parent model, we added this current, formulating it as in the human atrial cell model of Maleckar *et al.* (2009). The I_{Kur} conductance was set to 0.1539 nS, 6% of the corresponding atrial value, based on the automatic optimization procedure.

1.2.4.5 Transient outward K^+ current (I_{to})

We maintained the parent model formulation, which, in turn, was adopted from the model of Maltsev & Lakatta (2009). The I_{to} conductance was set to 3.5 nS, slightly reduced (-1.5%) compared to the rabbit SAN model.

1.2.4.6 Sodium/potassium pump current (I_{NaK})

For I_{NaK} , the formulation by Severi *et al.* (2012), which was in turn derived from that of Kurata *et al.* (2002), was adopted. The maximal activity of the Na^+/K^+ pump was reduced by 28% ($I_{NaK,max} = 0.08105$ nA) through automatic optimization.

1.2.4.7 Sodium current (I_{Na})

The presence of fast Na^+ current (I_{Na}) in human SAN cells has been reported by Verkerk *et al.* (2009b). The steady-state activation and inactivation curves (gates m and h) of the parent model have been simply rewritten in a sigmoidal formulation (see Appendix 1) to facilitate the implementation of mutations related to $Na_v1.5$ channels.

1.2.4.8 T-type Ca^{2+} current (I_{CaT})

The mathematical formulation of I_{CaT} was inherited from the parent model and thus based on the constant field equation by Sarai *et al.* (2003). The Ca^{2+} permeability P_{CaT} was set to 0.04132 nA mM^{-1} (+15%), as obtained by automatic optimization.

1.2.4.9 L-type Ca^{2+} current (I_{CaL})

Changes in I_{CaL} kinetics were limited to the voltage-dependent steady-state activation curve dL . The half-maximal activation voltage ($V_{1/2,dL}$) was slightly shifted towards less negative potentials (from -20.3 to -16.45 mV) and the slope factor k_{dL} was slightly increased (from 4.2 to 4.337 mV). The Ca^{2+} permeability

was increased by 28% ($P_{CaL} = 0.4578 \text{ nA mM}^{-1}$). All of these parameters were updated using automatic optimization.

1.2.4.10 Sodium/calcium exchange current (I_{NaCa})

The set of equations describing the Na^+/Ca^{2+} exchanger activity was adopted from the parent model and thus originally derived by Kurata *et al.* (2002). The maximal current provided by the exchanger was set to 3.343 nA, reduced by 53% as a result of the automatic optimization procedure.

1.2.5 Calcium handling

As in the parent model, the mathematical formulation of Ca^{2+} handling was based on Maltsev & Lakatta (2009), who provided an advanced description of SR behaviour. The parameter updates, which play an important role in Ca^{2+} handling, were achieved by automatic optimization.

1.2.5.1 SR Ca^{2+} uptake (J_{up})

The Ca^{2+} uptake flux was formulated by a sigmoidal curve, instead of the Michaelis–Menten equation of the parent model. The sigmoidal formulation permitted a higher control of Ca^{2+} uptake, in particular during the diastolic phase.

1.2.5.2 SR Ca²⁺ release (J_{rel})

The Ca²⁺ diffusion rate k_s , and the ryanodine receptors (RyRs) Ca-dependent activation rate, k_{om} , were set to $148 \times 10^6 \text{ s}^{-1}$ and 660 s^{-1} , respectively, through automatic optimization.

1.2.5.3 Ca²⁺ diffusion and Ca²⁺ buffers

The time constant for Ca²⁺ diffusion from the subsarcolemma to the cytosol (τ_{difCa}) was set to $5.469 \times 10^{-5} \text{ s}$. The Ca²⁺ association constants for calmodulin (k_{fCM}) and calsequestrin (k_{fCQ}) were set to 1.642×10^6 and $175.4 \text{ (mM s)}^{-1}$, respectively.

Calmodulin is involved in Ca²⁺ buffering in the cytosolic compartment, whereas calsequestrin binds Ca²⁺ in the junctional SR (jSR).

1.2.6 Ion concentrations

Ca²⁺ dynamics for the four compartments were described by the mass balance equations. Intracellular Na⁺ was fixed at 5 mM, the Na⁺ concentration in the pipette solution used in the whole cell configuration by Verkerk *et al.* (2007b).

In such a configuration, intracellular Na⁺ is expected to equilibrate with the pipette solution.

1.2.7 Sensitivity analysis

The sensitivity analysis was performed according to the approach proposed by Sobie (2009). The randomization procedure involved the parameters that underwent automatic optimization and the remaining maximal conductances, for a total of 18 parameters. The conductances were randomized through scaling factors chosen from a log-normal distribution with a median value of one and an SD $\sigma = 0.1873$; thus, an increase of 20% represents 1 SD away from the control value.

Shifts of the steady-state gating variables and the sarco-endoplasmic reticulum Ca^{2+} -ATPase (SERCA) pump calcium dependence were extracted from a normal distribution centered on zero, with SDs of $\sigma = 2$ mV and $\sigma = 50$ nM, respectively. The randomization was run for a population of 500 models. All of them were simulated and the corresponding AP and CaT features were computed.

Parameters and their corresponding features were collected in the X ($n \times p$) and Y ($p \times m$) matrices, respectively, where n corresponds to the number of simulations showing an auto-oscillating behaviour (< 500), p is the number of parameters and m is the number of computed features. Next, the matrix B ($p \times m$) containing the sensitivity coefficients was computed using the formula:

$$B = (X^T \times X)^{-1} \times X^T \times Y$$

1.2.8 Calibration of the population of models

The randomization of the parameters performed during the sensitivity analysis procedure led to a population of 500 models. First, the models that didn't show automaticity were discarded; then, the population was calibrated selecting the cell models that showed MDP, CL, APD_{90} and DDR_{100} within the experimental range mean \pm SEM.

1.2.9 Hardware and software

The human SAN model was built in Simulink (The Mathworks, Inc., Natick, MA, USA). Simulations ran on an OS X Mavericks (version 10.9.5) Apple computer (Apple, Cupertino, CA, USA) equipped with an Intel i7 dual core processor (Intel, Santa Clara, CA, USA). Numerical integration was performed by ode15s, a variable order solver based on numerical differentiation formulas, provided by MatLab (The Mathworks, Inc.). Simulations were run until steady-state was reached, which occurred after 50 s, based on the observation of calcium concentrations in each compartment. The automatic optimization and feature extraction were performed by custom code in MatLab 2013a. Model code is available at: <http://www.mcbeng.it/en/downloads/software/hap-san.html> and also in the CellML Model Repository (<http://models.cellml.org/>).

1.3 Results

Human SAN model behaviour in basal conditions

1.3.1 Simulated AP and calcium transient

The simulated AP waveform reproduces the available experimental traces well (Fig. 1.2A). Indeed, most of the quantitative parameters that describe AP morphology (i.e. CL, MDP, APD₉₀ and DDR₁₀₀) are within the mean \pm SD range of the experimental ones (Verkerk *et al.*, 2007b) (Table 1.2). In particular, the AP generated by the model is characterized by a CL of 814 ms, corresponding to a beating rate of 74 beats min⁻¹. However, the model presents a higher (dV/dt)_{max} and overshoot (OS) and a longer APD₂₀ (predicted features beyond the experimental mean \pm SD range).

The simulated Ca²⁺ transient qualitatively reproduces the single experimental trace acquired by Verkerk *et al.* (2013), showing a smaller transient amplitude and longer duration compared to rabbit data. Even if the model predicts slightly lower values for both diastolic and systolic [Ca²⁺]_i, the CaT amplitude (intracellular CaT amplitude; TA) is close to the experimental data (Fig. 1.2B and Table 1.3).

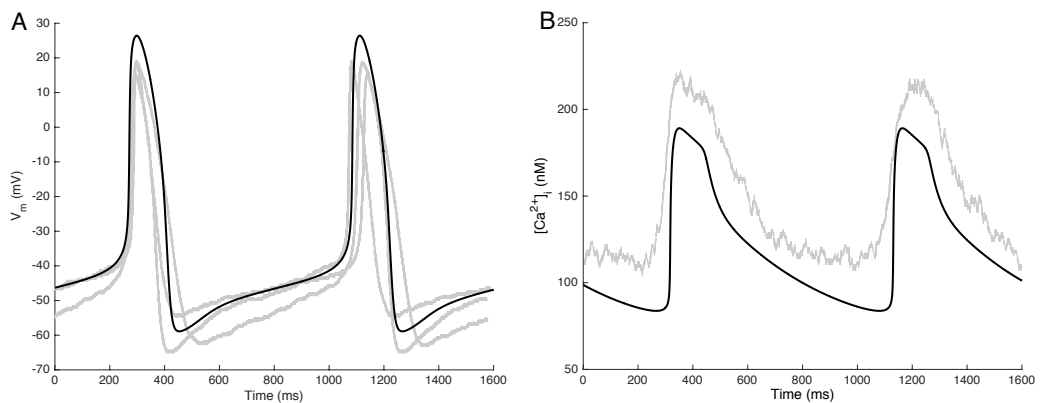


Figure 1.2 Action potential and intracellular Ca²⁺ transient of a single human SAN cell.

(A) Simulated action potential of a single human SAN cell (black thick line) and experimentally recorded action potentials of three different isolated human SAN cells (grey traces). Experimental data from Verkerk *et al.* (2009a; 2010). (B) Simulated (black thick line) and experimentally recorded (grey line) Ca²⁺ transient. Experimental data from Verkerk *et al.* (2013).

Table 1.2: Action potential features.

AP feature	Unit	Experimental Value	Present Model
MDP	mV	-61.7 ± 6.1	-58.9
CL	ms	828 ± 21	814
$(dV/dt)_{\max}$	V/s	4.6 ± 1.7	7.4
APD ₂₀	ms	64.9 ± 23.9	98.5
APD ₅₀	ms	101.5 ± 38.2	136.0
APD ₉₀	ms	143.5 ± 49.3	161.5
OS	mV	16.4 ± 0.9	26.4
DDR ₁₀₀	mV/s	48.9 ± 25.5	48.1

Comparison between experimental (mean \pm SD, n = 3) (Verkerk *et al.*, 2007b) and simulation data

Table 1.3: Calcium transient features.

Calcium Transient	Unit	Experimental Value	Present Model
Ca _i range	nM	105 - 220	85 - 190
TA	nM	115	105
TD ₂₀	ms	138.9	136.7
TD ₅₀	ms	217.4	206.3
TD ₉₀	ms	394.0	552.3

Comparison between experimental (Verkerk *et al.*, 2013) and simulation data.

The time courses of the underlying currents, Ca^{2+} fluxes and Ca^{2+} concentrations in the four intracellular compartments are shown in Fig. 1.3. The main inward (depolarizing) and outward (repolarizing) membrane currents are I_{CaL} and I_{Kr} , respectively (Fig. 3C). However, the peak amplitude of I_{tot} (Fig. 1.3B), and therefore the maximum AP upstroke velocity, is determined not only by I_{CaL} , but also by I_{NaCa} (Fig. 1.3E). Other currents are much smaller in amplitude than I_{CaL} and I_{Kr} . Yet, several are important determinants of the net ionic current during DD, and thus of CL (see below). Of note, as set out in Chapter 3, sinus node dysfunction can result from mutations in I_{f} , I_{Na} and I_{Ks} , which are among the smallest currents (Fig. 3D).

The calcium-induced calcium release from the jSR upon calcium entry through the I_{CaL} channels is reflected by the rapid increase in J_{rel} (Fig. 3G) and the accompanying rapid drop in Ca_{jSR} (Fig. 3K). The resulting increase in Ca_{sub} (Fig. 3I) and Ca_{i} (Fig. 3J) generates an increase in Ca^{2+} uptake (J_{up}) (Fig. 3H).

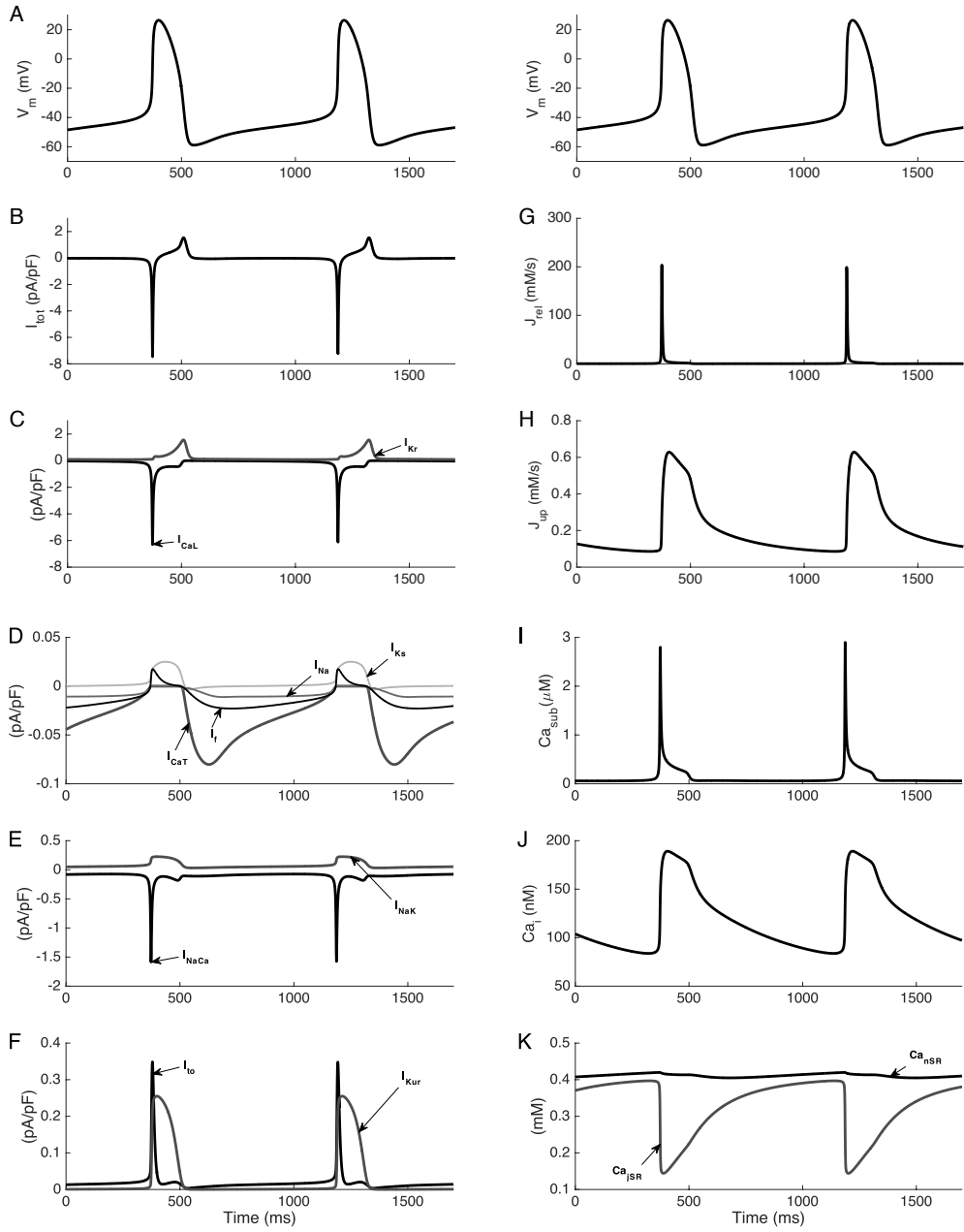


Figure 1.3: Time courses of simulated AP (A) and associated currents (B-F), fluxes (G and H) and calcium concentrations (I-K) in control steady-state conditions. Not shown is $I_{K_{ACh}}$, which is zero under control conditions. Note differences in ordinate scale.

1.3.2 Ionic currents during the DD phase

Figure 1.4 shows the time course of individual currents that play a relevant role during DD. The main inward currents during DD are I_{CaT} , I_f , I_{NaCa} and I_{CaL} .

I_{CaT} activates before the membrane potential reaches MDP and reaches its maximal current density in the first 100 ms of DD (early DD), thus contributing to DDR_{100} , and then slowly decreases. I_f is considerably smaller than I_{NaCa} but its amplitude during DD is comparable with that of the net inward current (Fig. 1.4B, dash-dotted line). Similar to I_{CaT} , I_f starts activating when the membrane is still repolarizing and it provides its maximal contribution in the first half of diastole. I_{NaCa} is a high-density inward current; it slowly diminishes during diastole, whereas it rapidly increases at the end of DD, providing an important contribution to the AP upstroke. A small amount of I_{Na} window current is active during DD. It is smaller than I_f , yet it is not negligible; it is able to modulate beating rate, as demonstrated by our simulations of mutations in the sodium voltage-gated channel α subunit 5 (SCN5A) gene (see Chapter 3). I_{CaL} follows a progressive increase during DD and becomes the major contributor to the net inward current at the end of DD; it has a relevant role during both DD and AP.

I_{NaK} , I_{Kr} and I_{Ks} are the main outward currents. I_{NaK} slowly increases during DD and reaches its maximal current density during AP, contributing to repolarization. I_{Kr} is the major driver in the repolarization process. It contributes to DD through its progressive decrease during this phase. The contribution of I_{Ks} to DD is almost negligible under control conditions, although gain-of function mutations can lead to a remarkable slowdown of pacemaking (see Chapter 3).

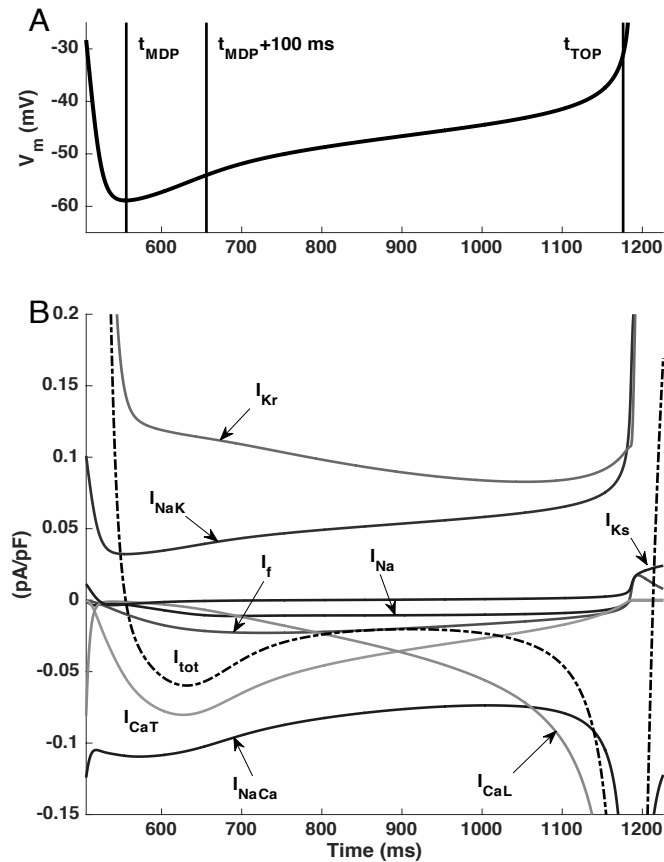


Figure 1.4: Membrane currents underlying diastolic depolarization. (A) Membrane potential and (B) associated net membrane current (I_{tot} , dash-dotted trace) during diastolic depolarization and contributing inward and outward currents. t_{MDP} and t_{TOP} indicate the time at which V_m reaches MDP and take-off potential, respectively.

1.3.3 Sensitivity analysis

Among the randomly generated population of 500 models, more than 300 showed an auto-oscillating behaviour. The results of the sensitivity analysis are reported in Fig. 1.5A, which shows the coefficients of the sensitivity matrix B , coded in a colour map. Each value in the matrix shows how a change in the parameter P displayed at the top is capable of affecting the feature F displayed on the left, and the coefficients <-0.2 and >0.2 are reported in the corresponding pixel. The obtained map highlights that nine out of the starting 18 parameters

show coefficients lower or higher than the selected thresholds of -0.2 and 0.2 , respectively.

As illustrated in Fig. 1.5A, changes in the permeability of I_{CaL} (P_{CaL}) and its activation kinetics (slope factor k_{dL} and shift in half-activation voltage $shift_{dL}$) have a large impact on upstroke velocity (dV/dt), AP duration ($APD_{20,50,90}$) and calcium transient. Furthermore, the kinetics of the I_{CaL} activation gate dL strongly affects CL and DDR_{100} . Similarly, a change of the maximal conductance of I_{Kr} (g_{Kr}) has a high impact on APA, MDP and APD, whereas the maximal activity of NCX (K_{NaCa}) strongly influences APA, dV/dt and calcium transient. Finally, a shift in the working point of the SERCA pump ($shift_{up}$) clearly affects the diastolic calcium concentration ($Ca_{i,min}$). Figure 1.5B shows that CL is largely determined by the I_{CaL} activation kinetics (through its parameters k_{dL} and $shift_{dL}$). Figure 1.5C shows that DDR_{100} is also largely determined by the activation kinetics of I_{CaL} but in the opposite way. In addition, it reveals that the permeability of I_{CaT} (P_{CaT}) is also an important determinant of DDR_{100} .

The parameter randomization, the first step of the linear regression approach, allowed us to explore a neighbourhood, in the parameter space, of the parameter set obtained as a result of the automatic optimization procedure. Only a few parameter sets (out of 500 tested) led to comparable values of the cost function. In particular, only four led to values of MDP, CL, APD_{90} and DDR_{100} within the target range (i.e. $mean \pm SEM$ of experimental values) and only one parameter set led to a slightly lower value of the cost function than the one obtained from the ‘optimized’ set of parameters. To compare these two models, the effects on the pacemaking rate of mutations affecting I_f and I_{Na} (more details are provided in Chapter 3) were compared for the two parameter sets. The ‘alternative’ set of parameters produced effects in close agreement with the ‘optimized’ set: the difference in mutation-induced changes in the pacemaking rate was always lower than 2.7%

The presence of multiple parameter sets compatible with experimental ranges allowed us to compute estimation intervals for the parameters that underwent the optimization procedure (Sarkar & Sobie, 2010). Nominal values and ranges for the optimized parameters are reported in Table A1 in Appendix 2. To confirm that

parameter values outside the estimated confidence interval lead to non-physiological (or at least non-basal) conditions, we tested the effect of changing P_{CaT} by 50% more or 50% less with respect to the parent rabbit model (instead of +15% as in the 'optimized' model). In accordance with the above observation that P_{CaT} is an important determinant of DDR_{100} , a large increase in P_{CaT} led to a notably higher beating rate (+17%; from 74 to 86 beats min^{-1}), whereas a large decrease in permeability resulted in a slower beating rate (-18.9%; from 74 to 60 beats min^{-1}). These results indicate that I_{CaT} could play a substantial role in pacemaking and underscore that the proposed value for P_{CaT} is quite well constrained (see also Table A1 in Appendix 2).

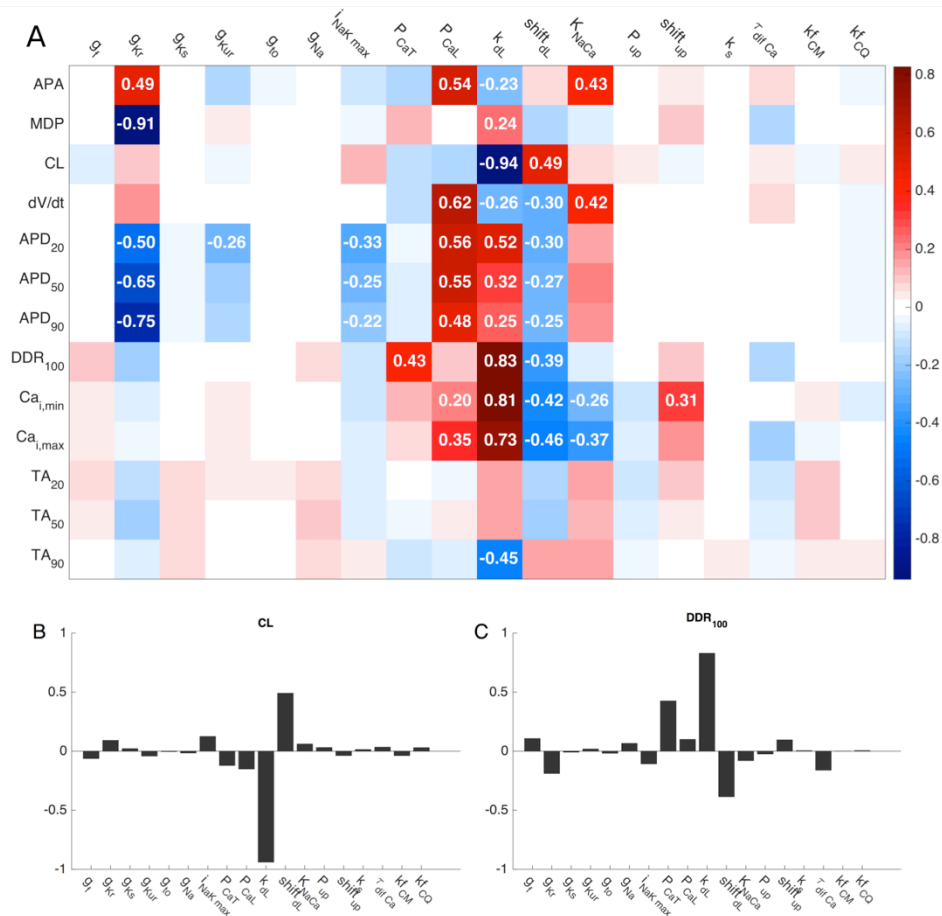


Figure 1.5 : Sensitivity Analysis

(A) Color coded map of sensitivity matrix **B**. Columns show how a specific parameter p affects AP and CaT features; rows show how each feature is affected by different parameters. Red, blue and white pixels represent positive, negative and no substantial correlation between parameters and features, respectively. Coefficients <-0.2 or >0.2 are considered substantial.

(B) and (C) Bar graphs describe how changes in each of the parameters affect CL and DDR_{100} . The two panels display in a different way the information reported in rows 3 and 8 of panel A.

1.3.4 Calibration of the population of models

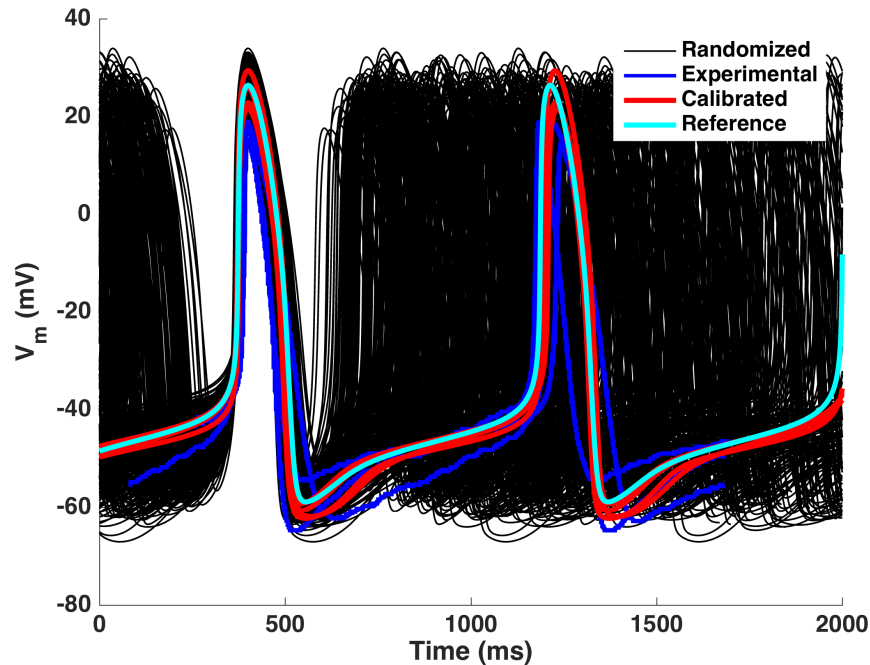


Figure 1.6: Calibration of the population of models

Comparison between auto-oscillating (black traces), calibrated (red traces), reference model (ciano trace) and experimental data (blue traces). Among the 500 randomly generated cell models, 318 maintained the automaticity. Four cell models showed MDP, CL, APD_{90} and DDR_{100} falling within the $mean \pm SEM$ experimental range and then were compared with the reference model.

Figure 1.6 reports the auto-oscillating (black traces) the calibrated (red traces), the reference models (ciano trace), and compare them with experimental data (blue traces). The randomly generated population showed 318 out of 500 self-oscillating models. The calibration performed using MDP, CL, APD_{90} and DDR_{100} , as features to be satisfied, reduced the number of models to only 4. The calibrated models showed a MDP = -62.2, -61.8, -60.8 and -59.3 mV, respectively; slightly hyperpolarized with respect to the reference model. The CL was slightly higher (CL = 819, 827, 828 and 834 ms vs 814 ms) in all the four cases. APD_{90} was 146, 162, 145 and 149 ms, respectively; two models showed

DDR₁₀₀ lower (DDR₁₀₀ = 39.5, 37.0 mV/s) and two higher (DDR₁₀₀ = 52.3, 56.1 mV/s) than the reference model (DDR₁₀₀ = 48.1 mV/s).

The diastolic (Ca_{i,min}) and systolic (Ca_{i,max}) Ca²⁺ values were close to the reference model in two cases out of four (Ca_{i,min} = 95 and 88 nM vs 84 nM and Ca_{i,max} = 192 and 194 nM vs 189 nM). The other models showed lower levels both for diastolic (Ca_{i,min} = 65 and 57 nM) and systolic Ca²⁺ (Ca_{i,max} = 153 and 137 nM).

1.4 Discussion

In the present study, we formulated a comprehensive human SAN AP model, starting from a state-of-the-art model of rabbit cardiac pacemaker cells, and converting it into a species-specific description using human experimental data as far as possible. A novel aspect is the adoption of an automatic optimization procedure, tightly bounded by the AP features, to identify the parameters for which experimental data are presently unavailable.

Previously, Chandler *et al.* (2009) showed that scaling ion current densities, according to the gene expression pattern they found in human SAN vs. atrial tissue, gives rise to automaticity in the human atrial cell model of Courtemanche *et al.* (1998). However, the values of the descriptive parameters of AP, in particular MDP, APA and APD, were far from the experimentally observed ones. As will be further detailed in Chapter 2 and 3, our model is able to reproduce the main experimentally observed electrophysiological features (AP waveform, calcium transient) and the simulated changes in pacemaking rate as a result of mutations affecting ionic channels are in line with clinical data. Furthermore, it allows the investigation of relevant conditions such as I_f block, NCX block and autonomic stimulation.

1.4.1 Construction of the model

AP models of cardiac cells are commonly based on voltage clamp data for ionic current identification and current clamp data for model validation. We tried to maximally exploit the scarce data available on human SAN cells, aiming at a detailed reproduction of experimental AP morphology. Updating the description of the funny current, based on the experimental data obtained by Verkerk *et al.* (2007b), was also crucial. In our human cell model, I_f current density during DD is considerably lower than in rabbit SAN cells, although it remains comparable to the net inward current as reported by Verkerk & Wilders (2010) in their virtual AP clamp experiments.

In control conditions, the model reproduces the experimental AP features well. The simulated AP is characterized by $CL = 814$ ms, which is close to the experimentally observed values (Verkerk *et al.*, 2007b) and critical parameters such as MDP, APD_{90} and DDR_{100} are all within the range of the experimental data (Table 1.2). As a consequence, the model shows a representative behaviour during both DD (subthreshold) and AP (Fig. 1.3).

A preliminary study on Ca^{2+} handling behavior was performed through a guess and check approach that highlighted the candidate parameters for the automated optimization. Among the twelve automatically optimized parameters, ten of them were involved in the calcium handling, regulating the Ca^{2+} fluxes through the membrane (P_{CaT} , P_{CaL} , V_{dL} , k_{dL} , K_{NaCa}) and in the cytosol, through the activity of SR (k_s and k_{up}), Ca^{2+} buffers (k_{fCM} , k_{fCQ}) and diffusion (τ_{diffCa}).

To achieve a calcium transient close to the experimental trace, several actors of Ca^{2+} handling underwent changes; in particular, maximal NCX activity was reduced by 53%, and a sigmoidal equation was introduced to describe SR uptake. These updates allowed a higher diastolic $[Ca^{2+}]_i$ and finer control during DD.

The availability of a unique Ca^{2+} trace acquired from a single human SAN cell (Verkerk *et al.* 2013) represents the main limitation for a proper description of Ca^{2+} dynamics. This had repercussions on the optimization procedure, where an arbitrary value for the experimental range (experimental value $\pm 10\%$) was set.

Moreover, to achieve a more accurate description of Ca^{2+} dynamics, it would be helpful to characterize also the spatial distribution of Ca^{2+} in the compartments. This approach, however, would lead to a higher level of complexity, that is not required for the overall aim of this work.

The Cs^+ -induced CL prolongation that was experimentally observed was also taken into account to tune parameters. Simulating the administration of 2 mM Cs^+ led to an increase in CL of 28.1%, close to the experimentally observed 26%, as detailed in Chapter 2. This Cs^+ concentration was reported to selectively and almost fully block the funny current (Verkerk *et al.*, 2007b) and so the reported prolongation established the maximal extent of the contribution of I_f to the pacemaking rate decrease in our model. Thus, the experimentally observed levels of I_f block by Cs^+ were highly relevant. Accordingly, we should not forget that a voltage-dependent partial block of funny channels by 5 mM Cs^+ has been reported elsewhere (DiFrancesco *et al.*, 1986). If the parameters in our model were tuned to reproduce a similar partial Cs^+ -induced block, a larger effect of complete I_f block would be observed in simulations.

1.4.2 Sensitivity analysis and calibration of the population of models

The sensitivity analysis highlighted the strong impact of I_{CaL} , in particular its activation kinetics (gate dL), on CL and on the calcium transient. A slight increase/decrease of the slope factor k_{dL} and a shift of the working point of the steady-state curve of the activation gate are able to substantially change these two features; indeed, the availability of open I_{CaL} channels during the highly sensitive DD phase is strongly affected by slight changes of the dL kinetics.

The calibration procedure showed that 4 models out 500 satisfied the experimental range for MDP, CL, APD_{90} and DDR_{100} . The criterion with the population of model was calibrated was analogous with the one adopted by Britton *et al.* (2013) for a population of models of rabbit Purkinje fibers. In this work the investigated population was wider (10000 models) and the final

calibration provided 213 model consistent with experimental data ($\approx 2\%$); the calibrated human SAN population showed a similar number of models consistent with the experimental range (0.8)%.

The simulations performed for the sensitivity analysis highlighted that the same AP can be produced by multiple sets of parameters. However, the observation that only a few parameter sets, out of a total of 500, produced simulation data within the experimental range, as showed by the calibration of the population of models, suggests that the parameters should fall within a narrow range. Among the calibrated models, indeed, the parameters that showed highest variations with respect to the reference model were g_{Kur} ($\approx -36\%$) and K_{NaCa} ($\approx +48\%$); for more details see Table A1 in Appendix 2.

Ranges in Table A1 in Appendix 2 are a first attempt to determine such physiological intervals for human SAN cells exploiting the limited experimental data. Future measurements will help to refine the information extracted by our investigation.

The illustrative investigation of the effects of changes in P_{CaT} suggests that this parameter is well constrained, and also that I_{CaT} plays a role in pacemaking, which is consistent with the report by Mangoni *et al.* (2006) who studied mice with a disrupted gene coding for $Ca_v3.1$ channels, as responsible for T-type calcium current.

1.5 Limitations and future developments

One evident limitation of the present study is that there are insufficient experimental data available on human SAN electrophysiology to fully constrain the parameters of the model. It is therefore possible that some non-human-specific aspects of the parent (rabbit) model are still present. The here discussed model thus only represents one step forward in the quantitative description of human SAN electrophysiology. Further experiments carried out on human adult SAN cells, or perhaps even on human induced pluripotent stem cell-derived cardiomyocytes, will challenge the current model, providing confirmation and/or

clarifying any changes that need to be made.

Specific limitations of the model include: the lack of intracellular sodium dynamics, and the lack of a detailed description of local calcium releases.

References

- Britton OJ, Bueno-Orovio A, Ammel KV, Lu HR, Towart R, Gallacher DJ & Rodriguez B (2013). Experimentally calibrated population of models predicts and explains intersubject variability in cardiac cellular electrophysiology. *Proc Natl Acad Sci* 110, E2098–E2105.
- Chandler NJ, Greener ID, Tellez JO, Inada S, Musa H, Molenaar P, DiFrancesco D, Baruscotti M, Longhi R, Anderson RH, Billeter R, Sharma V, Sigg DC, Boyett MR & Dobrzynski H (2009). Molecular architecture of the human sinus node insights into the function of the cardiac pacemaker. *Circulation* 119, 1562–1575.
- Courtemanche M, Ramirez RJ & Nattel S (1998). Ionic mechanisms underlying human atrial action potential properties: insights from a mathematical model. *Am J Physiol - Heart Circ Physiol* 275, H301–H321.
- Danielsson C, Brask J, Sköld A-C, Genead R, Andersson A, Andersson U, Stockling K, Pehrson R, Grinnemo K-H, Salari S, Hellmold H, Danielsson B, Sylvén C & Elinder F (2013). Exploration of human, rat, and rabbit embryonic cardiomyocytes suggests K-channel block as a common teratogenic mechanism. *Cardiovasc Res* 97, 23–32.
- DiFrancesco D (2010). The role of the funny current in pacemaker activity. *Circ Res* 106, 434–446.
- DiFrancesco D, Ferroni A, Mazzanti M & Tromba C (1986). Properties of the hyperpolarizing-activated current (if) in cells isolated from the rabbit sinoatrial node. *J Physiol* 377, 61–88.
- DiFrancesco D & Noble D (1985). A model of cardiac electrical activity incorporating ionic pumps and concentration changes. *Philos Trans R Soc Lond B Biol Sci* 307, 353–398.
- DiFrancesco D & Noble D (2012). The funny current has a major pacemaking role in the sinus node. *Heart Rhythm* 9, 299–301.
- Dokos S, Celler B & Lovell N (1996). Ion currents underlying sinoatrial node pacemaker activity: a new single cell mathematical model. *J Theor Biol* 181, 245–272.

- Drouin E (1997). Electrophysiologic properties of the adult human sinus node. *J Cardiovasc Electrophysiol* 8, 254–258.
- Grandi E, Pandit SV, Voigt N, Workman AJ, Dobrev D, Jalife J & Bers DM (2011). Human atrial action potential and Ca²⁺ model sinus rhythm and chronic atrial fibrillation. *Circ Res* 109, 1055–1066.
- Himeno Y, Sarai N, Matsuoka S & Noma A (2008). Ionic mechanisms underlying the positive chronotropy induced by β 1-adrenergic stimulation in guinea pig sinoatrial node cells: a simulation study. *J Physiol Sci* 58, 53–65.
- Himeno Y, Toyoda F, Satoh H, Amano A, Cha CY, Matsuura H & Noma A (2011). Minor contribution of cytosolic Ca²⁺ transients to the pacemaker rhythm in guinea pig sinoatrial node cells. *Am J Physiol - Heart Circ Physiol* 300, H251–H261.
- Kharche S, Yu J, Lei M & Zhang H (2011). A mathematical model of action potentials of mouse sinoatrial node cells with molecular bases. *Am J Physiol - Heart Circ Physiol* 301, H945–H963.
- Kurata Y, Hisatome I, Imanishi S & Shibamoto T (2002). Dynamical description of sinoatrial node pacemaking: improved mathematical model for primary pacemaker cell. *Am J Physiol - Heart Circ Physiol* 283, H2074–H2101.
- Lagarias JC, Reeds JA, Wright MH & Wright PE (1998). Convergence properties of the Nelder-Mead simplex method in low dimensions. *SIAM J Optim* 9, 112–147.
- Lakatta EG (2010). A paradigm shift for the heart's pacemaker. *Heart Rhythm* 7, 559–564.
- Lakatta EG & DiFrancesco D (2009). What keeps us ticking: a funny current, a calcium clock, or both? *J Mol Cell Cardiol* 47, 157–170.
- Lakatta EG & Maltsev VA (2012). Rebuttal: What If the shoe doesn't fit? "The funny current has a major pacemaking role in the sinus node." *Heart Rhythm* 9, 459–460.
- Lakatta EG, Maltsev VA & Vinogradova TM (2010). A coupled SYSTEM of intracellular Ca²⁺ clocks and surface membrane voltage clocks controls the timekeeping mechanism of the heart's pacemaker. *Circ Res* 106, 659–673.
- Maleckar MM, Greenstein JL, Giles WR & Trayanova NA (2009). K⁺ current changes account for the rate dependence of the action potential in the human atrial myocyte. *Am J Physiol - Heart Circ Physiol* 297, H1398–H1410.

- Maltsev VA & Lakatta EG (2009). Synergism of coupled subsarcolemmal Ca²⁺ clocks and sarcolemmal voltage clocks confers robust and flexible pacemaker function in a novel pacemaker cell model. *Am J Physiol - Heart Circ Physiol* 296, H594–H615.
- Maltsev VA & Lakatta EG (2010). A novel quantitative explanation for the autonomic modulation of cardiac pacemaker cell automaticity via a dynamic system of sarcolemmal and intracellular proteins. *Am J Physiol - Heart Circ Physiol* 298, H2010–H2023.
- Mangoni ME, Traboulsie A, Leoni A-L, Couette B, Marger L, Quang KL, Kupfer E, Cohen-Solal A, Vilar J, Shin H-S, Escande D, Charpentier F, Nargeot J & Lory P (2006). Bradycardia and Slowing of the Atrioventricular Conduction in Mice Lacking Ca_v3.1/ α 1G T-Type Calcium Channels. *Circ Res* 98, 1422–1430.
- McAllister RE, Noble D & Tsien RW (1975). Reconstruction of the electrical activity of cardiac Purkinje fibres. *J Physiol* 251, 1–59.
- Monfredi O, Maltsev VA & Lakatta EG (2013). Modern concepts concerning the origin of the heartbeat. *Physiology* 28, 74–92.
- Noble D, Noble PJ & Fink M (2010). Competing oscillators in cardiac pacemaking historical background. *Circ Res* 106, 1791–1797.
- Noble D & Noble SJ (1984). A model of sino-atrial node electrical activity based on a modification of the DiFrancesco-Noble (1984) equations. *Proc R Soc Lond B Biol Sci* 222, 295–304.
- Nygren A, Fiset C, Firek L, Clark JW, Lindblad DS, Clark RB & Giles WR (1998). Mathematical model of an adult human atrial cell the role of K⁺ currents in repolarization. *Circ Res* 82, 63–81.
- Pohl A, Wachter A, Hatam N & Leonhardt S (2016). A computational model of a human single sinoatrial node cell. *Biomed Phys Eng Express* 2, 035006.
- Rosen MR, Nargeot J & Salama G (2012). The case for the funny current and the calcium clock. *Heart Rhythm* 9, 616–618.
- Sarai N, Matsuoka S, Kuratomi S, Ono K & Noma A (2003). Role of individual ionic current systems in the SA node hypothesized by a model study. *Jpn J Physiol* 53, 125–134.
- Sarkar AX & Sobie EA (2010). Regression Analysis for Constraining Free Parameters in Electrophysiological Models of Cardiac Cells. *PLOS Comput Biol* 6, e1000914.

- Seemann G, Höper C, Sachse FB, Dössel O, Holden AV & Zhang H (2006). Heterogeneous three-dimensional anatomical and electrophysiological model of human atria. *Philos Transact A Math Phys Eng Sci* 364, 1465–1481.
- Severi S, Fantini M, Charawi LA & DiFrancesco D (2012). An updated computational model of rabbit sinoatrial action potential to investigate the mechanisms of heart rate modulation. *J Physiol* 590, 4483–4499.
- Sobie EA (2009). Parameter Sensitivity Analysis in Electrophysiological Models Using Multivariable Regression. *Biophys J* 96, 1264–1274.
- Verkerk AO, Borren MMGJ van, Peters RJG, Broekhuis E, Lam KY, Coronel R, Bakker JMT de, Tan HL & Wilders R (2007a). Single cells isolated from human sinoatrial node: action potentials and numerical reconstruction of pacemaker current. In *29th Annual International Conference of the IEEE Engineering in Medicine and Biology Society, 2007. EMBS 2007*, pp. 904–907.
- Verkerk AO, van Borren MMGJ & Wilders R (2013). Calcium transient and sodium-calcium exchange current in human versus rabbit sinoatrial node pacemaker cells. *Sci World J* 2013, e507872.
- Verkerk AO & Wilders R (2010). Relative importance of funny current in human versus rabbit sinoatrial node. *J Mol Cell Cardiol* 48, 799–801.
- Verkerk AO & Wilders R (2015). Pacemaker activity of the human sinoatrial node: an update on the effects of mutations in HCN4 on the hyperpolarization-activated current. *Int J Mol Sci* 16, 3071–3094.
- Verkerk AO, Wilders R, Borren MMGJ van, Peters RJG, Broekhuis E, Lam K, Coronel R, Bakker JMT de & Tan HL (2007b). Pacemaker current (I_f) in the human sinoatrial node. *Eur Heart J* 28, 2472–2478.
- Verkerk AO, Wilders R, van Borren MMGJ & Tan HL (2009). Is sodium current present in human sinoatrial node cells? *Int J Biol Sci* 5, 201–204.
- Wilders R (2007). Computer modelling of the sinoatrial node. *Med Biol Eng Comput* 45, 189–207.
- Yanagihara K, Noma A & Irisawa H (1980). Reconstruction of sino-atrial node pacemaker potential based on the voltage clamp experiments. *Jpn J Physiol* 30, 841–857.
- Yaniv Y, Lakatta EG & Maltsev VA (2015). From two competing oscillators to one coupled-clock pacemaker cell system. *Card Electrophysiol* 6, 28.

Yaniv Y, Sirenko S, Ziman BD, Spurgeon HA, Maltsev VA & Lakatta EG (2013). New evidence for coupled clock regulation of the normal automaticity of sinoatrial nodal pacemaker cells: Bradycardic effects of ivabradine are linked to suppression of intracellular Ca²⁺ cycling. *J Mol Cell Cardiol* 62, 80–89.

Zhang H, Holden AV, Kodama I, Honjo H, Lei M, Varghese T & Boyett MR (2000). Mathematical models of action potentials in the periphery and center of the rabbit sinoatrial node. *Am J Physiol - Heart Circ Physiol* 279, H397–H421.

Chapter 2

Model based analysis: effects of I_f , Ca^{2+} handling and autonomic system modulation of pacemaking

The content of this chapter is published in:

“Computational analysis of the human sinus node action potential: model development and effects of mutations”

Alan Fabbri¹, Matteo Fantini¹, Ronald Wilders² and Stefano Severi¹

¹ Computational Physiopatology Unit, Department of Electrical, Electronic and Information Engineering “Guglielmo Marconi”, University of Bologna, Cesena, Italy

² Department of Anatomy, Embriology and Physiology, Academic Medical Center, University of Amsterdam, Amsterdam, The Netherlands

The Journal of Physiology, J Physiol 2017, 595 (7) 2365-239

Abstract

The heart rate (HR) is one of the most important indexes in clinical practice and its modulation has remarkable implications for treatments of heart disease. Beating rate, i.e. the inverse of cycle length (CL), is the cellular equivalent of HR. The modulation of CL occurs during the spontaneous diastolic depolarization (DD), sensitive to changes of currents. The autonomic system modulates the DD duration by affecting the kinetics of ion channels and the activity of the sarcoplasmic reticulum (SR).

Aims of this chapter are to investigate (i) how “funny current” (I_f) and the Na^+ - Ca^{2+} exchanger current (I_{NaCa}) affect the AP features and calcium transient and (ii) how the autonomic system modulates CL through the administration of acetylcholine (ACh) and isoprenaline (Iso).

A progressive block of I_f , a reduction of the maximal conductance g_f and a shift of the steady state activation curve were simulated; a progressive block of I_{NaCa} was also introduced. To simulate the effect of 10 nM of ACh changes regarding I_f , I_{CaL} , and SR Ca^{2+} pump were implemented and the ACh activated K^+ current ($I_{\text{K,ACh}}$) was included. The administration of 1 μM Iso was mimicked through changes affecting I_f , I_{NaK} , I_{CaL} and I_{Ks} and the SR Ca^{2+} pump.

The full block of I_f increased CL to 1043 ms (+28.1%) and decreased $\text{DDR}_{100} = 29 \text{ mV s}^{-1}$ (-39.7%). A -15 mV shift in the I_f steady state activation curve increased CL to 957 ms (+17.6%) with a less steep DDR_{100} (37.7 mV s^{-1} ; -21.6%), whereas a +15 mV shift shortened CL to 577 ms, showing a steeper DDR_{100} (75.4 mV s^{-1} ; +56.8%). In each simulation MDP and APD_{90} were virtually unchanged. I_{NaCa} block, at moderate levels (50 and 70%), was responsible for a faster rate (83 and 93 beats min^{-1} vs. 74 beats min^{-1} under control). DDR_{100} , APD_{90} and MDP were notably affected. Automaticity ceased upon higher levels of I_{NaCa} block.

The simulation of administration of 10 nM ACh showed a rate decrease of 21.6%, with major contributions of I_f and $I_{\text{K,ACh}}$, whereas 1 μM Iso speeded up the rate by +27.0% through I_f and I_{CaL} .

Simulations showed that I_f modulates the rate acting on DDR_{100} . I_{NaCa} block acts on CL affecting DDR_{100} , APD_{90} and MDP. The mimicking of autonomic stimulation highlighted that I_f plays an important role in HR modulation together with $I_{K,ACh}$ (for ACh) and I_{CaL} (for Iso).

2.1 Introduction

The identification of the mechanism responsible for the initiation of the spontaneous activity and the modulation of the heart rate is one of the main topics in the cardiac research field.

The foundational work by Hodgkin and Huxley (Hodgkin & Huxley, 1952) mathematically described the squid neuronal action potential (AP) as result of a coordinate activation and inactivation of voltage- and time-dependent gating variables, that are either open (fraction O between 0 and 1) or closed (fraction $C=1-O$) and thus determine the probability to find the membrane ion channels in an open or closed state. This work underlies today's mathematical models of the more complex mammalian cardiac cells, including the model of a human SA nodal pacemaker cell presented in Chapter 1.

One of the main characteristics of SAN cells is their spontaneous activity determined by the spontaneous depolarization of the membrane potential during the diastolic depolarization phase.

The first mechanism proposed to explain the spontaneous depolarization during diastole was the “ I_K decay theory”, which pointed out the decrease of the K^+ outward current as the major responsible of DD phase.

Nowadays, there are two principal and still debated theories (Lakatta & DiFrancesco, 2009) that are based on two deeply different mechanisms, known as the ‘membrane clock’ and the ‘calcium clock’: the ‘membrane clock’ assumes that the spontaneous depolarization is controlled by surface membrane ion channels, whereas the ‘calcium clock’ is based on the hypothesis that intracellular calcium cycling is responsible for the initiation of DD.

In 1979, DiFrancesco *et al.* first described the “funny current” (I_f) and, due to its electrophysiological properties, they defined I_f as “pacemaker current”. Indeed I_f is activated at hyperpolarized potentials –its activation starts at about -40/50 mV in rabbit SAN cells and it is fully activated at -100 mV– it is an inward current in the membrane potential range corresponding to the DD phase, and has a reversal

potential close to -20 mV due to its permeability to both Na^+ and K^+ (DiFrancesco, 1985; Barbuti & DiFrancesco, 2008).

Other experimental evidence supports the role of I_f as major actor in pacemaking: gene expression studies in mammals indicated that there is a correlation between pacemaking tissue and the localization of the *HCN4* gene that encodes the I_f channel HCN4 subunit (Tellez *et al.*, 2006; Liu *et al.*, 2007); the loss of spontaneous activity during fetal development is concurrent to the loss of I_f channels (Robinson *et al.*, 1997; Yasui *et al.*, 2001) and in pathological conditions the up-regulation of HCN2 in ventricular cells leads to spontaneous ectopic beats (Cerbai *et al.*, 1994, 2001).

It was also reported that the funny current is an important target for autonomic stimulation, able to modulate the heart rate: on one hand, the presence of adrenaline caused a substantial increase of I_f (DiFrancesco *et al.*, 1986) and a consequent acceleration of the DD phase; on the other hand, acetylcholine (ACh) is responsible for an inhibition of I_f (DiFrancesco & Tromba, 1987, 1988a, 1988b), shifting its steady state activation curve towards more negative potentials. A decreased I_f , together with the activation of $I_{K,ACh}$, leads to a slower depolarization and hence to a lower beating rate.

Other studies highlighted that the administration of ryanodine leads to the depletion of the sarcoplasmic reticulum (SR), with a consequent impairment of the Ca^{2+} release. The effect is a reduced Ca^{2+} transient and the impairment of the inward current provided by the $\text{Na}^+/\text{Ca}^{2+}$ exchanger, responsible for a slow spontaneous beating rate. From these observations it was proposed that intracellular calcium cycling plays an important role in pacemaker cells automaticity (Rigg & Terrar, 1996).

The ‘calcium clock’ theory is based on the presence of spontaneous local calcium releases (LCRs) from the SR (Hüser *et al.*, 2000). The presence of wavelets of Ca^{2+} activates the electrogenic membrane surface protein $\text{Na}^+/\text{Ca}^{2+}$ exchanger (NCX) responsible for I_{NaCa} (Bogdanov *et al.*, 2006). The activity of I_{NaCa} depolarizes the membrane potential during diastole and then activates I_{CaL} , responsible for the AP upstroke.

In order to control the heart rate, the intracellular calcium oscillator should be able to work at different stable rates. The ‘calcium clock’ theory hypothesizes that the modulation of the DD occurs through the presence of ‘intracellular machinery’ (e.g. adenylyl cyclase (AC) (Mattick *et al.*, 2007; Younes *et al.*, 2008), protein kinase A (PKA) (Vinogradova *et al.*, 2006), calmodulin kinase II (CaMKII) (Vinogradova *et al.*, 2000)) that controls the availability of intracellular calcium, the SR Ca^{2+} pump and the activity of ryanodine receptors (RyRs). The effects of a more intense activity of LCRs (higher amplitude and shorter LCR period) are coupled to the membrane potential through NCX. During the autonomic stimulation the heart rate is modulated through the interplay between SR, NCX and the intracellular machinery leading to a faster (β -adrenergic stimulation) (Vinogradova *et al.*, 2002, 2008) or slower (cholinergic stimulation) DD (Lyashkov *et al.*, 2009).

The two theories provide different perspectives on how the spontaneous activity is generated and how the DD is modulated. The debate on which is the ‘leading clock’ is still open and, probably, an integration of the two mechanisms could show a more robust system able to generate and regulate HR.

The work reported in this chapter aims to describe how (1) I_f , (2) I_{NaCa} and (3) the autonomic stimulation affect the AP and calcium transient and to investigate the mechanisms underlying the different ways that modulate the beating rate. To do that, the AP changes due to the loss or gain of function of I_f , a progressive block of I_{NaCa} , and the administration of 10 nM of ACh and 1 μM of isoprenaline (Iso) are quantified and discussed. Also, the behavior of the isolated Ca^{2+} oscillator is assessed.

2.2 Methods

2.2.1 Blockade of funny current (I_f) and $\text{Na}^+/\text{Ca}^{2+}$ exchanger current (I_{NaCa})

To quantitatively assess the sensitivity of CL, and thus of pacing rate, to the funny current, we carried out two simulation experiments: (i) a progressive block of funny current (30, 70, 90 and 100%, i.e. full block), by reducing the maximal conductance g_f , and (ii) a shift in voltage dependence of the steady-state activation curve y_∞ , with a range from -15 to $+15$ mV, with voltage intervals of 5 mV.

The effects of I_{NaCa} block on AP and calcium transient features were assessed through the progressive reduction of the maximal activity of the $\text{Na}^+/\text{Ca}^{2+}$ exchanger (K_{NaCa}) by 50, 70 and 90%. A full block was excluded from the analysis since the intracellular calcium concentration $[\text{Ca}^{2+}]_i$ did not achieve a steady state.

2.2.2 Autonomic modulation

The effects of 10 nM ACh on I_f activation (≈ -5 mV shift in voltage dependence of activation), I_{CaL} (3.1% reduction of maximal conductance) and SR Ca^{2+} uptake (7% decrease of maximum activity) were all adopted from the parent model (Severi *et al.*, 2012). The administration of ACh also activates $I_{\text{K,ACh}}$, which is zero in the default model. The $I_{\text{K,ACh}}$ formulation was derived from the parent model. The maximal conductance $g_{\text{K,ACh}}$ was set to 3.45 nS (reduced by 77.5%) to achieve an overall reduction of the spontaneous rate by 20.8% upon administration of 10 nM ACh, as observed by Bucchi *et al.* (2007) in rabbit SAN cells.

The targets of isoprenaline (Iso) are I_f , I_{CaL} , I_{NaK} , maximal Ca^{2+} uptake and I_{Ks} . Changes in currents were adopted from the parent model, except for the modulation of I_{CaL} , where the effect of Iso induced a slightly smaller decrease of the slope factor k_{dL} (-27% with respect to control conditions, instead of the -31%

assumed by the parent model). The I_{CaL} current was modulated to fit the experimental data reported by Bucchi *et al.* (2007) on rabbit SAN cells ($26.3 \pm 5.4\%$; mean \pm SEM, $n = 7$) for the same Iso concentration.

2.3 Results

2.3.1 Contribution of I_f to pacemaking

Four levels of I_f block were assessed: 30%, 70%, 90% and 100% (i.e. full block) (Fig. 2.1A). The total block of funny current led to an increase in CL of 28.1% to 1043 ms, and thus a decrease in pacemaking rate of 21.6% to 58 beats min^{-1} , in good accordance with the 26% increase in CL that was experimentally observed by Verkerk *et al.* (2007b), who administered 2 mM Cs^+ as a blocker of I_f to a single isolated SAN cell (Fig. 2.1B). At this concentration, Cs^+ almost completely blocks I_f in the pacemaker range of potentials, whereas the delayed rectifier K^+ current, which is also sensitive to Cs^+ , is only affected slightly (Denyer & Brown, 1990; Zaza *et al.*, 1997; Liu *et al.*, 1998).

The increase in CL was mainly the result of a lower DDR and longer DD phase (with DDR_{100} decreasing by 39.7% to 29 mV s^{-1} upon full block), whereas APD_{90} and MDP remained almost unchanged (Fig. 2.1A). Of note, the increase in CL was also largely the result of a lower DDR and longer DD phase in the experiment of Verkerk *et al.* (2007b) (Fig. 2.1B).

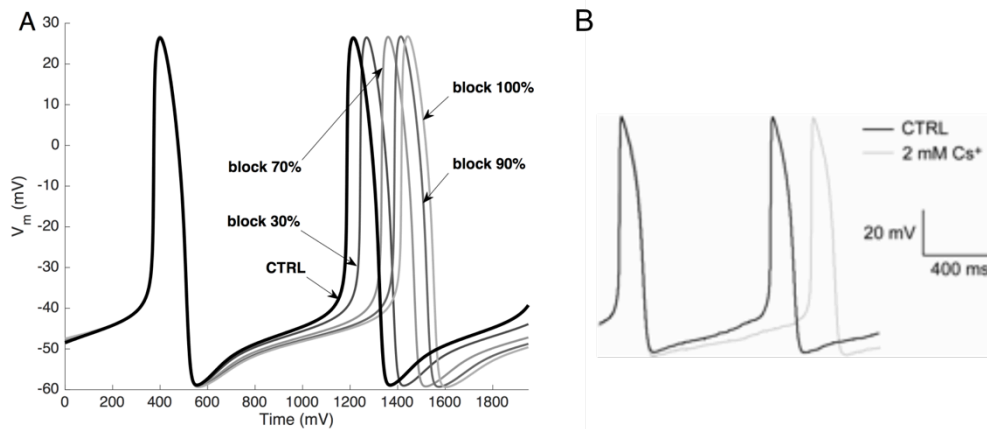


Figure 2.1: Functional effect of I_f block

A) Simulated AP under control conditions (CTRL) and upon 30%, 70%, 90% and full block of I_f . B) Effect of administration of Cs^+ (2 mM) on the AP of an isolated human SAN myocyte. Experimental trace adapted from Verkerk et al. (2007b).

Negative shifts of the steady-state activation curve led to an increase in CL, up to 957 ms (+17.6% with respect to control) with a -15 mV shift, whereas positive shifts shortened CL, up to 577 ms (-29.1%) with a $+15$ mV shift (Fig. 2.2A). As with the I_f block, DDR_{100} was the main descriptive parameter that changed (to 37.7 mV s^{-1} (-21.6%) with a -15 mV shift and to 75.4 mV s^{-1} ($+56.8\%$) with a $+15$ mV shift; Fig. 2.2B), whereas APD_{90} and MDP remained almost unaffected, as for the I_f block (Fig. 2.2, C and D).

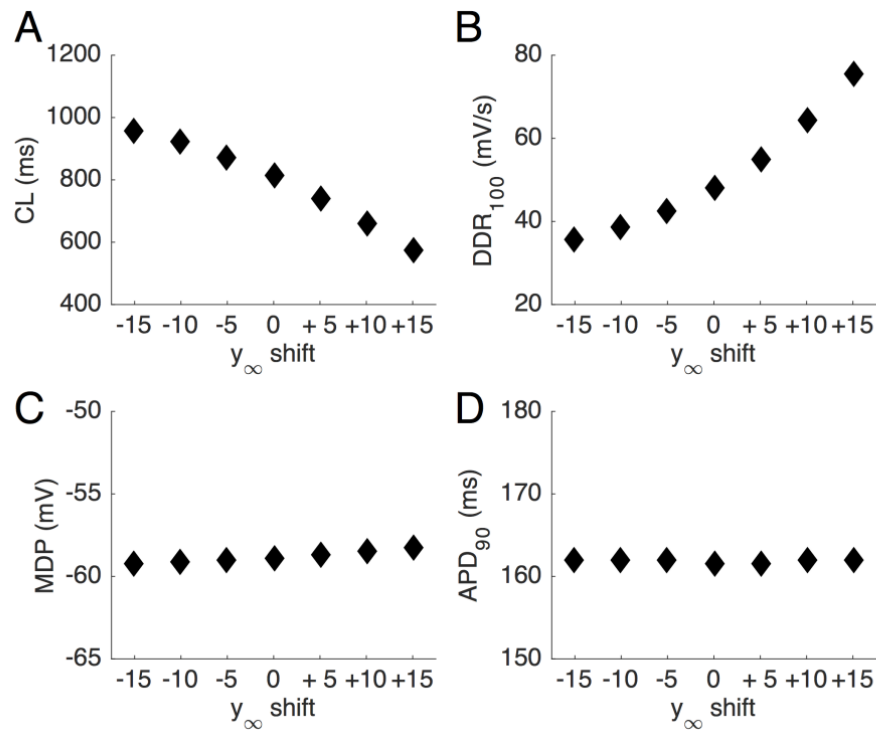


Figure 2.2: Functional effect of changes in voltage dependence of I_f activation
 Simulations of the effect of -15 to $+15$ mV shifts (with steps of 5 mV) in voltage dependence of the y_{∞} steady-state activation curve of the funny current on (A) cycle length, (B) DDR_{100} , (C) MDP and (D) APD_{90} .

2.3.2 Contribution of I_{NaCa} to pacemaking and spontaneous calcium oscillations

The Na^+/Ca^{2+} exchanger is an important actor in the generation of the AP and also contributes to the diastolic depolarization phase. To assess the impact that I_{NaCa} has on CL, we performed a progressive reduction of the maximal activity of Na^+/Ca^{2+} (K_{NaCa}) (Fig. 2.3). Reductions in K_{NaCa} of 50% and 75% unexpectedly led to faster pacemaking, with a rate of $83 \text{ beats min}^{-1}$ (+12.2%) and $93 \text{ beats min}^{-1}$ (+25.7%), respectively. DDR_{100} , APD_{90} and MDP contributed synergistically towards a shorter CL: DDR_{100} increased remarkably, APD_{90} shortened and MDP depolarized (Fig. 2.3A). DDR_{100} was steeper as a result of a more intense I_{NaCa} density during DD (Fig. 2.3, B and D) because of a higher concentration of $[Ca^{2+}]_i$ in the cell (Fig. 2.3C). The reduced maximal activity of the Na^+/Ca^{2+} exchanger

also resulted in a lower contribution of I_{NaCa} to the AP: the overshoot potential was lower and repolarization was faster, resulting in a shorter APD.

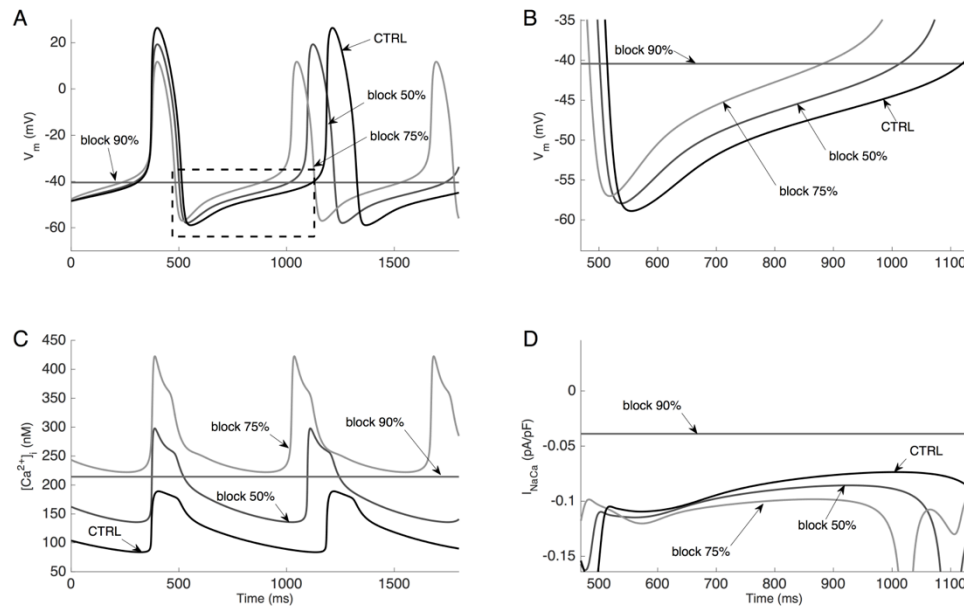


Figure 2.3: Functional effect of I_{NaCa} block

(A) Simulated AP and (C) associated $[Ca^{2+}]_i$ time course under control conditions (CTRL) and upon 50%, 75% and 90% block of I_{NaCa} . (B) Simulated AP and (D) associated I_{NaCa} time course relative to the dashed box of panel A.

Higher levels of block of the exchanger (reduction of maximal activity by 90%) stopped the automaticity of the cell. The inward current provided by the Na^+/Ca^{2+} exchanger was no longer sufficient to make the cell reach its threshold potential for an AP. Membrane potential stabilized at a level approaching -40 mV (Fig. 2.3, A and B), whereas $[Ca^{2+}]_i$ stabilized at a constant value close to 200 nM (Fig. 2.3C).

The presence in the model of the ‘isolated Ca^{2+} oscillator’ was also tested, by repeating the simulations with all membrane currents set to zero. Figure 2.4 depicts the results of the behavior of the ‘isolated Ca^{2+} oscillator’. Spontaneous oscillations of intracellular (Fig 2.4A) and subsarcolemmal Ca^{2+} (Fig 2.4B) were observed upon a large increase in the SERCA pump activity. Notably, the frequency of these oscillations was definitely higher than the physiological human

heart rate (>5 Hz). In particular, calcium oscillations were not sustained for P_{up} values up to more than 90 nM s^{-1} ; sustained oscillations, with a frequency of 5 Hz, arose upon further increasing P_{up} to a value approaching 100 nM s^{-1} . This frequency stayed almost constant as P_{up} was even further increased to 120 nM s^{-1} , suggesting that it might be not easy to tune the oscillation rate in a robust way, at least in this lumped-parameter model of calcium handling.

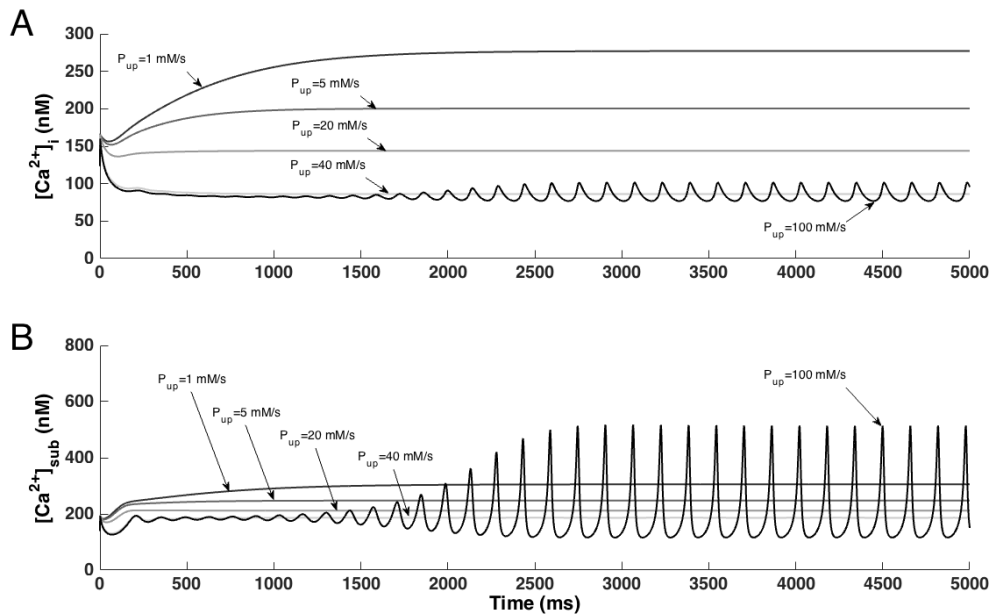


Figure 2.4: Isolated Ca^{2+} oscillator

Timecourse of Ca^{2+} in the intracellular compartment (A) and in the subspace (B) for SR isolated from the membrane. Different level of the maximal activity of SERCA pump $P_{up} = 1, 5, 20, 40$ and 100 mM/s were tested.

2.3.3 Autonomic modulation of pacemaking

The simulated administration of 10 nM ACh resulted in a reduction of spontaneous rate by 21.6% (from 74 to $58 \text{ beats min}^{-1}$). DDR_{100} was decreased by 9.8% (from 48.1 to 43.4 mV/s) and APD_{90} was shortened from 161.5 to 154 ms (-4.6%); MDP was not altered. Even though ACh had opposing effects on

DDR₁₀₀ and APD₉₀, the increase in CL (from 814 in CTRL to 1028 ms with 10 nM ACh) showed that the DDR₁₀₀ reduction prevailed (Fig. 2.5A).

We also assessed the contribution of each individual ion current by applying the ACh effect to each current separately. Changes in I_{K,ACh} and I_f were dominant, inducing a reduction in the pacemaking rate of 12.2% and 6.8%, respectively. Exposure of only I_{CaL} to ACh resulted in a minor effect (1.3% reduction of pacemaking rate), whereas the modification of J_{up} led to negligible changes.

These results are consistent with predictions on the effects on CL due to the changes occurring to P_{CaL}, P_{up}, and I_f that could have been made based on the sensitivity analysis performed in Chapter 1 (through the coefficients that correlate the parameters to the feature [r(parameter,feature)]). Indeed, the decrease of P_{CaL} (-3.1%) was responsible for a CL increase of 1.1%, compatible with r(P_{CaL},CL) = -0.15, that highlights a slight negative correlation. The almost negligible effect on CL (-0.2%) due to the decrease of P_{up} (-7%) was confirmed by the very low value of r(P_{up},CL) = 0.03. The shift of y towards more negative potentials (-5 mV) is consistent with the effect on CL due to a reduction of g_f.

Simulating the ACh effects on all targets but one led to similar results: I_{K,ACh} and I_f played a primary role, as demonstrated by the model-predicted reduction of the pacemaking rate by 8.1% and 13.5% (when I_{K,ACh} and I_f were the only unchanged currents), respectively.

The overall effect induced by 1 μM Iso resulted in an increase in the pacemaking rate of 27.0% to 94 beats min⁻¹ (Fig. 2.5A). DDR₁₀₀ increased from 48.1 mV s⁻¹ in control conditions to 53.4 mV s⁻¹ with Iso, whereas APD₉₀ and MDP were almost unchanged.

The assessment of the effect of Iso through each of the Iso-sensitive currents alone showed that the modified I_f and I_{CaL} both led to a substantial increase in pacemaking rate (13.5% and 25.7%, respectively). The increased activity of I_{NaK}, on the other hand, slowed the pacemaking rate (-13.5%), whereas Iso-induced changes in I_{Ks} and J_{up} only had a small effect (+1.4% and -1.3%, respectively).

The decrease of CL due to a positive shift (+7.5 mV) of the activation gate y is consistent with the effect due to an increase of g_f. The resulting decrease of CL (from 814 to 700 ms, -14.0%) due to the changes occurring to I_{CaL} is caused by

the counteracting effects of the increase of P_{CaL} (+23%, $r(P_{CaL}, CL) = -0.15$) and the shift towards more negative potentials of dL_{∞} (-8 mV, $r(\text{shift}_{dL}, CL) = 0.4$) – which tend to shorten the CL– and the decrease of the slope factor of dL_{∞} (-27%, $r(k_{dL}, CL) = -0.94$), which tends to prolong the CL. The increased activity of the Na^+/K^+ pump (+20% $I_{NaK, \text{max}}$) led to an increase of CL (CL = 937 ms, +15,1%) with $r(I_{NaK}, CL) = 0.12$. The contribution of I_{Ks} to CL decrease (CL = 802 ms, -1.5%) was mainly attributable to the shift of the steady state curve n_{∞} (-14 mV) since the increase of g_{Ks} (+20%) had an almost negligible effect on CL [$r(g_{Ks}, CL) = 0.02$]. Finally, the increase of P_{up} (+25%) was responsible for the slight increase of CL (CL = 818 ms, +0.4%) accordingly with $r(P_{up}, CL) = 0.03$.

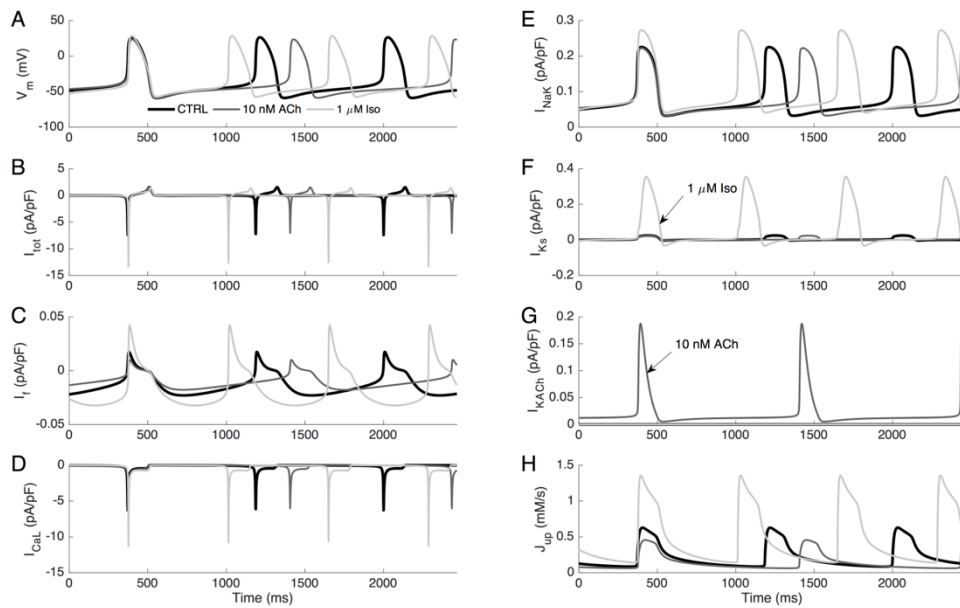


Figure 2.5: Functional effect of acetylcholine and isoprenaline

Time course of (A) membrane potential, (B) net current, target currents (C-G) and SERCA-pump uptake (H) in control conditions (CTRL, black lines), upon administration of ACh 10 nM (dark grey lines) and 1 μ M Iso (light grey lines). Targets for ACh are I_f , I_{CaL} , $I_{K,ACh}$ and J_{up} ; targets for Iso are I_f , I_{CaL} , I_{NaK} , I_{Ks} and J_{up} . Note differences in ordinate scales.

Considering the effects of all currents but one confirmed the above results; when all the currents but one, either I_{CaL} , I_f , I_{NaK} , I_{Ks} or J_{up} , were affected by 1 μ M Iso, an increase in beating rate equal to 1.4%, 9.5%, 43.2%, 21.3% and 28.4%, respectively, was observed. Of note, these values also show that I_{Ks} becomes more prominent at higher rates, when there is less time for its deactivation. The effect of I_{Ks} alone is small, with a 1.4% increase in beating rate, although the ‘all but one’ data (20.3% increase) reveal a more prominent role of I_{Ks} at higher rates; indeed, the net contribution of I_{Ks} (overall effect – all but I_{Ks} effect) shows an increase of beating rate equal to 6.7% (27.0–20.3%).

The model was capable of reproducing the full clinical range of human heart rate, assumed to be from 40 to 180 beats min^{-1} . In particular, the model predicted that a concentration of ACh equal to 25 nM was able to slow down the

pacemaking rate to 40 beats min^{-1} (-45.9%). This concentration was responsible for a negative shift in the voltage dependence of the I_f steady-state activation curve y_∞ and time constant τ_y of -6.3 mV, a reduction of the maximal I_{CaL} permeability P_{CaL} equal to -6.7% , and a 15% decrease in the maximal activity of the SERCA pump P_{up} , all with respect to control conditions. The $I_{\text{K,ACh}}$ was also affected, showing a peak value of 0.33 pA/pF.

The model also showed stable oscillations at a pacing frequency equal to 182 beats min^{-1} . Changes in the Iso target parameters responsible for this pacemaking rate were quantified (with respect to control conditions) as: y_∞ and τ_y were shifted by +12 mV; $I_{\text{NaK,max}}$ and g_{Ks} were both increased by 92%; and n_∞ and τ_n were shifted by -22 mV. I_{CaL} was affected by a 96.8% increase of P_{CaL} , a shift of dL_∞ and τ_{dL} by -12.8 mV, and a slope factor k_{dL} reduced by -29.7% . Thus, we directly tuned the parameters affected by Iso, increasing the aforementioned effects of 1 μM Iso to arrive at a pacemaking rate approaching 180 beats min^{-1} .

2.4 Discussion

Simulating I_f and NCX blocks and autonomic stimulation provided insights into the model behavior and shed light on underlying phenomena.

Lower levels of I_f block and shifts of the steady-state activation curve were able to modulate pacemaking rate, mainly by varying DDR_{100} . By contrast, MDP and APD_{90} showed no changes (Figs. 2.1 and 2.2). These results suggest that I_f exerts its capability to modulate beating rate during the DD phase. As previously shown for the rabbit SAN AP (Severi *et al.*, 2012), controlling the steepness of early DD is an efficient way of determining beating rate: small changes in currents are able to substantially modify the slope of DD, and thus the overall duration of the AP. This is even more true in human SAN because the pacing rate is even more sensitive to changes in DD slope. As a result of the non-linear relationship between dV/dt and time (Zaza, 2016), the same change in current is bound to produce larger changes in CL when basal CL is longer. Unlike the parent model,

pacemaker activity does not cease when I_f is fully blocked. Yet, the modulatory role of I_f is as important as in the parent model.

NCX provided an important contribution to automaticity, both during DD and during the AP upstroke. The considerable reduction of its maximal activity relative to the parent model, consistent with the gene expression pattern reported by Chandler *et al.* (2009), allowed $[Ca^{2+}]_i$ to reach a value closer to experimental values. The NCX block showed two different effects: for low-to-moderate levels of block, the beating rate became faster than under control conditions, whereas for high-to-almost-full block, the automaticity stopped (Fig. 2.3). The latter result is consistent with experiments showing an inhibitory effect of Na^+ replacement by Li^+ , thus abolishing NCX, on spontaneous beating in rabbit SAN cells (Bogdanov *et al.*, 2001). The unexpected effect of rate acceleration upon low-to-moderate block can be the result of a counterintuitive, although physiological, process: a lower maximal NCX activity results in a higher $[Ca^{2+}]_i$ during DD and, consequently, a more intense I_{NaCa} . Nevertheless, the rate increase induced by I_{NaCa} reduction is actually a prediction of our model, and experimental data (not available yet) are needed to confirm this prediction in human SAN cells.

Unlike I_f modulation, NCX block affected several main features of the action potential: DDR_{100} , MDP, APD_{90} and even APA underwent considerable changes (Fig. 2.3). Of note, both the absolute and relative amplitude of I_f and I_{NaCa} during DD were highly similar to those predicted by Verkerk *et al.* (2013) through numerical reconstruction.

It is worth noting that the ‘calcium clock’ was integrated in the parent model and it is also present in this human model but, as expected, the NCX current cannot effectively modulate the pacemaking rate. Based on the rabbit model simulations, the SERCA pump activity could be expected to modulate pacemaking rate. This was not the case in our model, in which changes in SERCA maximal activity had a negligible effect on rate. This leaves open the question about the actual relevance of the ‘calcium clock’ in human SAN.

The adopted calcium handling considered the presence of a subsarcolemmal space, which is also present in the rabbit SAN cell models of Kurata *et al.*, (2002), Maltsev & Lakatta, (2009) and Severi *et al.* (2012). Because T-tubules are poorly

defined in SAN cells, this subsarcolemmal space is proposed as a ‘fuzzy space’ (Lederer *et al.*, 1990). NCX1 and RyRs are co-located there, as reported by Lyashkov *et al.* (2007), who used immunolabelling techniques and confocal imaging. Through further simulations, we tested the effect of a different cell arrangement of RyRs in the cell space. We progressively switched the SR release from the subspace to the cytosol until a 100% Ca^{2+} release, targeted to the cytosol and thus sensitive to Ca_i instead of Ca_{sub} , was reached. The model did not show dramatic changes; in an SR release configuration fully targeted to cytosol, we only observed a minor change of pacemaking rate (+5.4%; from 74 to 78 beats min^{-1}), as well as a minor increase in Ca_i ($\text{Ca}_{i,\text{min}}$ from 84 to 99 nM, $\text{Ca}_{i,\text{max}}$ from 189 to 199 nM).

The only study to report experimental data on the administration of ACh and Iso in human SAN tissue was carried out by Drouin (1997). However, the observed intrinsic pacemaking frequency was not coherent with clinical observations (30 beats min^{-1} in vitro vs. 70–112 beats min^{-1} in situ); it is therefore most probable that the effects of ACh and Iso were exacerbated. Furthermore, ACh and Iso targets are not electrophysiologically characterized in humans, and so we used experimental data from rabbit SAN. Thus, our simulations of ACh and Iso effects provide theoretical insights about the mechanisms underlying autonomic modulation that may require updates with respect to future data that become available from human tissue. The administration of 10 nM ACh led to a reduction of the pacemaking rate as a result of the activation of $I_{K,\text{ACh}}$ together with changes to I_f , SR uptake and I_{CaL} . The ACh-induced reduction of I_f and activation of $I_{K,\text{ACh}}$ appeared to be the major determinants of rate slowdown.

The overall pacing rate acceleration, as a result of the administration of 1 μM Iso, was the result of a balance between opposing contributors. An assessment of the role of each of the five targets (I_f , I_{NaK} , I_{CaL} , I_{Ks} and SR uptake) showed that both I_f and I_{CaL} changes led to a faster beating rate. However, the underlying mechanisms were different: I_f worked on the early phase of DD, modifying DDR_{100} (also shown in I_f modulation caused by shifts in voltage dependence), whereas I_{CaL} exerted its effect during late DD. I_{NaK} showed an enhanced activity with Iso that decreased DDR and therefore counteracted the overall pacing rate

acceleration.

An important test of the validity of the model was its ability to reproduce the clinical range of human heart rate. Our model was able to provide stable automaticity at 40 beats min^{-1} upon administration of 25 nM of ACh, whereas the maximum rate (180 beats min^{-1}) was obtained by enhancing the effects of Iso on its target parameters.

The overall message from model-based simulations of autonomic modulation of pacemaking is that I_f plays an important role in rate regulation, as in rabbit. However, at least one other current ($I_{K,ACh}$ for ACh and I_{CaL} for Iso administration) needs to be modulated to achieve pacemaking rate regulation in the full physiological range.

References

- Barbuti A & DiFrancesco D (2008). Control of Cardiac Rate by “Funny” Channels in Health and Disease. *Ann N Y Acad Sci* 1123, 213–223.
- Bogdanov KY, Maltsev VA, Vinogradova TM, Lyashkov AE, Spurgeon HA, Stern MD & Lakatta EG (2006). Membrane potential fluctuations resulting from submembrane Ca^{2+} releases in rabbit sinoatrial nodal cells impart an exponential phase to the late diastolic depolarization that controls their chronotropic state. *Circ Res* 99, 979–987.
- Bogdanov KY, Vinogradova TM & Lakatta EG (2001). Sinoatrial Nodal Cell Ryanodine Receptor and Na^{+} - Ca^{2+} Exchanger Molecular Partners in Pacemaker Regulation. *Circ Res* 88, 1254–1258.
- Bucchi A, Baruscotti M, Robinson RB & DiFrancesco D (2007). Modulation of rate by autonomic agonists in SAN cells involves changes in diastolic depolarization and the pacemaker current. *J Mol Cell Cardiol* 43, 39–48.
- Cerbai E, Barbieri M & Mugelli A (1994). Characterization of the hyperpolarization-activated current, $I(f)$, in ventricular myocytes isolated from hypertensive rats. *J Physiol* 481, 585–591.
- Cerbai E, Sartiani L, DePaoli P, Pino R, Maccherini M, Bizzarri F, DiCiolla F, Davoli G, Sani G & Mugelli A (2001). The Properties of the Pacemaker Current I_f in Human Ventricular Myocytes are Modulated by Cardiac Disease. *J Mol Cell Cardiol* 33, 441–448.
- Chandler NJ, Greener ID, Tellez JO, Inada S, Musa H, Molenaar P, DiFrancesco

- D, Baruscotti M, Longhi R, Anderson RH, Billeter R, Sharma V, Sigg DC, Boyett MR & Dobrzynski H (2009). Molecular architecture of the human sinus node insights into the function of the cardiac pacemaker. *Circulation* 119, 1562–1575.
- Denyer JC & Brown HF (1990). Pacemaking in rabbit isolated sino-atrial node cells during Cs⁺ block of the hyperpolarization-activated current if. *J Physiol* 429, 401–409.
- DiFrancesco D (1985). The cardiac hyperpolarizing-activated current, if. origins and developments. *Prog Biophys Mol Biol* 46, 163–183.
- DiFrancesco D, Brown HF & Noble SJ (1979). How does adrenaline accelerate the heart? *Nature* 280, 235.
- DiFrancesco D, Ferroni A, Mazzanti M & Tromba C (1986). Properties of the hyperpolarizing-activated current (if) in cells isolated from the rabbit sino-atrial node. *J Physiol* 377, 61–88.
- DiFrancesco D & Tromba C (1987). Acetylcholine inhibits activation of the cardiac hyperpolarizing-activated current,if. *Pflug Arch* 410, 139–142.
- DiFrancesco D & Tromba C (1988a). Inhibition of the hyperpolarization-activated current (if) induced by acetylcholine in rabbit sino-atrial node myocytes. *J Physiol* 405, 477–491.
- DiFrancesco D & Tromba C (1988b). Muscarinic control of the hyperpolarization-activated current (if) in rabbit sino-atrial node myocytes. *J Physiol* 405, 493–510.
- Drouin E (1997). Electrophysiologic properties of the adult human sinus node. *J Cardiovasc Electrophysiol* 8, 254–258.
- Hodgkin AL & Huxley AF (1952). A quantitative description of membrane current and its application to conduction and excitation in nerve. *J Physiol* 117, 500–544.
- Hüser J, Blatter LA & Lipsius SL (2000). Intracellular Ca²⁺ release contributes to automaticity in cat atrial pacemaker cells. *J Physiol* 524, 415–422.
- Kurata Y, Hisatome I, Imanishi S & Shibamoto T (2002). Dynamical description of sinoatrial node pacemaking: improved mathematical model for primary pacemaker cell. *Am J Physiol - Heart Circ Physiol* 283, H2074–H2101.
- Lakatta EG & DiFrancesco D (2009). What keeps us ticking: a funny current, a calcium clock, or both? *J Mol Cell Cardiol* 47, 157–170.

- Lederer WJ, Niggli E & Hadley RW (1990). Sodium-calcium exchange in excitable cells: fuzzy space. *Science* 248, 283.
- Liu J, Dobrzynski H, Yanni J, Boyett MR & Lei M (2007). Organisation of the mouse sinoatrial node: structure and expression of HCN channels. *Cardiovasc Res* 73, 729–738.
- Liu YM, Yu H, Li CZ, Cohen IS & Vassalle M (n.d.). Cesium effects on $i(f)$ and $i(k)$ in rabbit sinoatrial node myocytes: implications for Sa node automaticity. *J Cardiovasc Pharmacol* 32, 783–790.
- Lyashkov AE, Juhaszova M, Dobrzynski H, Vinogradova TM, Maltsev VA, Juhasz O, Spurgeon HA, Sollott SJ & Lakatta EG (2007). Calcium Cycling Protein Density and Functional Importance to Automaticity of Isolated Sinoatrial Nodal Cells Are Independent of Cell Size. *Circ Res* 100, 1723–1731.
- Lyashkov AE, Vinogradova TM, Zahanich I, Li Y, Younes A, Nuss HB, Spurgeon HA, Maltsev VA & Lakatta EG (2009). Cholinergic receptor signaling modulates spontaneous firing of sinoatrial nodal cells via integrated effects on PKA-dependent Ca^{2+} cycling and IKACH. *Am J Physiol - Heart Circ Physiol* 297, H949–H959.
- Maltsev VA & Lakatta EG (2009). Synergism of coupled subsarcolemmal Ca^{2+} clocks and sarcolemmal voltage clocks confers robust and flexible pacemaker function in a novel pacemaker cell model. *Am J Physiol - Heart Circ Physiol* 296, H594–H615.
- Mattick P, Parrington J, Odia E, Simpson A, Collins T & Terrar D (2007). Ca^{2+} -stimulated adenylyl cyclase isoform AC1 is preferentially expressed in guinea-pig sino-atrial node cells and modulates the I_f pacemaker current. *J Physiol* 582, 1195–1203.
- Rigg L & Terrar D (1996). Possible role of calcium release from the sarcoplasmic reticulum in pacemaking in guinea-pig sino-atrial node. *Exp Physiol* 81, 877–880.
- Robinson RB, Yu H, Chang F & Cohen IS (1997). Developmental change in the voltage-dependence of the pacemaker current, i_f , in rat ventricle cells. *Pflug Arch* 433, 533–535.
- Severi S, Fantini M, Charawi LA & DiFrancesco D (2012). An updated computational model of rabbit sinoatrial action potential to investigate the mechanisms of heart rate modulation. *J Physiol* 590, 4483–4499.

- Tellez JO, Dobrzynski H, Greener ID, Graham GM, Laing E, Honjo H, Hubbard SJ, Boyett MR & Billeter R (2006). Differential Expression of Ion Channel Transcripts in Atrial Muscle and Sinoatrial Node in Rabbit. *Circ Res* 99, 1384–1393.
- Verkerk AO, van Borren MMGJ & Wilders R (2013). Calcium transient and sodium-calcium exchange current in human versus rabbit sinoatrial node pacemaker cells. *Sci World J* 2013, e507872.
- Verkerk AO, Wilders R, Borren MMGJ van, Peters RJG, Broekhuis E, Lam K, Coronel R, Bakker JMT de & Tan HL (2007). Pacemaker current (I_f) in the human sinoatrial node. *Eur Heart J* 28, 2472–2478.
- Vinogradova TM, Bogdanov KY & Lakatta EG (2002). beta-Adrenergic stimulation modulates ryanodine receptor Ca²⁺ release during diastolic depolarization to accelerate pacemaker activity in rabbit sinoatrial nodal cells. *Circ Res* 90, 73–79.
- Vinogradova TM, Lyashkov AE, Zhu W, Ruknudin AM, Sirenko S, Yang D, Deo S, Barlow M, Johnson S, Caffrey JL, Zhou Y-Y, Xiao R-P, Cheng H, Stern MD, Maltsev VA & Lakatta EG (2006). High Basal Protein Kinase A-Dependent Phosphorylation Drives Rhythmic Internal Ca²⁺ Store Oscillations and Spontaneous Beating of Cardiac Pacemaker Cells. *Circ Res* 98, 505–514.
- Vinogradova TM, Sirenko S, Lyashkov AE, Younes A, Li Y, Zhu W, Yang D, Ruknudin AM, Spurgeon H & Lakatta EG (2008). Constitutive Phosphodiesterase Activity Restricts Spontaneous Beating Rate of Cardiac Pacemaker Cells by Suppressing Local Ca²⁺ Releases. *Circ Res* 102, 761–769.
- Vinogradova TM, Zhou Y-Y, Bogdanov KY, Yang D, Kuschel M, Cheng H & Xiao R-P (2000). Sinoatrial Node Pacemaker Activity Requires Ca²⁺/Calmodulin-Dependent Protein Kinase II Activation. *Circ Res* 87, 760–767.
- Yasui K, Liu W, Opthof T, Kada K, Lee J-K, Kamiya K & Kodama I (2001). I_f Current and Spontaneous Activity in Mouse Embryonic Ventricular Myocytes. *Circ Res* 88, 536–542.
- Younes A, Lyashkov AE, Graham D, Sheydina A, Volkova MV, Mitsak M, Vinogradova TM, Lukyanenko YO, Li Y, Ruknudin AM, Boheler KR, van Eyk J & Lakatta EG (2008). Ca²⁺-stimulated basal adenylyl cyclase activity localization in membrane lipid microdomains of cardiac sinoatrial nodal pacemaker cells. *J Biol Chem* 283, 14461–14468.

Zaza A (2016). Electrophysiology meets geometry. *Europace* 18, 317–317.

Zaza A, Micheletti M, Brioschi A & Rocchetti M (1997). Ionic currents during sustained pacemaker activity in rabbit sino-atrial myocytes. *J Physiol* 505, 677–688.

Chapter 3

Model validation through the simulation of ion channel mutations

The content of this chapter is published in:

“Computational analysis of the human sinus node action potential: model development and effects of mutations”

Alan Fabbri¹, Matteo Fantini¹, Ronald Wilders² and Stefano Severi¹

The Journal of Physiology, J Physiol 2017, 595 (7) 2365-2396

“Bradycardic effects of mutations in the HCN4 gene at different levels of autonomic tone in humans”

Alan Fabbri¹, Arie O. Verkerk², Ronald Wilders² and Stefano Severi¹

Computing in Cardiology 2017, in press

¹ Computational Physiopatology Unit, Department of Electrical, Electronic and Information Engineering “Guglielmo Marconi”, University of Bologna, Cesena, Italy

² Department of Anatomy, Embryology and Physiology, Academic Medical Center, University of Amsterdam, Amsterdam, The Netherlands

Abstract

Sick Sinus Syndrome (SSS) consists in the impairment of SAN automaticity and conduction of the AP towards the surrounding atrium. SSS leads to sinus bradycardia, sinus arrest and sinus exit blocks and it accounts for 50% of the electrical pacemaker implantations.

Clinical studies on families affected by sinus arrhythmias shed light on the genetic linkage between SSS and mutations in the *HCN4*, *SCN5A* and *KCNQ1* genes, encoding pore-forming subunits of the I_f , I_{Na} and I_{Ks} channels, respectively.

Aim of this chapter is to validate the human SAN model comparing the effects of ion channel mutations on simulated beating rate with heart rate data collected in clinical studies.

The functional characterization of mutations in *HCN4*, *SCN5A* and *KCNQ1* was incorporated into the human SAN AP model. Several clinically observed mutations have been electrophysiologically characterized through in vitro experiments, revealing voltage shifts and changes of slope for steady state activation and inactivation curves as well as changes in maximal conductance. The basal beating rate in wild-type simulations was modulated in order to match with the heart rate of the non-carrier subjects.

The simulated changes of beating rate due to ion channel mutations are qualitatively in agreement, even if quantitatively less prominent, with clinical data.

The presence of the hyperpolarizing action of the surrounding atria in situ and the limitations of functional characterizations carried out on different expression systems could be the reason of the apparent gap between simulated and clinical data.

3.1 Introduction

Sick Sinus Syndrome (SSS) consists in the inability of the sinoatrial node to perform its pacemaking function due to a disorder of automaticity or the inadequate transmission of the AP from the SAN tissue towards the surrounding atrium (Bigger & Reiffel, 1979).

In clinical practice, SSS can be detectable within the ECG trace as sinus bradycardia, sinus arrest, SAN exit block, and chronotropic incompetence, and is responsible for half of the total amount of electrical pacemaker implantations (Lamas *et al.*, 2002).

Since the 1960s-1970s, literature has reported SSS observed in familial context, but the linkage between SSS and genetic mutations became clear only in the late 1990s and the beginning of 2000s. Benson *et al.* (2003) and Schulze-Bahr *et al.* (2003) provided a molecular interpretation of SSS linking mutations in the *SCN5A* (sodium channel voltage gated, type 5, α subunit) and *HCN4* (hyperpolarization-activated cyclic-nucleotide gated type 4) genes, encoding the pore-forming subunits of the I_{Na} and I_f channels, respectively, to this SAN dysfunction.

In cardiac tissue, four isoforms compose the HCN family (HCN1-4) and HCN4 is the more abundant of these family members in pacemaker cells. I_f channel is a tetramer composed of four HCN subunits and it could be present in the homomeric or heteromeric form.

Each HCN4 subunit consists of six trans-membrane subunits (S1-S6) where S4 fulfills the voltage sensor function; the P domain, which links S5 and S6, is the pore-forming region. The C-terminus of the HCN4 protein contains the C-linker and the cyclic-Nucleotide Binding Domain (cNBD), where cAMP can bind, mediating the autonomic stimulation. In vitro experiments showed that HCN4 mutations can impair the physiological behavior of I_f in several ways: they can modify the ion channel kinetics through a voltage shift or a change in the slope of the activation curve (Nof *et al.*, 2007; Laish-Farkash *et al.*, 2010; Duhme *et al.*, 2013), they can affect the sensitivity to cAMP, causing chronotropic incompetence (Schweizer *et al.*, 2014), or they can lead to the reduction of the

maximal conductance g_f , due to a compromised protein trafficking from the nucleus to the cell membrane (Ueda *et al.*, 2004; Nof *et al.*, 2007; Laish-Farkash *et al.*, 2010). For a comprehensive review on mutations affecting HCN4 and their effect on human I_f see the reviews by Verkerk & Wilders (2014, 2015).

Cardiac tetrodotoxin (TTX) resistant sodium channels ($Na_v1.5$) are composed of a single pore-forming α subunit, encoded by the *SCN5A* gene, and a modulatory one, the β subunit, from a family consisting of $\beta1-4$ isoforms, encoded by the *SCN1B-SCN4B* genes, respectively.

Four homologous domains (DI-DIV) build up the α subunit: each domain comprises six transmembrane segments (S1-S6) connected through extracellular and cytoplasmic loops. Segment S4 works as voltage sensor and the P loops that link the S5-S6 subunits are supposed to be the selective filter of the channel.

Mutations affecting *SCN5A* are frequently associated to multiple cardiac diseases, e.g. long QT type 3 (LQT3) syndrome and Brugada Syndrome (BrS). Loss of function mutations in *SCN5A*, i.e. mutations that reduce I_{Na} , can affect pacemaking and the propagation of AP, causing sinus bradycardia, slow SAN conduction and sino-atrial exit block, symptoms often observed in SSS.

Gain of function mutations in *SCN5A* are associated with LQT3 syndrome. In several mutations [e.g. Δ KPQ (Moss *et al.*, 1995; Nagatomo *et al.*, 1998), E1784K (Deschênes *et al.*, 2000; Makita *et al.*, 2008), 1795insD (Bezzina *et al.*, 1999; Veldkamp *et al.*, 2003)] LQT3 syndrome occurs in combination with sinus arrhythmias; of note, sinus bradycardia could exacerbate the QT prolongation representing an indirect factor to the predisposition to lethal arrhythmias. The cellular basis of sinus dysfunction in LQT3 was investigated by Veldkamp *et al.* (2003) providing the characterization of the 1795insD mutation in heterologous system and assessing its contribution to the SAN AP through computer simulations. The incomplete sodium channel inactivation led to the presence of a late current ($I_{Na,L}$) that caused AP prolongation and thus an increase of CL, compatible with the sinus bradycardia present in 1795insD mutation carriers.

Contrary to I_f and I_{Na} , I_{Ks} is an outward current and exerts its role mainly during the AP. The $K_v7.1$ channel, encoded by the *KCNQ1* gene, is assembled by four α subunits, each of which is composed of six transmembrane segments (S1-

S6). S4 carries out the role of voltage sensor, whereas the conductive pore is formed by S5-S6 and the linking P-loop. Mutations can lead to the increase of I_{Ks} (gain of function) or a lower contribution of that current (loss of function). Since I_{Ks} is a repolarizing current, gain of function mutations are responsible for short QT syndrome, whereas loss of function mutations are for long QT. Among *KCNQ1* mutations associated to sinus bradycardia, R231C (Henrion *et al.*, 2012) and V241F (Ki *et al.*, 2013) affect the S4 domain (belonging to the voltage sensor) and cause gain of function; Δ F339 is located in the pore-forming region (segment S6) and is responsible for loss of function of I_{Ks} (Thomas *et al.*, 2005).

Aim of this chapter is to validate the computational human SAN model presented Chapter 1 assessing the effects of ion channel mutations on action potential features.

To this end, the electrophysiological characterization of mutations affecting I_f , I_{Na} and I_{Ks} were incorporated into the model and the resulting beating rate was compared with the available clinical data. Moreover, the effects of mutations affecting the HCN4 channel were assessed at low, basal and high beating rates in case clinical data were available for comparison.

3.2 Methods

3.2.1 Functional effects of mutations

Mutations in genes encoding (subunits of) ion channels may lead to changes in electrophysiological properties. We incorporated such functional effects into our human SAN cell model by modifying the parameters of the affected ion channel according to values reported in the literature (Tables 3.1–3.3). Only studies reporting changes in heart rate as (one of) the clinical effects of the mutations were included.

The altered functionality was implemented as a shift of the steady-state

(de)activation or inactivation curve, a change in its slope factor or a reduction in maximal conductance. Mutations may also cause a change in the voltage-dependent time constant (τ) curve. When changes in the time constant had been experimentally reported, they were implemented by a constant multiplication factor. Otherwise, τ underwent the same voltage shift as applied to the steady-state (in)activation curve. Finally, mutations can also affect the maximal conductance ($g_{i,max}$) of ion channels.

When I_{Na} channels are incompletely inactivated, an additional non-inactivating term is added to the control formulation of I_{Na} , to reproduce a persistent, ‘late’ inward sodium current ($I_{Na,L}$), which is not normally present in the model.

$I_{Na,L}$ was mathematically formulated as follows:

$$I_{Na,L} = g_{Na,L} m^3 (V - E_{Na}) \quad (3.1)$$

The non-inactivating property was obtained by neglecting the gate h , responsible for the I_{Na} inactivation. The maximal conductance $g_{Na,L}$ was estimated simulating voltage clamp experiments in the same conditions reported in literature (Nagatomo *et al.*, 1998; Deschênes *et al.*, 2000; Veldkamp *et al.*, 2000; Makita *et al.*, 2008). The fast Na^+ current (I_{Na}) was elicited at -20 mV and the peak value was measured ($I_{Na,peak}$). $g_{Na,L}$ was tuned such as the amplitude of $I_{Na,L}$ was equal to the percentage of $I_{Na,peak}$ reported in literature. This method led to $g_{Na,L} = 5.5 \cdot 10^{-5}$, $1.36 \cdot 10^{-4}$, $1.02 \cdot 10^{-4}$, and $1.31 \cdot 10^{-4}$ μS for ΔKPQ , E1784a,b and 1795insD respectively.

3.2.2 HCN4 mutations and autonomic modulation

The bradycardic effect of three HCN4 mutations – G480R, A485V and 695X – on AP SAN was evaluated in presence of vagal tone, β -adrenergic tone and without autonomic stimulation.

The G480R mutation was simulated through a 50% reduction in fully-activated conductance (i.e., a scaling factor of 0.5) and a -15 mV shift in voltage

dependence, whereas a scaling factor of 0.33 and a -30 mV shift were used to simulate the A485V mutation. The loss of cAMP sensitivity in case of the 695X mutation was simulated by a fixed -10.1 mV shift in voltage dependence, in line with the maximum effect of acetylcholine.

The vagal tone stimulation was mimicked simulating the administration of 20 nM ACh. The major effects of the administration of ACh are the activation of the ACh-activated potassium current $I_{K,ACh}$, which is zero in the default model, and the inhibition of I_f through a negative shift in its voltage dependence. The administration of 20 nM ACh lowered the beating rate to 49 beats min^{-1} from the basal rate in control conditions of 74 beats min^{-1} .

A beating rate of 140 beats min^{-1} (β -adrenergic tone) was obtained through the simulated administration of Iso, tuning the parameters affected by Iso to arrive at this beating rate. The simulated effects of Iso included a $+10$ mV shift in the voltage dependence of I_f .

Table 3.1. Changes introduced in the I_f model parameters to reproduce the electrophysiological characteristics of mutant *HCN4* channels, and associated clinically reported heart rate.

<i>Mutation</i>	<i>Type of expression</i>	<i>Expression system</i>	<i>Activation</i>			<i>Current Density (%)</i>	<i>Heart rate (bpm)</i>	<i>Reference</i>
			<i>V_{1/2} shift (mV)</i>	<i>Slope (%)</i>	<i>Tau shift (mV)</i>			
G480R	Heteromeric	Oocyte, HEK	-15	-	-15	-50%	NC : 73 ± 11 C : 48 ± 12	Nof <i>et al.</i> (2007)
Y481H	Heteromeric	CHO	-43.9	n.s.	-43.9	n.s.	IP1 : < 30 IP2 : 40	Milano <i>et al.</i> (2014)
G482R a	Heteromeric	CHO	-38.7	n.s.	-38.7	n.s.	NC : 63 C : 48±10.7	Milano <i>et al.</i> (2014)
G482R b	Heteromeric	HEK	n.s.	n.s.	n.s.	-65%	NC : 63 C : 41± 5	Schweizer <i>et al.</i> (2014)
A485V	Heteromeric	Oocytes, HEK	-30	-	-30	-66.4%	NC : 77 ± 12 C : 58 ± 6	Laish-Farkash <i>et al.</i> (2010)
R524Q	Heteromeric	HEK	+4.2	-	+4.2	n.s.	IP : 98.5 ± 14.2	Baruscotti <i>et al.</i> (2015)
K530N	Heteromeric	HEK	-14.2	n.s.	-14.2	-	NC : 74 C : 60.6 ± 6.9	Duhme <i>et al.</i> (2013)
D553N	Heteromeric	COS	n.s.	n.s.	-	-63%	IP: 39	Ueda <i>et al.</i> (2004)
S672R	Heteromeric	HEK	-4.9	n.s.	-4.9	-	NC : 73.2 ± 1.6 C : 52.2 ± 1.4	Milanesi <i>et al.</i> (2006)

Experimental data are changes relative to wild-type currents. These changes are used to simulate the effect of *HCN4* mutations. Oocytes: *Xenopus* oocytes, HEK: HEK-293 cells, CHO: CHO cells, COS: COS-7 cells. $V_{1/2}$ shift: shift in I_f steady-state activation curve; slope: slope factor of steady-state activation curve; tau shift: shift in voltage dependence of time constant of activation. -: not reported; n.s.: no significant change. Heart rate is resting heart rate in index patient (IP), mutation carriers (C) or non-affected family members (non-carriers, NC).

Table 3.2. Changes introduced in the I_{Na} model parameters to reproduce the electrophysiological characteristics of mutant *SCN5A* channels, and associated clinically reported heart rate.

<i>Mutation</i>	β <i>subunit</i>	<i>Expression system</i>	<i>Activation</i>			<i>Inactivation</i>			I_{Na} <i>Late</i> (%)	<i>Current Density</i> (%)	<i>Heart rate</i> (bpm)	<i>Reference</i>
			$V_{1/2}$ <i>shift</i> (mV)	<i>Slope</i> (%)	<i>Tau shift</i> (mV)	$V_{1/2}$ (mV)	<i>Slope</i> (%)	<i>Tau</i>				
E161K	yes	tsA201	+11.9	+17.9	+11.9	n.s.	n.s.	n.s.	-	-60	NC: 51±0.6 * C: 39±1 *	Smits <i>et al.</i> (2005)
G1406R	yes	COS	-	-	-	-	-	-	-	-100	NC: 74±2 C: 68.4	Kyndt <i>et al.</i> (2001)
ΔKPQ	no	HEK	+9.0	+26.8	+9.0	n.s.	n.s.	n.s.	0.60	-	NC: 76.4 C: 62.1	Nagatomo <i>et al.</i> (1998) Moss <i>et al.</i> (1995)
E1784K a	yes	tsA201	+8.8	+78.1	+8.8	-14.4	n.s.	n.s.	1.5	-	IP: 42	Deschênes <i>et al.</i> (2000)
E1784K b	yes	tsA201	+12.5	+32.6	+12.5	-15.0	n.s.	n.s.	1.85	-40	SND [#]	Makita <i>et al.</i> (2008)
D1790G	yes	HEK	+6	+33.3	+6	-15	-6.8	x0.5	n.s.	-	NC: 64.9 C: 58.6	Wehrens <i>et al.</i> (2000) Benhorin <i>et al.</i> (2000)
1795insD**	yes	HEK/Oocytes	+9.1	n.s.	+9.1	-9.7	n.s.	n.s.	1.4	-77.8	NC: 74.5 ± 13.5 C: 67.5 ± 16.4	Bezzina <i>et al.</i> (1999) Veldkamp <i>et al.</i> (2000)

Experimental data are changes relative to wild-type currents. These changes are used to simulate the effect of *SCN5A* mutations. α , β : subunits α and β constituting the *SCN5A* channel. HEK: HEK-293 cells, COS: COS-7 cells, tsA201: tsA201 cells. $V_{1/2}$: shift in I_{Na} steady-state (in)activation curve; slope: slope factor of steady-state (in)activation curve; tau shift: shift in voltage dependence of time constant of activation; I_{Na} Late: persistent sodium current as percent of peak current under voltage clamp conditions. -: not reported; n.s.: no significant change. Heart rate is resting heart rate in index patient (IP), mutation carriers (C) or non-affected family members (non-carriers, NC). *Absolute minimum heart rate. #Sinus node dysfunction (SND) observed in 16/41 mutation carriers.

** Parameters employed for simulations were selected from two different experimental studies (Bezzina *et al.*, 1999; Veldkamp *et al.*, 2000). In particular, the set of parameters reported by Veldkamp *et al.* (2000) was extended with a depolarizing shift of the activation and a remarkable current density reduction as observed by Bezzina *et al.* (1999).

Table 3.3. Changes introduced in the I_{Ks} model parameters to reproduce the electrophysiological characteristics of mutant *KCNQ1* channels, and associated clinically reported heart rate.

<i>Mutation</i>	<i>Type of expression</i>	<i>Expression system</i>	<i>Activation</i>			<i>Current Density (%)</i>	<i>Heart rate (bpm)</i>	<i>Reference</i>
			<i>V_{1/2} shift (mV)</i>	<i>Slope (%)</i>	<i>Tau (%)</i>			
R231C	Homomeric	Oocytes	-	-	-	Voltage dependent*	C:58.5±7.7	Henrion <i>et al.</i> (2012)
V241F	Homomeric	HEK	-43.2	+52.9	-	-	IP1:30 IP2: 36	Ki <i>et al.</i> (2013)
ΔF339	Heteromeric	Oocytes	+25.0	-	-	-69.5	NC: 63 C: 62.0 ± 6.6	Thomas <i>et al.</i> (2005)

Experimental data are changes relative to wild-type currents. These changes are used to simulate the effect of *KCNQ1* mutations. All experimental data are in the presence of the *KCNE1* β -subunit. Oocytes: *Xenopus* oocytes HEK: HEK-293 cells. -: not reported. Heart rate is resting heart rate in index patient (IP), mutation carriers (C) or non-affected family members (non-carriers, NC).

*The ratio between the current density of I_{Ks} in wild-type condition and with R231C mutation ($I_{KsR231C}/I_{KsWT}$) used to simulate the voltage dependent gain of function was estimated from Figure 4 (upper left corner) from Henrion *et al.* (2012).

3.3 Results

3.3.1 Model validation through the simulation of ion channel mutations

The implementation of the functional changes in ion channels as a result of genetic mutations allowed validation of the present model of the human SAN AP. A prerequisite of the validation process was that each of the mutations included in the analysis had been characterized clinically and that the effects of the mutation on the associated current had been investigated in vitro. Specifically, the criteria that a mutation had to satisfy were: (i) the availability of clinical data on adult patients affected by sinus node dysfunction related to the ion channel mutation of interest and (ii) the availability of an electrophysiological characterization of the mutation, usually carried out in heterologous cell systems (COS-7, CHO, tsA201 and HEK-293 cells or *Xenopus* oocytes), into which the mutation was transfected. Furthermore, to represent the clinical conditions as faithfully as possible, the electrophysiological data were ideally obtained from systems in which the expression of the mutation was heterozygous. However, in the absence of data on heterozygously expressed gain-of-function mutations in potassium voltage-gated channel subfamily Q member 1 (*KCNQ1*), data from homozygously expressed mutations were used.

We used the data from cellular electrophysiological studies to simulate the effects of mutations in the *HCN4*, *SCN5A* and *KCNQ1* genes, encoding the HCN4, Na_v1.5 and K_v7.1 pore-forming α -subunits of the I_f, I_{Na} and I_{Ks} channels, respectively, in our human SAN cell model. Next, we compared the results of our simulations with the clinical data. When clinical data relative to non-carrier family members were available, the model was tuned through autonomic modulation to reproduce the average heart rate reported for non-carriers as the control beating rate. Furthermore, if the clinical control rate was lower than the intrinsic beating rate of the model (74 beats min⁻¹), a not-null basal level of ACh was simulated, whereas a fixed percentage of the effects of isoprenaline on all its targets was simulated to obtain higher control rates. When clinical data relative to non-carriers

were not available, the effects of mutations were evaluated starting from the intrinsic beating rate of the model.

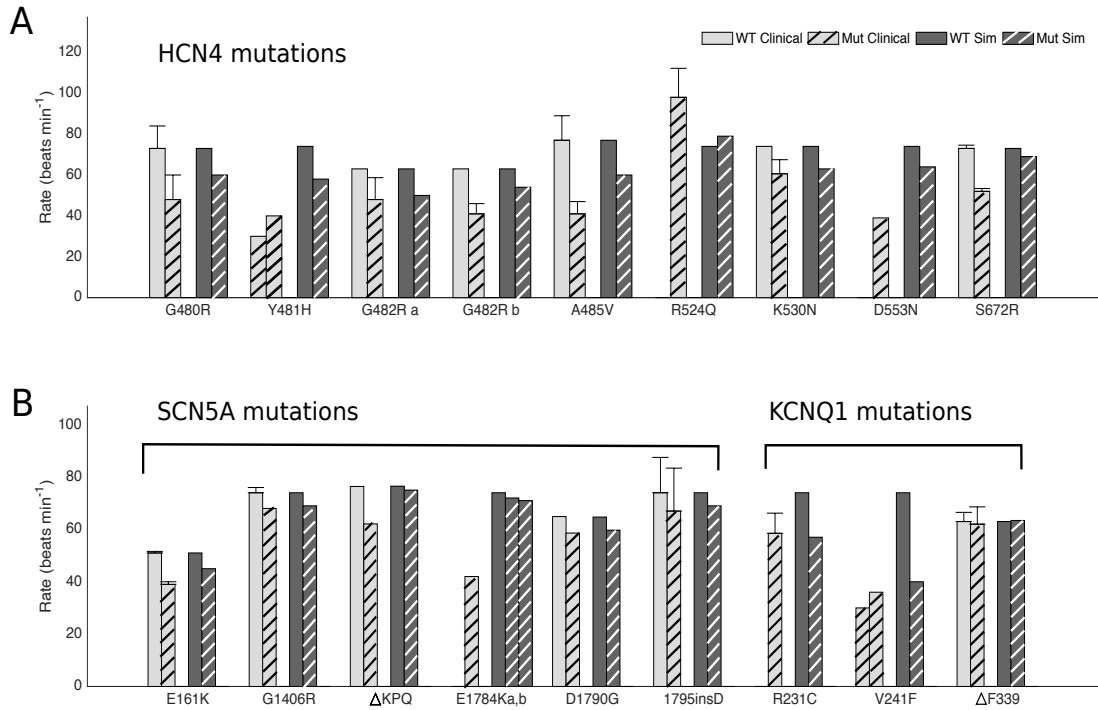


Figure 3.1: Clinically observed vs. simulated effects of I_f , I_{Na} and I_{Ks} mutations

(A) Comparison between clinical data (solid and hatched light grey bars) and simulation data (solid and hatched dark grey bars) on the effects of mutations affecting HCN4 channels (I_f). For the Y481H, R524Q and D553N mutations, no clinical data from non-carrier family members were available. SDs of the clinical data, where available, are indicated. (B) Comparison between clinical data (solid and hatched light grey bars) and simulation data (solid and hatched dark grey bars) on the effects of mutations affecting SCN5A channels (I_{Na} , group on the left) and KCNQ1 (I_{Ks} , group on the right). SDs of the clinical data, where available, are indicated. From the 'a' study on the E1784K mutation, no clinical data from non-carrier family members were available. Clinical data from the 'b' study were only reported in a qualitative way ('sinus node dysfunction') (Table 3.2). For the R231C and V241F mutations, no clinical data from non-carrier family members were available. SDs of the clinical data, where available, are indicated.

3.3.2 Effects of I_f mutations

All the initially observed mutations in *HCN4* resulted in a loss of function of I_f (Verkerk & Wilders, 2015), although, recently, a gain-of-function mutation in *HCN4* (R524Q) has also been reported by Baruscotti *et al.* (2017). A complete list of the mutations taken into consideration in the present study, together with a short description of their electrophysiological characterization and the parameter values used in our simulations, is reported in Table 3.1.

A loss-of-function-induced decrease in the intensity of I_f could be the result of (i) a hyperpolarizing shift of the steady-state activation curve y_∞ and time constant τ_y [e.g. for the Y481H and G482R (Milano *et al.*, 2014) and the K530N (Duhme *et al.*, 2013) mutations]; (ii) a reduction of the maximal conductance [e.g. for the G482R mutation (Schweizer *et al.*, 2014) and the D553N mutation (Ueda *et al.*, 2004)]; and (iii) both of the aforementioned changes together [e.g. for the G480R, A485V and S672R mutations (Verkerk & Wilders, 2015)]. Furthermore, there can be mutation-induced changes in the activation and/or deactivation rate of the I_f channel that contribute to the decrease of I_f intensity [e.g. the slowed activation in case of the G480R mutation (Nof *et al.*, 2007)].

In the simulations, all three types of loss-of-function mutations led to an increase in CL and thus a reduction of pacemaking rate (Fig. 3.1A). A more detailed look at the AP features reveals that DDR_{100} showed a substantial decrease for all loss-of-function mutations, varying from 8.5% for the relatively mild S672R mutation (pacemaking rate of 69 beats min^{-1}) to 40.7% for the A485V mutation (pacemaking rate of 61 beats min^{-1}), whereas APD_{90} was almost unchanged in our simulations. Similarly, changes in MDP and APA were almost negligible: the maximum hyperpolarization of the MDP amounted to 0.5 mV and the maximum increase in APA was 0.9 mV (both for the A485V mutation).

The only gain-of-function mutation, R524Q, led to an increase in I_f by shifting the steady-state activation curve and the time constant curve towards less negative potentials (Baruscotti *et al.*, 2017). Simulation of the mutation showed a faster pacemaking rate (79 beats min^{-1}). DDR_{100} had an increase of 8.2%, whereas MDP, APD_{90} and APA were unchanged.

The comparison between the pacemaking rates in our simulation data and the clinically observed heart rates (Fig. 3.1A) highlighted the ability of the model to reproduce the effects of the mutations on *HCN4* channels, at least qualitatively. Quantitatively, the effects in the simulation data are consistently smaller than those observed clinically, which might be expected (see Section 3.4 Discussion).

3.3.3 *HCN4* mutations and autonomic modulation

Fig. 3.2A shows the effects of autonomic modulation through ACh and Iso on the electrical activity of the human SAN pacemaker cell model. Under control conditions, the model cell shows pacemaker activity with a cycle length of 814 ms (Fig. 3.2A, top panel, grey trace). The associated time course of I_f is shown in the bottom panel of Fig. 3.2A. The amplitude of I_f is ≈ 1 pA, whereas the amplitude of the net inward current is ≈ 2 pA (not shown). Thus, I_f is an important inward current during the diastolic depolarization phase.

The inhibition of I_f by ACh contributes to the increase in cycle length to 1231 ms (Fig. 3.2A, blue traces). The application of Iso stimulates I_f and decreases cycle length to 429 ms (Fig. 3.2A, red traces). A loss-of-function mutation in *HCN4* will lead to a smaller I_f , and thus a decrease in inward current during diastolic depolarization, at all levels of autonomic tone.

Fig. 3.2, B–D, shows the effects of mutations in *HCN4* on the pacemaker activity of the model cell at different levels of autonomic tone. The G480R mutation (Fig. 3.2B) reduces I_f by $\approx 50\%$. As a result, the cycle length increases from 814 to 961 ms (+18%) under control conditions. With ACh and Iso, the cycle length increases from 1231 to 1503 ms (+22%) and from 429 to 519 ms (+21%), respectively.

With a -30 mV shift in voltage dependence and a scaling factor of 0.33, the A485V mutation is more ‘severe’ than the G480R mutation, which shows a -15 mV shift and a scaling factor of 0.5. This is reflected in a smaller amplitude of I_f and slower pacemaking (Fig. 3.2C). The cycle length now amounts to 1018 ms

under control conditions (+25%) and to 1618 ms (+31%) and 599 ms (+40%) with ACh and Iso, respectively.

The functional effects are somewhat different for the 695X mutation, which leads to a loss of cAMP sensitivity of I_f rather than to a shift in its voltage dependence and/or a reduction in its fully-activated conductance. With an increase in cycle length to 1326 ms (+8%), the effects of the 695X mutation are relatively mild at vagal tone (Fig. 3.2D). Under control conditions and with Iso, cycle length increases to 924 ms (+14%) and to 550 ms (+28%), respectively.

The functional effects of the three different mutations are summarized in Fig. 3.3, which shows the beating rate of the model cell at different levels of autonomic tone for each of the mutations. The grey bars show the beating rate in the absence of a mutation.

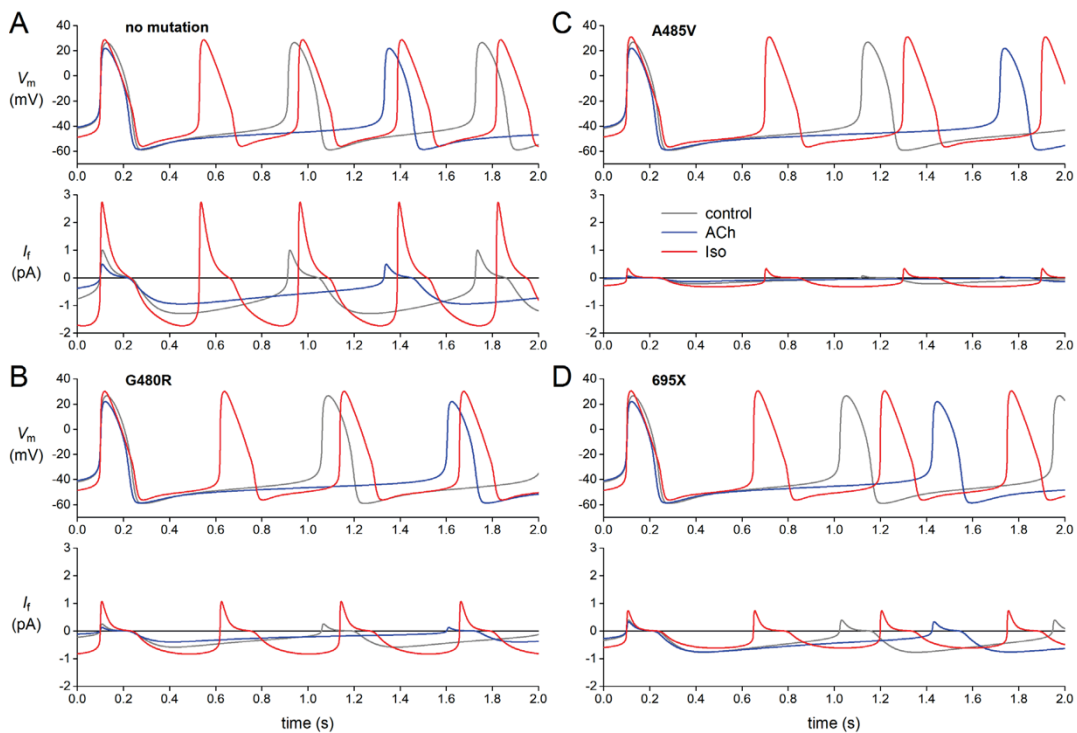


Figure 3.2. HCN4 mutations and electrical activity at different levels of autonomic tone

Effects of mutations in HCN4 on the pacemaker activity of our human SAN cell model at different levels of autonomic tone. Membrane potential (V_m) and associated hyperpolarization-activated 'funny current' (I_f). (A) Default model (no mutation). (B) G480R, (C) A485V, and (D) 695X mutations

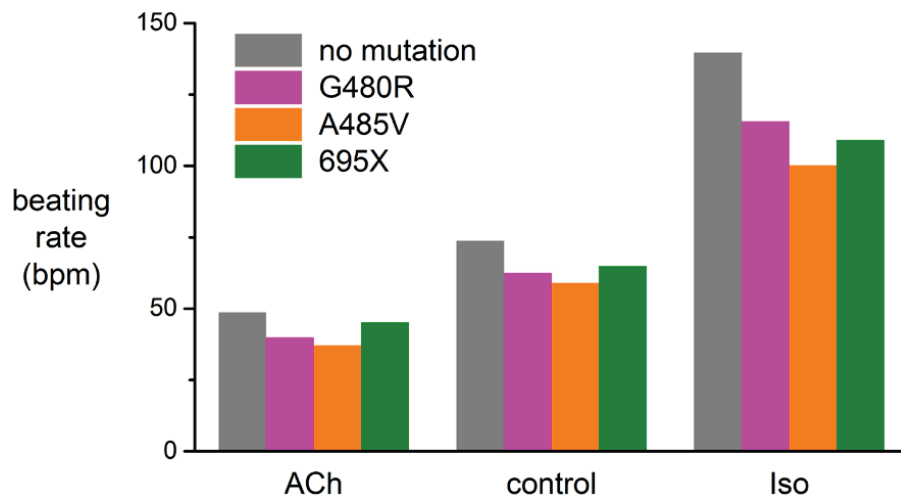


Figure 3.3. HCN4 mutations and autonomic modulation

Effects of the G480R, A485V, and 695X mutations in HCN4 on the beating rate of our human SAN cell model at different levels of autonomic tone. Vagal tone (ACh, left), control (middle), and β -adrenergic tone (Iso, right).

3.3.4 Effects of I_{Na} mutations

A large number of mutations identified in *SCN5A* are related to sinus dysfunction, such as sinus bradycardia and sinus pauses (often associated with the LQT3 phenotype) and sick sinus syndrome (Veldkamp *et al.*, 2003; Lei *et al.*, 2007).

A loss of function of the I_{Na} channel can have several causes: (i) a rapid inactivation of the ion channel; (ii) a depolarizing shift of activation; (iii) a hyperpolarizing shift of inactivation; and (iv) a reduction of the current density, which, in some cases, can lead to the non-function phenotype (i.e. a full loss of function). In several cases, multiple causes can be present at the same time, enhancing the reduction of I_{Na} (Table 3.2).

The simulations of the effects of loss-of-function I_{Na} mutations showed a decrease in pacemaking rate, up to 11.8% for the E161K mutation. DDR_{100} showed a decrease for all mutations (with a maximum of 9.0% for E161K). APD_{90} , MDP and APA were almost unchanged for all mutations.

In simulations of Δ KPQ (Nagatomo *et al.*, 1998) and E1784K [parameters from Deschênes *et al.* (2000) and Makita *et al.* (2008)] and 1795insD mutations [parameters from Bezzina *et al.* (1999) and Veldkamp *et al.* (2000)] an incomplete inactivation, which induced a sustained (late) Na^+ current (gain of function), was combined with a loss of function. The DDR_{100} resulting from this combined gain and loss of function showed a decrease (-5.8% for Δ KPQ, -7.9% and -7.7% for E1784K, and -8.0% for 1795insD). By contrast, APD_{90} showed an increase for all three mutations ($+1.3\%$ for Δ KPQ, $+2.2\%$ and $+1.5\%$ for E1784K ‘a’ and ‘b’, and $+0.6\%$ for 1795insD). The overall effect was a reduction of the pacemaking rate for all simulated mutations (by -4.8% for Δ KPQ, -2.9% and -3.7% for E1784K ‘a’ and ‘b’, and -6.2% for 1795insD).

To assess the contribution of an incomplete inactivation of I_{Na} channels in these ‘mixed mutations’, we investigated the effect of I_{NaL} alone by introducing this current into a cell in control condition. The presence of I_{NaL} caused two opposing effects: enhanced inward current during late DD resulted in a steeper DDR, whereas inward I_{Na} current during AP prolonged APD. In our model for g_{NaL} set to 1% of g_{Na} in the control condition, the higher inward current during late DD prevailed. The overall effect of I_{NaL} was a minor increase of the pacemaking rate ($+3.2\%$). However, in the four mixed loss- and gain-of-function mutations analyzed, the loss-of-function effect prevailed and led to an overall slowdown of the pacemaking rate.

A comparison of pacemaking rates predicted by the model and clinical data is shown in Fig. 3.1B. The simulation data for the G1406R, D1790G and 1795insD mutations were in close agreement, both qualitatively and quantitatively, with the clinical data. For the other three mutations, the simulations showed a decrease of the beating rate compatible with the loss-of-function behavior of the mutations, although it was quantitatively less close to the clinically observed effect.

3.3.5 Effects of I_{Ks} mutations

Both loss-of-function and gain-of-function mutations in *KCNQ1*, encoding the $K_{V7.1}$ pore-forming α -subunit of the I_{Ks} channel, have been reported in relation to sinus bradycardia.

A gain of function of $K_{V7.1}$ channels could be the result of (i) a higher current density, as observed for the R231C mutation (Henrion *et al.*, 2012) or (ii) a hyperpolarizing shift of the steady-state activation curve, as observed for the V241F mutation (Ki *et al.*, 2013). With either simulated mutation, DDR_{100} was markedly increased. However, the overall DDR was reduced, leading to a longer DD phase duration. Both mutations showed a slight depolarization of MDP (from -58.9 to -57.6 and -57.1 mV for R231C and V241F, respectively), whereas APD_{90} was considerably reduced (by 10.8% and 19.8% for R231C and V241F, respectively). Thus, opposing effects were present. However, the prolongation of the DD phase far outweighed the effects of a higher DDR_{100} and a shorter APD_{90} , leading to slower pacemaking rates (57 and 40 beats min^{-1} for R231C and V241F, respectively), which were in good agreement with clinical data (Fig. 3.1B). On the other hand, a loss of function of $K_{V7.1}$ channels can be attributed to (i) a lower channel expression or (ii) a depolarizing shift of the steady-state activation curve.

The $\Delta F339$ mutation shows both effects (Table 3.3) (Thomas *et al.*, 2005). The model predicted a negligible change in pacemaking rate (from 63 to 63.5 beats min^{-1}), which is consistent with clinical data (Fig. 3.1B); DDR_{100} was slightly reduced (by 2.4%) and APD_{90} was increased (by 1.3%), whereas MDP was almost unchanged.

3.4 Discussion

3.4.1 *HCN4* mutations

Because of the clinical importance of this research, a large number of studies have previously been carried out and a considerable amount of both clinical and electrophysiological data is available, as reviewed by Verkerk & Wilders (2014, 2015). *HCN4* is the most abundant isoform of the HCN family. Most *HCN4* mutations result in a loss of function of I_f , although, recently, Baruscotti *et al.* (2017) found a mutation that results in a gain of function. In our simulations, I_f exerted its contribution during DD, influencing the amount of net inward current, and thus the slope of this phase. In this way, a loss of function of I_f leads to a slower rate, whereas a gain of function leads to a faster one. A remarkable aspect of this finding is that I_f is able to modulate DDR at the same time as leaving other important parameters (such as APD and MDP) unchanged.

The simulations of loss-of-function mutations in *HCN4* show a considerable slowing but not a complete cessation of pacemaker activity. The slowing is consistently smaller than that observed in the associated mutation carriers (Fig. 3.1). The difference between clinical and simulated effects of mutations, however, is to be expected because the hyperpolarizing effect of the surrounding atrium will result in a more prominent role of I_f in the SA node of the intact heart. Of note, our current model appears to be more promising for assessing the effects of *HCN4* mutations in humans than the comprehensive rabbit SAN cell models described by Maltsev and Lakatta (2009) and Severi *et al.* (2012). As recently reported by Wilders & Verkerk (2016), the mutation effects appear to be highly underestimated in the Maltsev–Lakatta model, in which a slowing of only 5.2% was observed for the most severe of the 11 mutations tested (A485V; 21.4% in the present model) and highly overestimated in the Severi–DiFrancesco model, where pacemaker activity ceased for five of the 11 mutations, including A485V.

3.4.2 *SCN5A* mutations

In the validation stage, a large number of mutations in the *SCN5A*-encoded $\text{Na}_v1.5$ channels were assessed. We observed two kinds of mutations: the first kind was characterized by changes in electrophysiological properties that led to a loss of function of channels (E161K, G1406R and D1790G); the second kind showed the concurrent presence of loss of function and gain of function (Δ KPQ, E1784K and 1795insD). The latter effect was the result of an incomplete inactivation of I_{Na} channels, which was incorporated into the model by means of the $I_{\text{Na,L}}$ current.

Loss-of-function mutations reduced the inward current carried by I_{Na} and therefore decreased DDR. Thus, I_{Na} regulated heart rate in an analogous way to that of the funny current; however, the lower weight of I_{Na} in the overall inward current resulted in quantitatively fewer extensive effects with respect to I_f .

Similar to the mutations in *HCN4*, the slowing in pacemaking rate associated with mutations in *SCN5A* is consistently smaller in simulations than in the intact heart (Fig. 3.1). Again, this could be explained by the hyperpolarizing effect of the surrounding atrium that could also result in a more prominent role of I_{Na} in the SA node of the intact heart. In our current model, we observed a decrease in the pacemaking rate of up to 14.9% for the most severe *SCN5A* mutation. We could not test the *SCN5A* mutation effects in the Maltsev–Lakatta rabbit SAN cell model because this model lacks I_{Na} . In the Severi–DiFrancesco rabbit SAN cell model, the decrease in pacemaking rate was almost negligible for each of the *SCN5A* mutations tested, with a maximum near 1%.

3.4.3 *KCNQ1* mutations

The simulated effect of the $\Delta F339$ loss-of-function mutation in *KCNQ1* that affects $K_{V7.1}$ channels is almost negligible. The gain of function of I_{Ks} was more critical. The increase in outward current resulted in a DDR reduction that far outweighed the accompanying APD reduction. Thus, the gain-of-function mutations R231C and V241F resulted in a rate slowdown compatible with the clinically observed sinus bradycardia. However, it should be noted that the electrophysiological characterizations of both R231C and V241F were obtained in homozygous expression (Table 3.3). Although no experimental data are available concerning the R231C and V241F mutations in heterozygous expression, we decided to include these simulations anyway to provide a lower limit of the beating rate that the model can achieve for these mutations.

3.4.4 General remarks

The comparison between clinical findings and simulated effects of mutations on beating rate showed good overall behavior of the model. Except for the I_{Ks} $\Delta F339$ mutation, simulated effects on beating rate were in accordance with the reported clinical data (Fig. 3.1). It should be noted that there is always a gap between clinical and simulated mutation effects, given the difference in the systems analyzed: the heart rate is a macroscopic phenomenon, resulting from the overall SAN tissue behavior and its interaction with the autonomic nervous system, whereas the beating rate predicted by the model considers only the microscopic single cell level. At this level, there is (for example) no hyperpolarizing effect of the surrounding atrium, which may increase I_f and I_{Na} and thus the functional effects of mutations in the associated genes. It should also be noted that carriers of the same mutation may show widely different phenotypes, even within the same family. This holds in particular for the *SCN5A* mutations; it is possible that only a minority of the affected family members show

sinus node dysfunction. Finally, other factors, such as physical training level, can affect the difference in basal heart rate found between healthy subjects and mutation carriers.

As emphasized by Verkerk & Wilders (2015) for *HCN4* mutations, although it can be readily extended to other ion channels, there are inconsistencies between clinical and experimental data. Many factors can underlie these inconsistencies: (i) data on current density can be misleading because heterologous systems (in vitro) can express different levels of the gene affected by the mutation with respect to the subject (in vivo) under investigation; (ii) experimental data can be incomplete and may strongly depend on the expression system and the experimental protocol employed; (iii) clinical data are often limited to a small number of patients, or even a single patient; (iv) the affected isoform is not the only one expressed in vivo; and (v) remodeling processes can occur in mutant carriers and affect their clinical phenotypes.

References

- Baruscotti M, Bucchi A, Milanese R, Paina M, Barbuti A, Gneccchi-Ruscione T, Bianco E, Vitali-Serdoz L, Cappato R & DiFrancesco D (2017). A gain-of-function mutation in the cardiac pacemaker HCN4 channel increasing cAMP sensitivity is associated with familial Inappropriate Sinus Tachycardia. *Eur Heart J* 38, 280–288.
- Benhorin J, Taub R, Goldmit M, Kerem B, Kass RS, Windman I & Medina A (2000). Effects of flecainide in patients with new SCN5A mutation mutation-specific therapy for long-QT syndrome? *Circulation* 101, 1698–1706.
- Benson DW, Wang DW, Dymont M, Knilans TK, Fish FA, Strieper MJ, Rhodes TH & George AL (2003). Congenital sick sinus syndrome caused by recessive mutations in the cardiac sodium channel gene (SCN5A). *J Clin Invest* 112, 1019–1028.
- Bezzina C, Veldkamp MW, Berg MPV den, Postma AV, Rook MB, Viersma J-W, Langen IMV, Tan-Sindhunata G, Bink-Boelkens MTE, Hout AH van der, Mannens MMAM & Wilde AAM (1999). A single Na⁺ channel

- mutation causing both long-QT and brugada syndromes. *Circ Res* 85, 1206–1213.
- Deschênes I, Baroudi G, Berthet M, Barde I, Chalvidan T, Denjoy I, Guicheney P & Chahine M (2000). Electrophysiological characterization of SCN5A mutations causing long QT (E1784K) and Brugada (R1512W and R1432G) syndromes. *Cardiovasc Res* 46, 55–65.
- Duhme N, Schweizer PA, Thomas D, Becker R, Schröter J, Barends TRM, Schlichting I, Draguhn A, Bruehl C, Katus HA & Koenen M (2013). Altered HCN4 channel C-linker interaction is associated with familial tachycardia–bradycardia syndrome and atrial fibrillation. *Eur Heart J* 34, 2768–2775.
- Henrion U, Zumhagen S, Steinke K, Strutz-Seebohm N, Stallmeyer B, Lang F, Schulze-Bahr E & Seebohm G (2012). Overlapping cardiac phenotype associated with a familial mutation in the voltage sensor of the KCNQ1 channel. *Cell Physiol Biochem* 29, 809–818.
- Bigger JT Jr & Reiffel JA (1979). Sick Sinus Syndrome. *Annu Rev Med* 30, 91–118.
- Ki C-S, Jung CL, Kim H, Baek K-H, Park SJ, On YK, Kim K-S, Noh SJ, Youm JB, Kim JS & Cho H (2013). A KCNQ1 mutation causes age-dependant bradycardia and persistent atrial fibrillation. *Pflügers Arch - Eur J Physiol* 466, 529–540.
- Kyndt F, Probst V, Potet F, Demolombe S, Chevallier J-C, Baro I, Moisan J-P, Boisseau P, Schott J-J, Escande D & Marec HL (2001). Novel SCN5A mutation leading either to isolated cardiac conduction defect or Brugada syndrome in a large French family. *Circulation* 104, 3081–3086.
- Laish-Farkash A, Glikson M, Brass D, Marek-Yagel D, Pras E, Dascal N, Antzelevitch C, Nof E, Reznik H, Eldar M & Luria D (2010). A novel mutation in the HCN4 gene causes symptomatic sinus bradycardia in Moroccan Jews. *J Cardiovasc Electrophysiol* 21, 1365–1372.
- Lamas GA, Lee KL, Sweeney MO, Silverman R, Leon A, Yee R, Marinchak RA, Flaker G, Schron E, Orav EJ, Hellkamp AS, Greer S, McAnulty J, Ellenbogen K, Ehlert F, Freedman RA, Estes NAMI, Greenspon A & Goldman L (2002). Ventricular pacing or dual-chamber pacing for sinus-node dysfunction. *N Engl J Med* 346, 1854–1862.
- Lei M, Zhang H, Grace AA & Huang CL-H (2007). SCN5A and sinoatrial node pacemaker function. *Cardiovasc Res* 74, 356–365.
- Makita N, Behr E, Shimizu W, Horie M, Sunami A, Crotti L, Schulze-Bahr E, Fukuhara S, Mochizuki N, Makiyama T, Itoh H, Christiansen M, McKeown

- P, Miyamoto K, Kamakura S, Tsutsui H, Schwartz PJ, George AL & Roden DM (2008). The E1784K mutation in SCN5A is associated with mixed clinical phenotype of type 3 long QT syndrome. *J Clin Invest*; DOI: 10.1172/JCI34057.
- Maltsev VA & Lakatta EG (2009). Synergism of coupled subsarcolemmal Ca²⁺ clocks and sarcolemmal voltage clocks confers robust and flexible pacemaker function in a novel pacemaker cell model. *Am J Physiol - Heart Circ Physiol* 296, H594–H615.
- Milanesi R, Baruscotti M, Gnecci-Ruscone T & DiFrancesco D (2006). Familial sinus bradycardia associated with a mutation in the cardiac pacemaker channel. *N Engl J Med* 354, 151–157.
- Milano A, Vermeer AMC, Lodder EM, Barc J, Verkerk AO, Postma AV, Van der Bilt IAC, Baars MJH, Van Haelst PL, Caliskan K, Hoedemaekers YM, Le Scouarnec S, Redon R, Pinto YM, Christiaans I, Wilde AA & Bezzina CR (2014). HCN4 mutations in multiple families with bradycardia and left ventricular noncompaction cardiomyopathy. *J Am Coll Cardiol* 64, 745–756.
- Moss AJ, Zareba W, Benhorin J, Locati EH, Hall WJ, Robinson JL, Schwartz PJ, Towbin JA, Vincent GM, Lehmann MH, Keating MT, MacCluer JW & Timothy KW (1995). ECG T-wave patterns in genetically distinct forms of the hereditary long QT syndrome. *Circulation* 92, 2929–2934.
- Nagatomo T, Fan Z, Ye B, Tonkovich GS, January CT, Kyle JW & Makielski JC (1998). Temperature dependence of early and late currents in human cardiac wild-type and long Q-T Δ KPQ Na⁺ channels. *Am J Physiol - Heart Circ Physiol* 275, H2016–H2024.
- Nof E, Luria D, Brass D, Marek D, Lahat H, Reznik-Wolf H, Pras E, Dascal N, Eldar M & Glikson M (2007). Point mutation in the HCN4 cardiac ion channel pore affecting synthesis, trafficking, and functional expression is associated with familial asymptomatic sinus bradycardia. *Circulation* 116, 463–470.
- Schulze-Bahr E, Neu A, Friederich P, Kaupp UB, Breithardt G, Pongs O & Isbrandt D (2003). Pacemaker channel dysfunction in a patient with sinus node disease. *J Clin Invest* 111, 1537–1545.
- Schweizer PA, Schröter J, Greiner S, Haas J, Yampolsky P, Mereles D, Buss SJ, Seyler C, Bruehl C, Draguhn A, Koenen M, Meder B, Katus HA & Thomas D (2014). The symptom complex of familial sinus node dysfunction and myocardial noncompaction is associated with mutations in the HCN4 channel. *J Am Coll Cardiol* 64, 757–767.

- Severi S, Fantini M, Charawi LA & DiFrancesco D (2012). An updated computational model of rabbit sinoatrial action potential to investigate the mechanisms of heart rate modulation. *J Physiol* 590, 4483–4499.
- Smits JPP, Koopmann TT, Wilders R, Veldkamp MW, Opthof T, Bhuiyan ZA, Mannens MMAM, Balsler JR, Tan HL, Bezzina CR & Wilde AAM (2005). A mutation in the human cardiac sodium channel (E161K) contributes to sick sinus syndrome, conduction disease and Brugada syndrome in two families. *J Mol Cell Cardiol* 38, 969–981.
- Thomas D, Wimmer A-B, Karle CA, Licka M, Alter M, Khalil M, Ulmer HE, Kathöfer S, Kiehn J, Katus HA, Schoels W, Koenen M & Zehelein J (2005). Dominant-negative I_{Ks} suppression by KCNQ1- $\Delta F339$ potassium channels linked to Romano–Ward syndrome. *Cardiovasc Res* 67, 487–497.
- Ueda K, Nakamura K, Hayashi T, Inagaki N, Takahashi M, Arimura T, Morita H, Higashiuesato Y, Hirano Y, Yasunami M, Takishita S, Yamashina A, Ohe T, Sunamori M, Hiraoka M & Kimura A (2004). Functional characterization of a trafficking-defective HCN4 mutation, D553N, associated with cardiac arrhythmia. *J Biol Chem* 279, 27194–27198.
- Veldkamp MW, Viswanathan PC, Bezzina C, Baartscheer A, Wilde AAM & Balsler JR (2000). Two distinct congenital arrhythmias evoked by a multidysfunctional Na^+ channel. *Circ Res* 86, e91–e97.
- Veldkamp MW, Wilders R, Baartscheer A, Zegers JG, Bezzina CR & Wilde AAM (2003). Contribution of sodium channel mutations to bradycardia and sinus node dysfunction in LQT3 families. *Circ Res* 92, 976–983.
- Verkerk AO & Wilders R (2014). Pacemaker activity of the human sinoatrial node: effects of HCN4 mutations on the hyperpolarization-activated current. *Europace* 16, 384–395.
- Verkerk AO & Wilders R (2015). Pacemaker activity of the human sinoatrial node: an update on the effects of mutations in HCN4 on the hyperpolarization-activated current. *Int J Mol Sci* 16, 3071–3094.
- Wehrens XHT, Abriel H, Cabo C, Benhorin J & Kass RS (2000). Arrhythmogenic mechanism of an LQT-3 mutation of the human heart Na^+ channel α -subunit a computational analysis. *Circulation* 102, 584–590.
- Wilders R & Verkerk AO (2016). In quest of a sinoatrial cell model to assess the functional effects of mutations in the HCN4 funny current gene. *Comput Cardiol* 43, 833–836.

Chapter 4

Effects of the small and large conductance calcium-activated potassium currents (I_{SK} and I_{BK}) in human sinoatrial node

Part of the content of this chapter is in

“Effects of the small conductance calcium-activated potassium current (I_{SK}) in human sinoatrial node”

Computing in Cardiology 2017, In press

Alan Fabbri¹, Michelangelo Paci², Jari Hyttinen², Ronald Wilders³ and Stefano Severi¹

¹ Computational Physiopatology Unit, Department of Electrical, Electronic and Information Engineering “Guglielmo Marconi”, University of Bologna, Cesena, Italy

² Computational Biophysics and Imaging Group (CBIG), Faculty of Biomedical Sciences and Engineering, Tampere University of Technology BioMediTech, Tampere, Finland

³ Department of Anatomy, Embriology and Physiology, Academic Medical Center, University of Amsterdam, Amsterdam, The Netherlands

Abstract

Small (SK) and large (BK) conductance channels are potassium channels sensitive to changes in intracellular calcium. Calcium-activated potassium channels (K_{Ca}) are largely diffused in brain, smooth muscle and cardiac tissue and are involved in neuro-secretion, smooth muscle tone and action potential shape. Several studies reported that SK and BK channels are able to modulate heart rate; however the underlying mechanisms are not fully understood.

Aim of this work is to evaluate the effects on action potential features of the inclusion of I_{SK} and I_{BK} into the human and rabbit sinoatrial node (SAN) computational models.

I_{SK} was formulated accordingly to Kennedy *et al.* (2017) and different values for the maximal conductance g_{SK} were tested: 4, 10 and 41.7 $\mu\text{S}/\mu\text{F}$. I_{BK} was formulated in accordance with Orio *et al.* (2006) and g_{BK} was set to 5, 9.3, 25 and 50 $\mu\text{S}/\mu\text{F}$.

The inclusion of I_{SK} increased the beating rate from 74 up to 137 beat min^{-1} (+85.1%) and from 169 up to 212 beat min^{-1} (+25.4%), for $g_{SK} = 41.7 \mu\text{S}/\mu\text{F}$ for human and rabbit SAN, respectively. The maximal activity of I_{BK} ($g_{BK} = 50 \mu\text{S}/\mu\text{F}$) was responsible for a beating rate increase from 74 up to 76 beat min^{-1} (+2.7%) in human SAN and from 169 up to 174 beat min^{-1} (+3.0%) in rabbit SAN.

The effects of I_{SK} and I_{BK} are in agreement with the behavior reported in literature, even if less extended, especially for I_{BK} . The increase in the pacing rate was mainly due to shortening of the diastolic depolarization phase. Interestingly, such changes on the diastolic depolarization phase are an indirect effect of K_{Ca} currents: K_{Ca} are mainly activated by the calcium transient and cause a decrease in the AP amplitude, which in turn is responsible for a lower activation of the outward I_{Kr} during the spontaneous depolarization.

4.1 Introduction

Calcium-activated potassium channels (K_{Ca}) are largely expressed in both excitable and non-excitable cells and carry out many functions such as neurosecretion, smooth muscle tone and action potential shape.

The main characteristic of K_{Ca} channels consists in their ability to couple intracellular Ca^{2+} fluctuations to membrane voltage changes; on the basis of their single channel conductance they are classified in 3 subfamilies: small (SK), intermediate (IK) and large (BK) conductance channels. Electrophysiological studies reported conductances of ≈ 10 pS for SK (Lancaster *et al.*, 1991; Köhler *et al.*, 1996), 20-80 pS for IK (R Latorre *et al.*, 1989) and 100-300 pS for BK (Toro *et al.*, 1998).

At least 3 distinct genes, KCNN1 (SK1), KCNN2 (SK2) and KCNN3 (SK3) encode for SK channels; the pore-forming α subunit is composed by 6 transmembrane domains and it is gated solely by sub-micromolar concentrations of intracellular Ca^{2+} (Köhler *et al.*, 1996); the ensemble of four tetramers forms the functional ion channel.

The presence of SK channels in cardiac tissue was detected through RT-PCR, western blot analysis and immunofluorescence labeling in murine (Tuteja *et al.*, 2005; Torrente *et al.*, 2017), guinea pig (Koumi *et al.*, 1994), rabbit (Giles & Imaizumi, 1988; Chen *et al.*, 2013) and humans (Xu *et al.*, 2003; Chandler *et al.*, 2009).

Apamin is a neurotoxin in bee venom that showed remarkably specificity for SK channels; SK2 are the most sensitive isoforms to apamin ($EC_{50} \approx 40$ pM), SK3 showed intermediate sensitivity ($EC_{50} \approx 1$ nM) and SK1 are the least sensitive ($EC_{50} \approx 10$ nM).

Several studies have shown that SK channels are involved in heart rate modulation, affecting the automaticity of the cardiac tissue. Observing isolated atrioventricular node tissue in a mouse model, (Zhang *et al.*, 2008) reported a decreased automatic activity in knock out (KO) SK2 channels specimens, whereas the overexpression of SK2 led to a faster beating rate. Notably, significant

changes with respect to wild type (WT) were found in the diastolic depolarization rate and in AP duration. Chen *et al.* (2013) characterized I_{SK} current in rabbit SAN cells with the administration of 1 and 10 nM of apamin, showing a decrease of beating rate due to APD prolongation. Torrente *et al.* (2017) measured I_{SK} in murine SAN tissue and reported a slowed repolarization, depolarized MDP and prolonged diastolic depolarization upon 10 nM apamin administration.

The pore-forming α and the regulatory β subunits of BK channels are encoded by KCNMA and KCNMB gene respectively. BK channels are both voltage and Ca^{2+} -dependent, with a voltage sensitive region and a dedicated “calcium bowl” that bind Ca^{2+} located in the α subunit. The β subunit is not necessary for ion conduction but is able to affect calcium sensitivity and kinetics time constant (Schreiber & Salkoff, 1997).

BK channels are present in many tissues as brain, smooth muscle and cardiac tissue. They are involved in the control of the neuronal circuits in hippocampus, control of blood pressure and regulation of heart rate. Imlach *et al.* (2010) investigated the role of BK channels in heart rate control through the effects of paxilline (PAX) and lolitrem B, two BK blockers, on a BK KO mouse model *in vivo* and in isolated hearts, highlighting that an inhibition of BK current was responsible for the slowdown of the beating rate. Lai *et al.* (2014) characterized native I_{BK} in SAN cells and cloned I_{BK} in HEK, reporting a pronounced prolongation of diastolic depolarization upon PAX administration.

Since their capability to modulate heart rate and the specificity of their inhibitors, SK and BK channels can be important pharmacological targets to treat arrhythmias.

The electrophysiological characterization of I_{SK} and I_{BK} showed that they are two outward potassium currents active especially during the AP; however, experimental studies highlighted that the diastolic depolarization (DD) is affected by I_{SK} and I_{BK} and the mechanisms of how those two potassium currents modulates DD are still unclear.

Aim of this work is to evaluate the effects brought by the inclusion of I_{SK} and I_{BK} on the features of the human SAN computational model and to provide insights on how they can modulate the spontaneous DD.

To this end, we added mathematical formulations based on the available experimental data and we performed a preliminary sensitivity analysis using maximal conductance values within the range reported in literature.

4.2 Methods

4.2.1 Mathematical description of I_{SK}

The mathematical formulation of I_{SK} was adopted from Kennedy *et al.* (2017), who recently developed mathematical model of I_{SK} in order to analyse its impact on a ventricular myocyte model:

$$I_{SK} = g_{SK}x_{SK}(V_m - E_K) \quad (4.1)$$

where g_{SK} is the maximal conductance, x_{SK} is the time and calcium-dependent gating variable, V_m is the membrane potential and E_K is the potassium reversal potential.

The first order x_{SK} kinetics –both the steady state activation curve $x_{SK,\infty}$ and the time constant τ_{SK} – are dependent on the calcium concentration sensed in the sub-sarcolemma space ($[Ca^{2+}]_{sub}$) rather than on the membrane potential.

The calcium dependence of $x_{SK,\infty}$ is described by a Hill equation,

$$x_{SK,inf} = 0.81 \cdot \frac{[Ca^{2+}]_{sub}^n}{[Ca^{2+}]_{sub}^n + EC_{50}^n}, \quad (4.2)$$

while τ_{SK} has a hyperbolic dependence on calcium,

$$\tau_{SK} = \frac{1}{0.047 \cdot [Ca^{2+}]_{sub} + 1/76}, \quad (4.3)$$

both the formulations were adopted from Hirschberg *et al.* (1998).

In this work, the half maximal effective calcium concentration $EC_{50} = 0.7 \mu M$ adopted by (Kennedy *et al.*, 2017) and aHill coefficient $n=2.2$ according to

(Hirschberg *et al.*, 1998) were assumed. τ_{SK} and $[Ca^{2+}]_{sub}$ are expressed in ms and μM , respectively.

In literature, the maximal conductance g_{SK} has been estimated in several ways and quite a large range of values was found; studies carried out on ventricular myocytes pointed out g_{SK} close to $10 \mu S/\mu F$. The computational study on ventricular myocytes by (Kennedy *et al.*, 2017) estimated $g_{SK}=0.8 \mu S/\mu F$ based on the apamin effects on APD and employed a range from 0.4 to $4 \mu S/\mu F$. (Torrente *et al.*, 2017) characterized I_{SK} current in mouse SAN cells and the impact of I_{SK} block on pacemaking. A voltage clamp protocol stepping from a holding potential of -55 mV to test potentials ranging from -100 to $+50$ mV was used and I_{SK} was obtained as the difference in net membrane current before and after the administration of apamin at a concentration of 10 nM. The intracellular calcium was buffered to $0.5 \mu M$ with EGTA into the pipette solution. We estimated the maximal conductance g_{SK} from their I-V relationship (see Figure 4.1) with a linear fitting procedure, obtaining the extremely high value of $41.7 \mu S/\mu F$.

The sensitivity of the human and rabbit SAN AP models to the inclusion of I_{SK} was explored testing different values of g_{SK} : 4 , 10 and $41.7 \mu S/\mu F$.

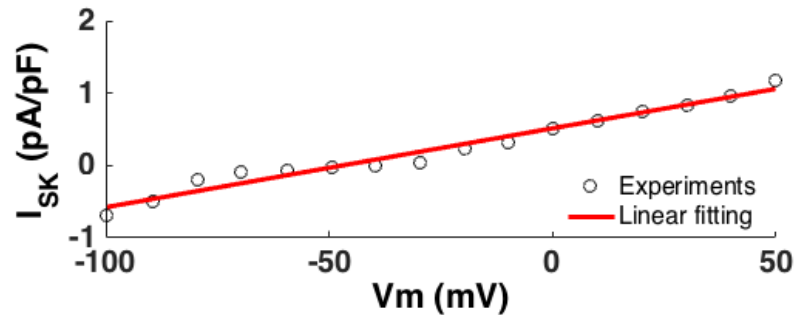


Figure 4.1. Linear fitting of the I-V relationship reported by Torrente *et al.* (2017) with intracellular calcium buffered to $0.5 \mu M$. The estimated $g_{SK,max}$ was $41.7 \mu S/\mu F$.

4.2.2 Mathematical description of I_{BK}

The mathematical formulation of I_{BK} was adopted from Orio & Latorre, (2005), who characterized the BK channels with the patch clamp technique expressing the KCNMA1 gene (for the α subunit) and KCNMB1, KCNMB2 (for the $\beta 1$ and $\beta 2$ subunit) in *Xenopus laevis* :

$$I_{BK} = g_{BK,max}x_{BK}(V_m - E_K) \quad (4.4)$$

where $g_{BK,max}$ is the maximal conductance, x_{BK} is the gating variable, V_m is the membrane potential and E_K is the reversal potential of potassium.

The steady state activation curve is both voltage and calcium-dependent:

$$x_{BK,\infty} = \frac{1}{1 + e^{\frac{zF(V - V_{0.5})}{RT}}} \quad (4.5)$$

where z is the valence, F is the Faraday constant, $V_{0.5}$ is the half maximal activation voltage, R is the universal gas constant and T is absolute temperature (K).

The dependence on the intracellular calcium is expressed by z and $V_{0.5}$. We fitted data published by (Orio & Latorre, 2005), relative to the α subunit [see Figure 10, panel C and D (Orio & Latorre, 2005)] as follows:

$$V_{0.5}(Ca_{sub}) = \frac{268.26}{1 + e^{\frac{(\log_{10}Ca_{sub} + 0.1173)}{0.6127}}} - 35.8 \quad (4.6)$$

$$z(Ca_{sub}) = 0.8556 - 0.6373 \frac{1}{1 + e^{\frac{-(\log_{10}Ca_{sub} - 1.76975)}{2.7337}}} \left(1 - \frac{1}{1 + e^{\frac{-(\log_{10}Ca_{sub} - 2.19845)}{2.7337}}} \right) \quad (4.7)$$

where Ca_{sub} is scaled by \log_{10} .

Figure 4.2, that reconstructs Figure 10 (Panels A, C and D) in Orio & Latorre, (2005), reports $x_{BK,\infty}$ (panel A) for several intracellular calcium concentrations (5, 30, 100, 200, 680 nM, 1.8, 2.8, 12 and 150 μM), and fitted $V_{0.5}$ and z calcium dependent curves (panel B and C).

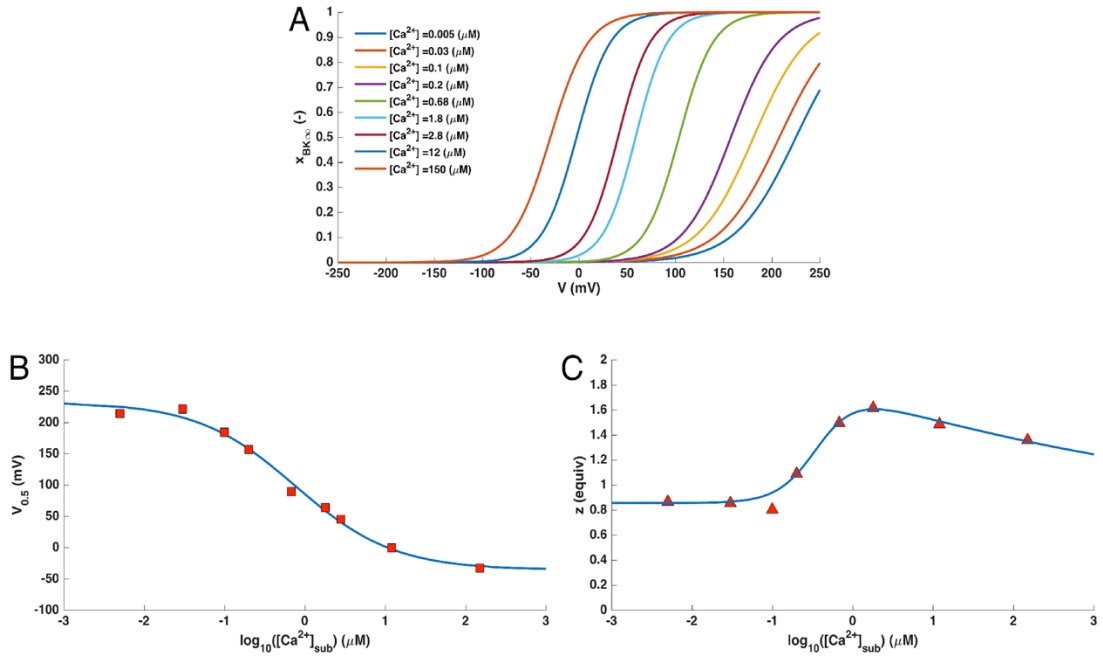


Figure 4.2 Characterization of the voltage and calcium dependence of BK channel

(A) Steady state activation curve $x_{BK\infty}$ at different intracellular Ca^{2+} concentrations. Increasing Ca^{2+} concentrations lead to shifts towards more negative potentials. $x_{BK\infty}$ is described by a Boltzmann fit curve (Eq. 2). (B and C) Calcium dependence of half maximal potential $V_{0.5}$ and valence z . $V_{0.5}$ is described by a sigmoidal curve (Eq. 6), whereas z is described by an asymmetrical double sigmoidal equation (Eq. 7). Experimental data are extracted from Orio & Latorre, (2005).

The kinetics of the gating variable $x_{BK\infty}$ is described by the first order differential equation:

$$\frac{dx_{BK}}{dt} = \frac{x_{BK,\infty} - x_{BK}}{\tau_{BK}} \quad (4.8)$$

where $\tau_{BK} = 5$ ms, according to Tabak *et al.*, (2011).

The effects of I_{BK} current on human SAN pacemaking were analysed using different values of the maximal conductance g_{BK} . In their study on BK channels, carried out on mouse SAN cells, Lai *et al.*, (2014) reported a peak value of 1.4 ± 4.6 pA/pF at +60 mV, resulting in a maximal conductance of $9.3 \mu\text{S}/\mu\text{F}$. (Tabak *et al.*, 2011) assumed $g_{BK} = 0.5$ nS for a cell with a capacitance of 10 pF leading to a specific capacitance of $50 \mu\text{S}/\mu\text{F}$. Lower values of conductance ($g_{BK} = 5$ and $10 \mu\text{S}/\mu\text{F}$) were also tested.

In order to quantify the effects of the inclusion of the SK and BK channels, cycle length (CL), maximum diastolic potential (MDP), AP duration at 20, 50, and 90% of repolarization (APD_{20} , APD_{50} and APD_{90}), diastolic depolarization rate in the first 100 ms after MDP (DDR_{100}), diastolic and systolic intracellular calcium ($Ca_{i,min}$ and $Ca_{i,max}$) and the intracellular calcium transient duration at 20%, 50% and 90% of calcium decay (TD_{20} , TD_{50} and TD_{90}) were compared in absence of the two currents (reference value) and in presence of I_{SK} and I_{BK} .

4.2.3 Optimization of the model when including I_{SK}

In order to observe how the model parameters might change in response to the inclusion of I_{SK} two set of automated optimization procedures were performed: the first one is based on the hypothesis that the actual value for g_{SK} in human SAN cells is known, thus only the parameters without experimental references undergo to optimization; the second set is based on the hypothesis that we don't know the actual value for g_{SK} , and includes it within the parameters to be optimized.

When the first hypothesis was assumed, the optimization procedure was performed with $g_{SK} = 4, 10$ and $41.7 \mu\text{S}/\mu\text{F}$; when g_{SK} was included into the optimization, the minimum of the cost function was searched for starting from different initial guesses ($g_{SK} = 4, 25$ and $41.7 \mu\text{S}/\mu\text{F}$).

For each optimization the initial guess for the other parameters was the nominal value of the SAN original model (see Appendix 1). The cost function was defined accordingly to the one adopted for the optimization of the human model starting from the rabbit model by Severi *et al.* (2012) (see Appendix 2).

4.3 Results

4.3.1 Effects of I_{SK} on AP and calcium transient in the human SAN

The inclusion of I_{SK} current into the human SAN AP model increased the beating rate. The amount of rate increase was strictly dependent on the I_{SK} maximal conductance, from 74 to 78 beats min^{-1} +5.4% for $g_{BK} = 4 \mu\text{S}/\mu\text{F}$ and dramatically large (from 74 up to 137 beats min^{-1} , +85.1%) for the highest simulated conductance value, $g_{SK} = 41.7 \mu\text{S}/\mu\text{F}$. The reduction of CL was due both to a remarkable decrease of APD ($\text{APD}_{90} = 98.5 \text{ ms}$ vs 161.5 ms without I_{SK}) and an increase of the DDR_{100} up to 80.2% (from 48.1 mV/s without I_{SK} to 86.7). MDP was virtually unchanged for $g_{SK} = 4$ and 10 $\mu\text{S}/\mu\text{F}$, whereas $g_{SK} = 41.7 \mu\text{S}/\mu\text{F}$ led to a hyperpolarization of about 5% ($\text{MDP} = -62.0$ vs $\text{MDP} = 58.9 \text{ mV}$). I_{SK} contribution during the AP also downsized the overshoot, lowering the action potential amplitude [from $\text{APA} = 85.3$ to 72.9 mV (-14.5%)].

The intracellular calcium showed a significant increase both in diastole ($\text{Ca}_{i,\text{min}} = 129 \text{ nM}$ +53.6%) and in systole ($\text{Ca}_{i,\text{min}} = 292 \text{ nM}$ +53.7%), for $g_{SK} = 41.7 \mu\text{S}/\mu\text{F}$.

The extracted features for $g_{SK} = 4, 10$ and 41.7 $\mu\text{S}/\mu\text{F}$, and the percentage difference with respect to the model without I_{SK} are reported in Table 4.1.

Figure 4.3 depicts the AP traces (panel A) and the comparison between I_{SK} for different values of g_{SK} and the total current simulated without the presence of I_{SK} as reference (panel B). I_{SK} reached its current density peak during the upstroke, when the $[\text{Ca}^{2+}]_{\text{sub}}$ is maximal (panel C); I_{SK} maximal amplitude, for 41.7 $\mu\text{S}/\mu\text{F}$, resulted higher than the outward I_{net} of the original human SAN model.

Table 4.1 – Effects on AP features of I_{SK} for $g_{SK} = 4, 10, 41.7 \mu S/\mu F$ in human SAN AP model

	Units	CTRL	$g_{SK} = 4 \mu S/\mu F$	$g_{SK} = 10 \mu S/\mu F$	$g_{SK} = 41.7 \mu S/\mu F$
CL ($\Delta CL\%$)	ms (%)	814	767 (-5.8)	686 (-15.7)	438 (-46.2)
Beating Rate ($\Delta BR\%$)	Beats min^{-1} (%)	74	78 (+5.4)	87 (17.6)	137 (+85.1)
APD ₉₀ (ΔAPD_{90})	ms (%)	161.5	155.5 (-3.7)	146.5 (-9.3)	98.5 (-39.0)
DDR ₁₀₀ (ΔDDR_{100})	mV/s (%)	48.1	52.6 (+9.4)	59.4 (23.5)	86.7 (+80.2%)
APA (ΔAPA)	mV (%)	85.3	82.8 (-2.9)	79.6 (-6.7)	72.9 (-14.5)
$Ca_{i,min}$ ($\Delta Ca_{i,min}$)	nM (%)	84	88 (+4.8)	96 (+14.3)	130 (+53.6)
$Ca_{i,max}$ ($\Delta Ca_{i,max}$)	nM (%)	189	198 (+4.2)	214 (+12.6)	292 (+53.7)

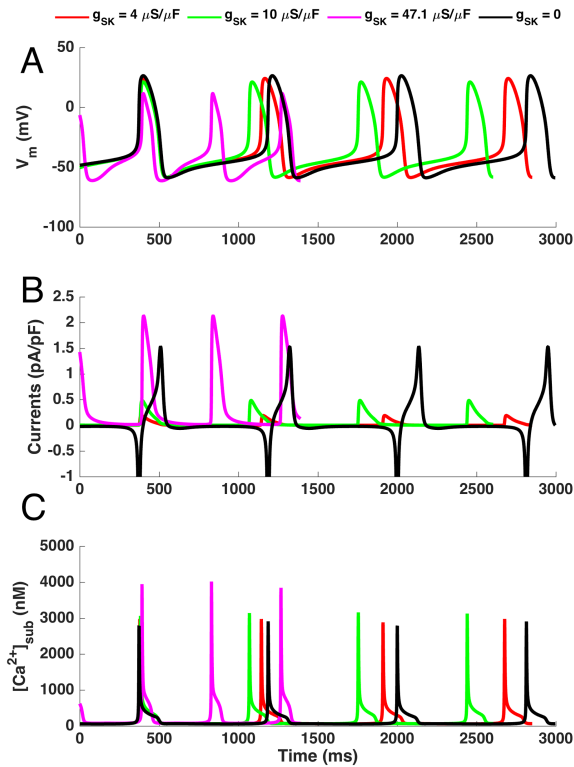


Figure 4.3 Effects of the introduction of I_{SK} on the human SAN AP (A) Time course of V_m for $g_{SK} = 4, 10$ and $41.7 \mu S/\mu F$, and in absence of I_{SK} (No I_{SK}). The overall shortening of CL is due to a faster repolarization (reduction of $APD_{20,50,90}$) and a steeper DD phase. (B) Comparison between the density of I_{SK} for $g_{SK} = 4, 10$ and $41.7 \mu S/\mu F$, and the total net current density in absence of I_{SK} . I_{SK} achieves the peak current density of, 0.19, 0.50 and 2.17 pA/pF for $g_{SK} = 4, 10$ and $41.7 \mu S/\mu F$, during the action potential.

4.3.2 Effects of I_{SK} on AP and calcium transient in the rabbit SAN

The effects of I_{SK} on the rabbit SAN AP model are consistent with the ones observed in the human SAN, even if less pronounced.

The beating rate increased from 169 up to 212 beats min^{-1} (+25.4%). CL showed a shortening up to -20% for $g_{SK} = 41.7 \mu\text{S}/\mu\text{F}$ (from 355 ms with no I_{SK} to 284 ms). Both the reduction of APD ($\text{APD}_{90} = 104$ vs 148.0 ms (-29.7%) without I_{SK}) and the increase of DDR_{100} ($\text{DDR}_{100} = 86.1$ vs 130.3 mV/s (+51.3%)) contributed to shrink the CL. MDP was virtually unchanged for all the tested values of g_{SK} even if it is worthwhile to point out that for $g_{SK} = 41.7 \mu\text{S}/\mu\text{F}$ MDP was slightly hyperpolarized (MDP = -58.0 mV in the original model vs MDP = -59.0 mV) in accordance with human SAN model. The inclusion of an outward (hence repolarizing) current during the AP affected also the OS, leading to a reduction of APA up to -9.8% (APA = 72.5 vs 80.4 mV) with $g_{SK} = 41.7 \mu\text{S}/\mu\text{F}$.

Intracellular calcium concentrations were almost unaffected except for a slight increase for $g_{SK} = 41.7 \mu\text{S}/\mu\text{F}$ (from $\text{Ca}_{i,\text{min}} = 83$ to 87 nM and from $\text{Ca}_{i,\text{min}} = 319$ to 321 nM).

Table 4.2 collects the main features of the simulated rabbit membrane potentials for $g_{SK} = 4, 10$ and $41.7 \mu\text{S}/\mu\text{F}$ and the percentage different for the features without I_{SK} .

Figure 4.4 shows the time course of the membrane potentials (panel A), I_{SK} currents (panel B) and the subsarcolemmal Ca^{2+} $[\text{Ca}^{2+}]_{\text{sub}}$ (panel C) for the different simulated conductance values. For $g_{SK} 41.7 \mu\text{S}/\mu\text{F}$ I_{SK} is comparable to I_{net} of the original rabbit SAN model.

Table 4.2 – Effects on AP features of I_{SK} for $g_{SK} = 4, 10, 41.7 \mu S/\mu F$ in rabbit SAN AP model

	Units	CTRL	$g_{SK} = 4 \mu S/\mu F$	$g_{SK} = 10 \mu S/\mu F$	$g_{SK} = 41.7 \mu S/\mu F$
CL ($\Delta CL\%$)	ms (%)	355	348 (-2.0)	338 (-4.8)	284 (-20.1)
Beating Rate ($\Delta BR\%$)	Beats min^{-1} (%)	169	172 (+1.8)	178 (+5.3)	212 (+25.4)
APD ₉₀ (ΔAPD_{90})	ms (%)	148.0	142 (-4.0)	134.5 (-9.1)	104.0 (-29.7)
DDR ₁₀₀ (ΔDDR_{100})	mV/s (%)	86.1	89.2 (+3.6)	95.1 (+10.4)	130.3 (51.3)
APA (ΔAPA)	mV (%)	80.4	79.1 (-1.6)	77.5 (-3.6)	72.5 (-9.8)
$Ca_{i,min}$ ($\Delta Ca_{i,min}$)	nM (%)	84	83 (-1.2)	83 (-1.2)	87 (+3.6)
$Ca_{i,max}$ ($\Delta Ca_{i,max}$)	nM (%)	319	319 (-)	319 (-)	321 (+0.6)

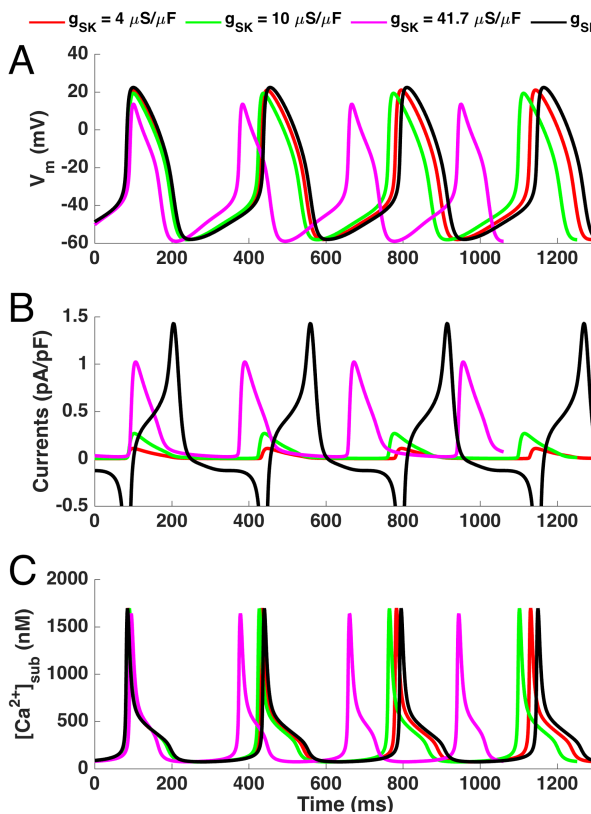


Figure 4.4 Effects of the introduction of

I_{SK} on the rabbit SAN AP (A) Time course of V_m for g_{SK} 4, 10 and $41.7 \mu S/\mu F$, and in absence of I_{SK} (No I_{SK}). The effect of the inclusion of I_{SK} is consistent with the human SAN even less extended. The shortening of CL is due to a reduction of $APD_{20,50,90}$ and a steeper DD phase.

(B) Comparison between the density of I_{SK} for g_{SK} 4, 10 and $41.7 \mu S/\mu F$ and the total net current density in absence of I_{SK} . I_{SK} achieves the peak current density of 0.11, 0.27 and 1.02 pA/pF for g_{SK} 4, 10 and $41.7 \mu S/\mu F$ during the action potential.

(C) Time course of Ca^{2+} in the sub-sarcolemmal compartment. $[Ca^{2+}]_{sub}$ increase is responsible for the peak of I_{SK} during the upstroke.

4.3.3 Effects of I_{BK} on AP and calcium transient in the human SAN

I_{BK} is an outward current that reaches its maximal activity during the rising phase of the AP (see Figure 5, panel a and B).

With the inclusion of I_{BK} , the simulated beating rate slightly increased (from 74 to 76 beats min^{-1} (+2.7%)).

CL showed a slight reduction (CL = 814 ms without I_{BK} vs 789 ms, -3.1%) for $g_{BK} = 50 \mu\text{S}/\mu\text{F}$, the maximal value tested for I_{BK} . The AP duration was virtually unchanged, (all the APD variations are <1%), whereas DDR_{100} increased up to +5.4%. MDP showed negligible variations and APA slightly decreased (APA = 85.3 vs 83.1 mV, -2.6% with $g_{BK} = 50 \mu\text{S}/\mu\text{F}$).

The intracellular calcium concentrations shifted towards higher values ($\text{Ca}_{i,\text{min}} = 84$ vs 86 nM, +3.1%, $\text{Ca}_{i,\text{max}} = 189$ vs 196 nM, +3.7% for $g_{BK} = 50 \mu\text{S}/\mu\text{F}$).

Table 4.3 – Effects on AP features of I_{BK} for $g_{BK} = 5, 9.3, 25$ and $50 \mu\text{S}/\mu\text{F}$ in human SAN AP model

	Units	CTRL	$g_{BK} = 5 \mu\text{S}/\mu\text{F}$	$g_{BK} = 9.3 \mu\text{S}/\mu\text{F}$	$g_{BK} = 25 \mu\text{S}/\mu\text{F}$	$g_{BK} = 50 \mu\text{S}/\mu\text{F}$
CL ($\Delta\text{CL}\%$)	ms (%)	814	812 (-0.2)	809 (-0.6)	802 (-1.5)	789 (-3.1)
Beating Rate ($\Delta\text{BR}\%$)	Beats min^{-1} (%)	74	74 (-)	74 (-)	75 (+1.3)	76 (+2.7)
APD_{90} (ΔAPD_{90})	ms (%)	161.5	161.0 (-0.3)	161.0 (-0.3)	161.0 (-0.3)	160.5 (-0.6)
DDR_{100} (ΔDDR_{100})	mV/s (%)	48.1	48.5 (+0.8)	48.6 (+1.0)	49.4 (+2.7)	50.7 (+5.4)
APA (ΔAPA)	mV (%)	85.3	85.1 (-0.2)	84.9 (-0.5)	84.3 (-1.2)	83.1 (-2.6)
$\text{Ca}_{i,\text{min}}$ ($\Delta\text{Ca}_{i,\text{min}}$)	nM (%)	84	84 (-)	84 (-)	85 (+1.2)	86 (+2.4)
$\text{Ca}_{i,\text{max}}$ ($\Delta\text{Ca}_{i,\text{max}}$)	nM (%)	189	190 (+0.5)	190 (+0.5)	192 (+1.6)	196 (+3.7)

Table 4.3 reports the features of the human SAN AP model for $g_{BK} = 5, 9.3, 25$ and $50 \mu\text{S}/\mu\text{F}$.

Figure 4.5 shows the membrane potentials (panel A) and I_{BK} currents (panel B). The maximum peak of I_{BK} occurred in the very early phase of AP and its amplitude resulted much smaller than the I_{net} of the original model.

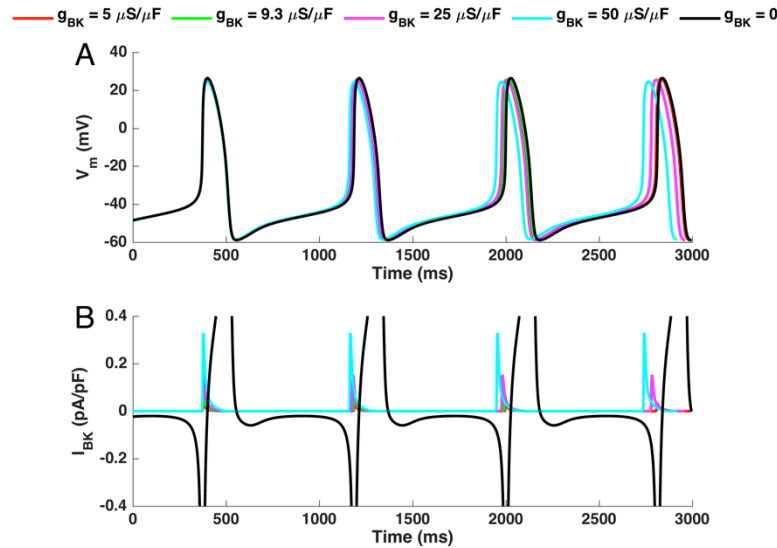


Figure 4.5 Effects of the inclusion of I_{BK} on the human SAN AP.

(A) Time course of V_m for $g_{BK} = 5, 9.3, 25, 50 \mu\text{S}/\mu\text{F}$, and in absence of I_{BK} . The overall effect is a slight shortening of CL due to an increase of DDR_{100} , whereas APD was virtually unchanged. (B)

Comparison between the time course of I_{BK} currents and I_{net} . I_{BK} is as small outward current in the very early stage of the upstroke. Peak values reached by I_{BK} are 0.032, 0.065, 0.15 and 0.33 pA/pF for $g_{BK} = 5, 9.3, 25, 50 \mu\text{S}/\mu\text{F}$ respectively

4.3.4 Effects of I_{BK} on AP and calcium transient in the rabbit SAN

I_{BK} on the Severi *et al.* (2012) rabbit SAN model led to a small increase of beating rate (from 169 up to 174 beats min^{-1} , +3.0%)

CL was shortened, showing a maximal reduction of 3.1% (from 355 of the original model in control conditions to 344 ms) for $g_{BK} = 50 \mu\text{S}/\mu\text{F}$. $APD_{20,50,90}$ and DDR_{100} worked in synergy towards CL shortening: the AP duration showed a contraction for the three repolarization phases ($APD_{20} = 83.0$ vs 75.0 ms (-9.6%), $APD_{50} = 121$ vs 114 ms (-5.8%) , $APD_{90} = 148.0$ vs 139 ms (-6.1%)) whereas $DDR_{100} = 86.1$ vs 87.7 mV/s (+1.9%) without I_{BK} and for $g_{BK} = 50 \mu\text{S}/\mu\text{F}$ respectively. MDP slightly shifted progressively to less negative potentials (MDP

= -58.0 vs -57.4 mV without I_{BK} and for $g_{BK}=50 \mu\text{S}/\mu\text{F}$) and APA decreased up to -7.3% (from APA = 80.4 mV in the original formulation to 74.5 mV with the maximal value of $g_{BK}=50 \mu\text{S}/\mu\text{F}$).

The intracellular calcium was virtually unaffected, showing a negligible decrease lower than 0.3%

Table 4.4 – Effects on AP features of I_{BK} for $g_{BK}= 5, 9.3, 25$ and $50 \mu\text{S}/\mu\text{F}$ in rabbit SAN AP model

	Units	CTRL	$g_{BK} = 5$ $\mu\text{S}/\mu\text{F}$	$g_{BK} = 9.3$ $\mu\text{S}/\mu\text{F}$	$g_{BK} = 25$ $\mu\text{S}/\mu\text{F}$	$g_{BK} = 50$ $\mu\text{S}/\mu\text{F}$
CL ($\Delta\text{CL}\%$)	ms (%)	355	354 (-0.3)	353 (-0.6)	350 (-1.4)	344 (-3.1)
Beating Rate ($\Delta\text{BR}\%$)	Beats min^{-1} (%)	169	169 (-)	170 (+0.6)	171 (+1.2)	174 (+3.0)
APD ₉₀ ($\Delta\text{APD}_{90}\%$)	ms (%)	148.0	146.0 (-1.4)	145.0 (-2.0)	143.0 (-3.4)	139.0 (-6.1)
DDR ₁₀₀ ($\Delta\text{DDR}_{100}\%$)	mV/s (%)	86.1	86.1 (-)	86.3 (+0.2)	86.9 (+0.9)	87.7 (+1.9)
APA ($\Delta\text{APA}\%$)	mV (%)	80.4	79.7 (-0.9)	79.0 (-1.7)	77.3 (-3.8)	74.5 (-7.3)
$\text{Ca}_{i,\text{min}}$ ($\Delta\text{Ca}_{i,\text{min}}\%$)	nM (%)	84	84 (-)	84 (-)	83 (-1.2)	83 (-1.2)
$\text{Ca}_{i,\text{max}}$ ($\Delta\text{Ca}_{i,\text{max}}\%$)	nM (%)	319	319 (-)	319 (-)	318 (-0.3)	318 (-0.3)

Table 4.4 reports the features of the human SAN AP model for $g_{BK} = 5, 9.3, 25$ and $50 \mu\text{S}/\mu\text{F}$.

Figure 4.6 shows the membrane potentials (panel A) and I_{BK} currents (panel B). As in the human model, I_{BK} showed small maximal amplitude compared with the I_{net} of the original model.

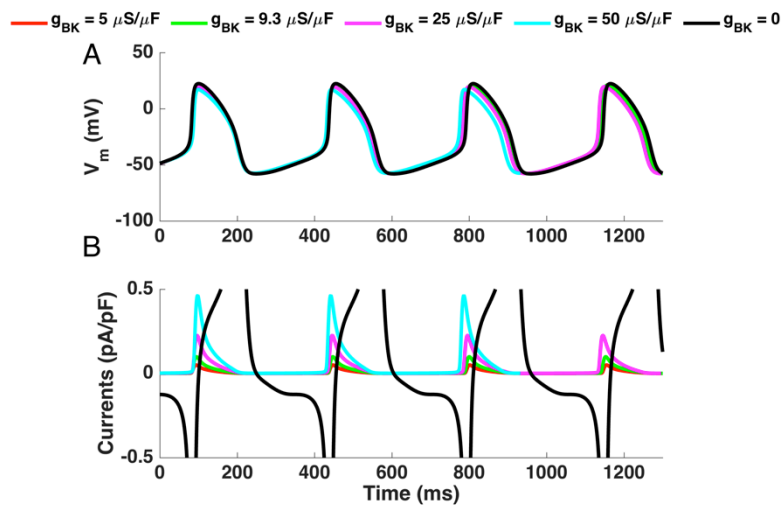


Figure 4.6 Effects of the inclusion of I_{BK} on the rabbit SAN AP.

(A) Time course of V_m for $g_{BK} = 5, 9.3, 25, 50 \mu\text{S}/\mu\text{F}$, and in absence of I_{BK} . The overall effect is a shortening of CL due to a faster APD and steeper DDR_{100} .

(B) Comparison between the time course of I_{BK} currents and I_{net} . I_{BK} is as small outward current in the very early stage of the upstroke. Peak values reached by I_{BK} are slightly higher than in human SAN model (0.050, 0.099, 0.23 and 0.46 pA/pF for $g_{BK} = 5, 9.3, 25, 50 \mu\text{S}/\mu\text{F}$, respectively).

(B) Comparison between the time course of I_{BK} currents and I_{net} . I_{BK} is as small outward current in the very early stage of the upstroke. Peak values reached by I_{BK} are slightly higher than in human SAN model (0.050, 0.099, 0.23 and 0.46 pA/pF for $g_{BK} = 5, 9.3, 25, 50 \mu\text{S}/\mu\text{F}$, respectively).

4.3.5 Combining I_{SK} and I_{BK} in the human and in the rabbit SAN

In order to investigate the interaction between I_{SK} and I_{BK} , the simultaneous presence of the two calcium sensitive currents was tested, combining the values of g_{SK} (no I_{SK} , 4, 10 and 41.7 $\mu\text{S}/\mu\text{F}$) and g_{BK} (no I_{BK} , 5, 9.3, 25 and 50 $\mu\text{S}/\mu\text{F}$). Among the 20 total simulations, we compared the effects for (1) $g_{SK} = 41.7 \mu\text{S}/\mu\text{F}$ and $g_{BK}=0$ (maximal value for I_{SK} and no I_{BK} , (2) $g_{SK} = 0$ and $g_{BK} = 50 \mu\text{S}/\mu\text{F}$ (no I_{SK} and maximal value for I_{BK}) –the results relative to these two configurations are already reported in the previous sections–, with (3) $g_{SK} = 41.7$ and $g_{BK} = 50 \mu\text{S}/\mu\text{F}$ (both I_{SK} and I_{BK} at the highest intensity) on the AP features.

In the human SAN model the simulation with $g_{SK} = 41.7 \mu\text{S}/\mu\text{F}$ and $g_{BK} = 50 \mu\text{S}/\mu\text{F}$ led to a faster beating rate (140 beats min^{-1} , +89.2%), a reduction of CL (from 814 of the original model to 429 ms (-47.3%)), APD_{90} (from 162 to 96 ms (-40.6%)) and APA (from 85.3 to 71.6 mV (-16.1%)). DDR_{100} remarkably increased (from 48.1 to 88.6 mV/s (+84.2%)) as the diastolic and systolic calcium concentrations did ($\text{Ca}_{i,\text{min}} = 84$ nM in the original model vs $\text{Ca}_{i,\text{min}} = 130$ nM (+54.8%), $\text{Ca}_{i,\text{max}} = 298$ nM vs 189 nM (+57.7%)).

The comparison of the percentage variations of HR, CL, APD_{90} , DDR_{100} , APA, $\text{Ca}_{i,\text{min}}$ and $\text{Ca}_{i,\text{max}}$ in the three cases under study with respect to the original model (i.e with no I_{SK} and I_{BK}) highlighted an almost negligible interaction (see Table 4.5), since the total effect due to the presence of both I_{SK} and I_{BK} is close to the sum of the effects due to the separate presence of I_{SK} and I_{BK} .

Table 4.5 – Effects on AP features of the maximal intensity of I_{SK} , I_{BK} and the $I_{SK} + I_{BK}$ in the human SAN AP model

	Units	Original model	I_{SK} max $g_{SK} = 41.7$ $g_{BK} = 0$	I_{BK} max $g_{SK} = 0$ $g_{BK} = 50$	I_{SK}, I_{BK} max $g_{SK} = 41.7$ $g_{BK} = 50$
CL ($\Delta CL\%$)	ms (%)	814	438 (-46.2)	789 (-3.1)	429 (-47.3)
Beating Rate ($\Delta BR\%$)	Beats min^{-1} (%)	74	137 (+85.1)	76 (+2.7)	140 (+89.2)
APD ₉₀ (ΔAPD_{90})	ms (%)	161.5	98.5 (-39.0)	160.5 (-0.6)	96.0 (-40.6)
DDR ₁₀₀ (ΔDDR_{100})	mV/s (%)	48.1	86.7 (+80.2%)	50.7 (+5.4)	88.6 (+84.2)
APA (ΔAPA)	mV (%)	85.3	72.9 (-14.5)	83.1 (-2.6)	71.6 (-16.1)
$Ca_{i,min}$ ($\Delta Ca_{i,min}$)	nM (%)	84	129 (+53.6)	86 (+3.1)	130 (+54.8)
$Ca_{i,max}$ ($\Delta Ca_{i,max}$)	nM (%)	189	292 (+54.5)	196 (+3.7)	298 (+57.7)

In rabbit SAN, the employment of the maximal values of g_{SK} and g_{BK} was responsible for the increasing of beating rate (216 beats min^{-1} , +27.8%) and CL shortening, with respect to the original model, accordingly to what observed in human SAN even if less pronounced (from CL = 355 to 278 ms (-21.7%)). The effect due to outward currents during the action potential led the voltage membrane to a faster repolarization (APD₉₀ changed from 148.0 to 102.0 ms (-31.1%)) and a lower APA (from 80.4 to 69.2 mV (-13.9%)). Another contribution to the shortening of CL came from DDR₁₀₀, which became steeper (DDR₁₀₀ = 86.1 vs 127.5 mV/s (+48.1%)).

Unlike what observed in the human model, the intracellular calcium concentrations were almost unaffected, with a slight increase of $Ca_{i,min}$ (from 84 to 88 nM (+4.8%)) and a virtually unchanged $Ca_{i,max}$ (from 319 to 321 nM (+0.6%))

Table 4.6 reports the comparison of the percentage variations of HR, CL, APD₉₀, DDR₁₀₀, APA, Ca_{i,min} and Ca_{i,max} in the three cases under study with respect to the original model.

Table 4.6 – Effects on AP features of the maximal intensity of I_{SK}, I_{BK} and the I_{SK} + I_{BK} in the rabbit SAN AP model

	Units	Original model	I _{SK} max g _{SK} = 41.7 g _{BK} = 0	I _{BK} max g _{SK} = 0 g _{BK} = 50	I _{SK} , I _{BK} max g _{SK} = 41.7 g _{BK} = 50
CL (ΔCL%)	ms (%)	355	284 (-20)	344 (-3.1)	278 (-21.7)
Beating Rate (ΔBR%)	Beats min ⁻¹ (%)	169	212 (+25.4)	174 (+3.0)	216 (+27.8)
APD ₉₀ (ΔAPD ₉₀)	ms (%)	148.0	104.0 (-29.7)	139.0 (-6.1)	102.0 (-31.1)
DDR ₁₀₀ (ΔDDR ₁₀₀)	mV/s (%)	86.1	130.3 (51.3)	87.7 (+1.9)	127.5 (+48.1)
APA (ΔAPA)	mV (%)	80.4	72.5 (-9.8)	74.5 (-7.3)	69.2 (-13.9)
Ca _{i,min} (ΔCa _{i,min})	nM (%)	84	87 (+3.6)	83 (-1.2)	88 (+4.8)
Ca _{i,max} (ΔCa _{i,max})	nM (%)	319	321 (+0.6)	317 (-0.6)	321 (+0.6)

4.3.6 Features and parameters of the models after the optimization procedure

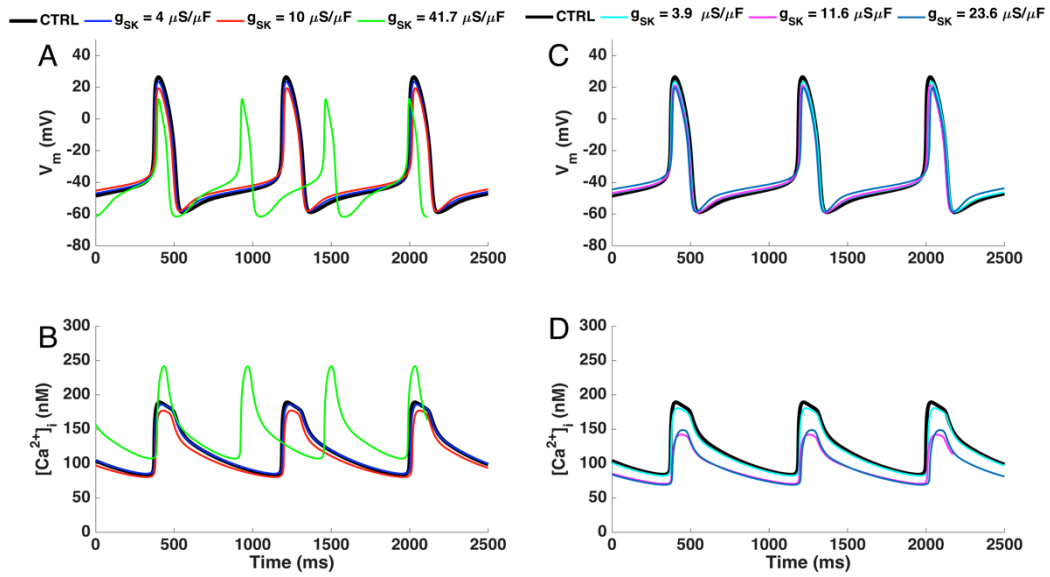


Figure 4.7 Timecourse of V_m (A,C) and $[Ca^{2+}]_i$ (B,D) of the original (CTRL. black trace) and the optimized models including I_{SK} . For (A) and (B) g_{SK} was supposed constant, whereas for (C) and (D) g_{SK} was optimized starting from different initial guesses (4, 25 and 41.7 $\mu S/\mu F$)

As first, the optimization performed keeping g_{SK} constant ($g_{SK} = 4, 10$ and $41.7 \mu S/\mu F$) were analyzed. The three models showed $CL = 816 (+0.2\%)$, $818 (+0.5\%)$ and $533 \text{ ms} (-34.5\%)$ respectively. MDP slightly depolarized (MDP = -58.3 and -58.1 mV) for $g_{SK} = 4$ and $10 \mu S/\mu F$, whereas it went towards more negative potential (MDP = -61.7 mV) for $g_{SK} = 41.7 \mu S/\mu F$. The presence of a higher I_{SK} led to shorter APD_{90} than the original model ($APD_{90} = 152, 139$ and 98 ms for $g_{SK} = 4, 10$ and $41.7 \mu S/\mu F$ respectively) and a remarkably higher DDR_{100} ($DDR_{100} = 61.1 (+26.9\%)$, $73.9 (+53.7\%)$ and $78.9 \text{ mV/s} (+64.1\%)$).

The optimization procedure led to $Ca_{i,min} = 85 (+1.2\%)$, $80 (-4.8\%)$. and $107 \text{ nM} (27.4\%)$ and $Ca_{i,max} = 186 (-1.6\%)$, $177 (-6.3\%)$ and $241 \text{ nM} (+27.5\%)$.

The values of the extracted features from the 3 optimized model assuming g_{SK} constant and their variations from the ones extracted from the original model are collected in Table 4.7.

Table 4.7 Comparison between experimental and simulated features for CTRL and optimized model including I_{SK} assuming g_{SK} constant.

Features	Units	Exp	CTRL	g_{SK} 4 $\mu S/\mu F$	g_{SK} 10 $\mu S/\mu F$	g_{SK} 41.7 $\mu S/\mu F$
APA ($\Delta APA\%$)	mV	78.0 \pm 4.5	85.3	81.7 (-4.2)	77.5 (-9.1)	74.3 (-12.9)
MDP ($\Delta\%$)	mV	-61.7 \pm 4.3	-58.9	-58.3 (-1.0)	-58.1 (-1.4)	-61.7 (4.7)
CL ($\Delta CL\%$)	ms	828 \pm 15	814	816 (0.2)	818 (0.4)	533 (-34.5)
dV/dt_{max} ($\Delta dV/dt_{max}\%$)	V/s	4.6 \pm 1.2	7.4	6.6 (-11.4)	5.6 (-24.9)	6.1 (-18.1)
APD₂₀ ($\Delta APD_{20}\%$)	ms	64.9 \pm 16.9	98.5	91.0 (-7.6)	83.0 (-15.7)	52.5 (-46.7)
APD₅₀ ($\Delta APD_{50}\%$)	ms	101.5 \pm 27.0	136.0	127.0 (-6.6)	115.5 (-15.1)	77.5 (-43.0)
APD₉₀ ($\Delta APD_{90}\%$)	ms	143.5 \pm 34.9	161.5	152.0 (-5.9)	139.0 (-13.9)	97.5 (-39.6)
DDR₁₀₀ ($\Delta DDR_{100}\%$)	V/s	48.9 \pm 18	48.1	61.1 (26.9)	73.9 (53.7)	78.9 (64.1)
$Ca_{i,min}$ ($\Delta Ca_{i,min}\%$)	nM	110	84	85 (1.2)	80 (-4.8)	107 (27.4)
$Ca_{i,max}$ ($\Delta Ca_{i,max}\%$)	nM	220	189	186 (-1.8)	177 (-6.4)	241 (27.5)
TD₂₀ ($\Delta TD_{20}\%$)	ms	138.9	136.7	132.0 (-3.4)	116.7 (-14.7)	72.0 (-47.3)
TD₅₀ ($\Delta TD_{50}\%$)	ms	217.4	206.3	204.0 (-1.1)	181.3 (-12.1)	107.7 (-47.8)
TD₉₀ ($\Delta TD_{90}\%$)	ms	394	552.3	554.0 (0.3)	535.0 (-3.1)	333.7 (-39.6)
Cs^+ CL increase ($\Delta increase\%$)	%	26	28.0	28.1 (0.4)	28.6 (2.1)	33.4 (19.3)

The inclusion of g_{SK} within the set of parameters to be optimized led to a maximal conductance of 3.9, 11.6 and 23.6 $\mu S/\mu F$ starting from the initial guesses of 4, 25 and 41.7 $\mu S/\mu F$, respectively. The resulting models showed CL = 819 (+0.6), 814 (-) and 820 ms (+0.2%), negligible changes in MDP [-58.6 (+0.5%), -59.0 (-0.2%), -58.5 mV (0.7%)] shorter APD₉₀ [153 (-5.3%), 143 (-11.5%) and 134.5 ms, (-16.7%)] and a remarkably higher DDR₁₀₀ (59.6 (+23.8%), 63.1 (+31.3%) and 84 V/s (+74.7%).

Calcium transient reached lower levels both for $Ca_{i,min}$ [82 (-2.4%), 70 (-16.7%) and 69 nM (-17.9%)] and $Ca_{i,max}$ [181 (-4.2%), 142 (-24.9%) and 149 nM (-21.2%)].

Table 4.8 reports the complete list of the features extracted from the three optimized models, and their variation from the nominal model, including g_{SK} within the parameter set to be optimized.

Table 4.8 Comparison between experimental and simulated features for CTRL and optimized model including I_{SK} , with g_{SK} optimized.

Features	Units	Exp	CTRL	$g_{SK} 1G$ 4 $\mu S/\mu F$	$g_{SK} opt$ 25 $\mu S/\mu F$	$g_{SK} opt$ 41.7 $\mu S/\mu F$
APA ($\Delta APA\%$)	mV	78.0 \pm 4.5	85.3	82.1 (-3.7)	80.1 (-6.0)	78.1 (-8.4)
MDP ($\Delta\%$)	mV	-61.7 \pm 4.3	-58.9	-58.6 (-0.5)	-59.0 (0.2)	-58.5 (-0.7)
CL ($\Delta CL\%$)	ms	828 \pm 15	814	819 (0.6)	814.0 (0.0)	820 (0.7)
dV/dt_{max} ($\Delta dV/dt_{max}\%$)	V/s	4.6 \pm 1.2	7.4	6.6 (-10.2)	6.2 (-15.6)	5.9 (-20.1)
APD₂₀ ($\Delta APD_{20}\%$)	ms	64.9 \pm 16.9	98.5	92.0 (-6.6)	84.0 (-14.7)	77.5 (-21.3)
APD₅₀ ($\Delta APD_{50}\%$)	ms	101.5 \pm 27.0	136.0	128.0 (-5.9)	119.0 (-12.5)	111.5 (-18.0)
APD₉₀ ($\Delta APD_{90}\%$)	ms	143.5 \pm 34.9	161.5	153.0 (-5.3)	143.0 (-11.5)	134.5 (-16.7)
DDR₁₀₀ ($\Delta DDR_{100}\%$)	V/s	48.9 \pm 18	48.1	59.6 (23.8)	63.1 (31.3)	84.0 (74.7)
$Ca_{i\ min}$ ($\Delta Ca_{i\ min}\%$)	nM	110	84	82 (-2.4)	70 (-16.7)	69 (-17.9)
$Ca_{i\ max}$ ($\Delta Ca_{i\ max}\%$)	nM	220	189	181 (-4.2)	142 (-24.9)	149 (-21.2)
TD₂₀ ($\Delta TD_{20}\%$)	ms	138.9	136.7	131.0 (-4.2)	125.0 (-8.6)	116.3 (-14.9)
TD₅₀ ($\Delta TD_{50}\%$)	ms	217.4	206.3	202.0 (-2.1)	199.0 (-3.5)	185.0 (-10.3)
TD₉₀ ($\Delta TD_{90}\%$)	ms	394	552.3	554.0 (0.3)	563.0 (1.9)	548.0 (-0.8)
$Ca^{+} CL$ increase ($\Delta increase\%$)	%	26	28.0	28.0 (-0.1)	28.6 (2.2)	28.2 (0.7)

Each optimization returned a new set of parameters. For $g_{SK} = 4 \mu S/\mu F$, P_{CaT} and P_{CaL} showed the highest variations with respect to the values of the original model (+13.7% and -5.9% respectively). The model with $g_{SK} = 10 \mu S/\mu F$ was characterized by a strong increase of P_{CaT} and k_s (+23% and +44.3%. respectively) and a decrease of V_{dL} (-10.4%). The set of parameters with $g_{SK} = 41.7 \mu S/\mu F$ reported an increase of K_{NaCa} (+5.1%) and a decrease of V_{dL} (-9.5%).

Table 4.9 collects the parameters obtained by the optimization procedure and the percentage changes with respect to the original set when g_{SK} is kept constant.

Table 4.9 Comparison between the parameter of the original model (CTRL) and the ones obtained after the automatic optimization. g_{SK} is assumed to be constant

Parameters	Units	CTRL	g_{SK} 4 $\mu S/\mu F$	g_{SK} 10 $\mu S/\mu F$	g_{SK} 41.7 $\mu S/\mu F$
K_{NaCa} ($\Delta K_{NaCa}\%$)	(-)	3.343	3.377 (1.0)	3.356 (0.4)	3.512 (5.1)
K_{up} ($\Delta K_{up}\%$)	mM	0.000286	0.000301 (5.3)	0.000275 (-4.0)	0.000287 (0.3)
P_{CaT} ($\Delta P_{CaT}\%$)	nA/mM	0.0413	0.0470 (13.7)	0.0508 (23.0)	0.0410 (-0.8)
P_{CaL} ($\Delta P_{CaL}\%$)	nA/mM	0.458	0.431 (-5.9)	0.412 (-9.9)	0.432 (-5.5)
k_{dL} ($\Delta k_{dL}\%$)	mV	4.3372	4.3237 (-0.3)	4.4521 (2.6)	4.4985 (3.7)
V_{dL} ($\Delta V_{dL}\%$)	mV	-16.4509	-16.2203 (-1.4)	-14.7427 (-10.4)	-14.8818 (-9.5)
τ_{difCa} ($\Delta \tau_{difCa}\%$)	s	5.47E-05	5.54E-05 (1.2)	5.48E-05 (0.3)	5.73E-05 (4.7)
k_s ($\Delta k_s\%$)	1/s	1.48E+08	1.49E+08 (0.5)	2.14E+08 (44.3)	1.53E+08 (3.5)
$K_{f,CM}$ ($\Delta K_{f,CM}\%$)	mM/s	1642000	1582759 (-3.6)	1654255 (0.7)	1686092 (2.7)
$K_{f,CQ}$ ($\Delta K_{f,CQ}\%$)	mM/s	175.4	175.4 (0.0)	163.8 (-6.6)	182.2 (3.9)
$i_{NaK,max}$ ($\Delta i_{NaK,max}\%$)	nA	0.0810	0.0783 (-3.4)	0.0660 (-18.5)	0.0834 (2.9)
g_{Kur} ($\Delta g_{Kur}\%$)	μS	1.54E-04	1.49E-04 (-3.3)	1.41E-04 (-8.6)	1.47E-04 (-4.4)

The initial guess for g_{SK} (4, 25 and 41.7 $\mu S/\mu F$) affected the final set of the optimized parameters. When the initial guess was $g_{SK} = 4 \mu S/\mu F$, P_{CaT} showed an increase of 12.2%, whereas P_{CaL} and g_{Kur} underwent to a decrease of -6.4% and -7.3% respectively. Starting from $g_{SK} = 25 \mu S/\mu F$ led to an increase of K_{NaCa} , P_{CaT} , $\tau_{dif,Ca}$ and k_{fCQ} (+37.1%, +18.9%, +25.3% and +21.2% respectively) and a decrease of P_{CaL} and g_{Kur} , (-18.4% and -16.0% respectively). Finally, for $g_{SK} = 41.7 \mu S/\mu F$ as initial guess, K_{NaCa} and P_{CaT} notably increased (+39.8% and +36.7%, respectively). whereas V_{dL} , k_s , $I_{NaK,max}$ and g_{Kur} decreased (-14.2%, -28.8%, -28.8% and -26.2%, respectively).

Table 4.10 collects the values of each parameter set and the percentage variation with respect to the original model. Figure 4.X depicts the timecourse for the V_m (panel A) and for $[Ca^{2+}]_i$ (panel B) of the original model and the optimized models including g_{SK} .

Table 4.10 Comparison between the parameter of the original model (CTRL) and the ones obtained after the automatic optimization. g_{SK} is included in the optimization procedure

Parameters	Units	CTRL	$g_{SK} IG$ 4 $\mu S/\mu F$	$g_{SK} opt$ 25 $\mu S/\mu F$	$g_{SK} opt$ 41.7 $\mu S/\mu F$
K_{NaCa} ($\Delta K_{NaCa}\%$)	(-)	3.343	3,450 (3,2)	4,583 (37,08)	4.674 (39.8)
K_{up} ($\Delta K_{up}\%$)	mM	0.000286	0,000287 (0,3)	0,000284 (-0,74)	0.000280 (-2.2)
P_{CaT} ($\Delta P_{CaT}\%$)	nA/mM	0.0413	0,0464 (12,2)	0,0491 (18,90)	0.0565 (36.7)
P_{CaL} ($\Delta P_{CaL}\%$)	nA/mM	0.458	0,4286 (-6,4)	0,3737 (-18,36)	0.4321 (-5.6)
k_{dL} ($\Delta k_{dL}\%$)	mV	4.3372	4,3329 (-0,1)	4,3708 (0,78)	4.4083 (1.6)
V_{dL} ($\Delta V_{dL}\%$)	mV	-16.4509	-16,2668 (-1,1)	-16,2096 (-1,47)	-14.1127 (-14.2)
τ_{diffCa} ($\Delta \tau_{diffCa}\%$)	s	5.47E-05	5,60E-05 (2,4)	6,85E-05 (25,31)	5.46E-05 (-0.1)
k_s ($\Delta k_s\%$)	1/s	1.48E+08	1,51E+08 (2,1)	1,47E+08 (-0,75)	1.05E+08 (-28.8)
$K_{f,CM}$ ($\Delta K_{f,CM}\%$)	mM/s	1642000	1660992 (1,2)	1603605 (-2,34)	2074266 (26.3)
$K_{f,CQ}$ ($\Delta K_{f,CQ}\%$)	mM/s	175.4	180,5 (2,9)	212,5 (21,18)	151.8 (-13.5)
$i_{NaK,max}$ ($i_{NaK,max}\%$)	nA	0.0810	0,0792 (-2,3)	0,0763 (-5,83)	0.0577 (-28.8)
g_{Kur} ($\Delta g_{Kur}\%$)	μS	1.54E-04	1,43E-04 (-7,3)	1,29E-04 (-16,03)	1.14E-04 (-26.2)

4.4 Discussion

In this work we assessed the effects on AP waveform and calcium transient due to the inclusion of the small (I_{SK}) and large (I_{BK}) conductance Ca^{2+} -dependent potassium currents into the human SAN computational model we recently developed and into the rabbit SAN parent model. The preliminary sensitivity analysis allowed us to observe how AP waveform and calcium transient were affected by different levels of I_{SK} , I_{BK} and by the simultaneous presence of the two currents under investigation.

4.4.1 Effects of the inclusion of I_{SK} in human and rabbit SAN models

The inclusion of I_{SK} into the human SAN model led to the increase of the beating rate due to the APD shortening (in all its phases) and DDR increase. The effects are less pronounced in rabbit SAN model, where the maximal increase of beating rate (+25.4% vs +85.1% in human SAN) was obtained with $g_{SK} = 41.7 \mu S/\mu F$. As the human model, the Severi *et al.* (2012) rabbit SAN showed a shortening of APD, a steeper DD phase and negligible MDP changes. The inclusion of I_{SK} , in this two computational SAN, is able to modulate the beating rate both acting on the diastolic depolarization and in the action potential.

This result is in accordance with the effects of the administration of 10 nM apamin reported by Chen *et al.*, (2013) on rabbit SAN single cells and by Torrente *et al.* (2017) on murine SAN single cells, where a 50% block of I_{SK} was responsible for a decrease of beating rate respectively of 25 and 18%. Torrente *et al.* (2017) reported an APD_{90} prolongation of +25% and a decrease of DDR of -44%. The inclusion of I_{SK} in rabbit model caused a comparable APD_{90} decrease (-29.7%) whereas the in human model the APD_{90} shortening was stronger (-39%). About DDR, the rabbit model showed a closer behavior ($\Delta DDR\% = +51.2\%$), whereas human model showed an extremely high DDR increase (+119%). In our simulations MDP was virtually unchanged for g_{SK} up to 10 $\mu S/\mu F$ and hyperpolarized for the maximal employed conductance ($g_{SK} = 41.7 \mu S/\mu F$). There

is no agreement about MDP in literature, since Torrente *et al.* (2017) noticed statistically differences of MDP with 10 nM of apamin (-60 vs -64 mV in control) whereas Chen *et al.* (2013) reported no significant changes.

The time course of the currents during DD phase allowed us to investigate the underlying mechanisms about the modulation of beating rate (Figure 4.8). Notably, how the inclusion of the outward I_{SK} led to the increase in SAN beating rate is not straightforward. This mechanism is well explained, maybe exacerbated, in human SAN for $g_{SK} = 41.7 \mu S/\mu F$ (Figure 4.8 A, B). The activation of I_{SK} during AP affected the maximal voltage (overshoot, OS) reached by the membrane. A lower OS was responsible for a remarkably lower I_{Kr} activation. Since I_{Kr} is characterized by very fast inactivation kinetics, at the beginning of the DD phase recovery from inactivation is completed, whereas the slower deactivation process is still on the way. As a result, the amount of I_{Kr} at this stage is dependent on the amount of voltage-dependent activation reached during the AP. For this reason, the I_{SK} -induced OS reduction causes a remarkable decrease of I_{Kr} during the DD phase, which is not compensated by the strong I_{SK} outward current; this speeds up the depolarization process and leads to early triggering of I_{CaL} , and of the consequent action potential. The outward contribution of I_{SK} during the AP is clearly evident when $g_{SK} = 41.7 \mu S/\mu F$. In this configuration, I_{SK} overcompensate the low repolarizing contribution of I_{Kr} leading not only to a shorter APD but also to a more negative MDP.

The results showed by the two models are similar, even if less extended in the rabbit SAN. In the rabbit SAN model the reduction of I_{Kr} was still present, but less pronounced. As in the human model, a faster increase of V_m triggered I_{CaL} sooner (Figure 4.8 C,D)

Our results point out that the effect of I_{SK} on pacemaking rate can be substantial. Whilst the actual size (i.e. maximal conductance value) of the I_{SK} current in human SAN is still an open issue, it has been possible, through simulations, to make a sort of sensitivity analysis of the pacemaking to different levels of the current. Results confirm that it is crucial to determine the real amount of I_{SK} in human SAN in order to quantitatively evaluate its eventual contribution to pacemaking. Simulation results suggest that even a quite small amount of I_{SK}

($g_{SK} = 4 \mu S/\mu F$) leads to small but not negligible changes in the main biomarkers. As a relevant example, CL was reduced by 6%, down to 767 ms, which is out of the experimental range (828 ± 21 ms, $m \pm sd$) reported by Verkerk *et al.* (2007) in human SAN cells.

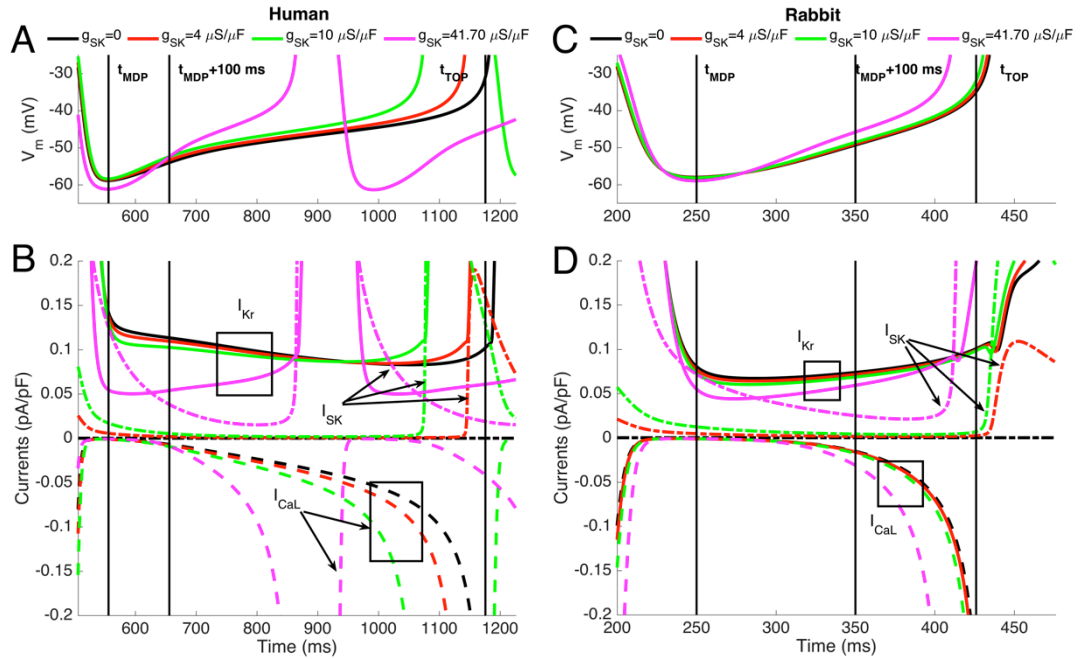


Figure 4.8 : Underlying mechanisms for I_{SK} DD modulation in human (A-B) and rabbit (C-D) SAN. Membrane potential (A-C) and main currents (B-D) involved in modulation of DD phase are shown. In the human SAN model (A-B) the steeper DD is due to a lower outward I_{Kr} that leads to a faster activation of I_{CaL} . In the rabbit SAN model (C-D) the mechanism is similar to the human SAN but it is less pronounced, leading to a less steeper DD phase.

4.2 Effects of the inclusion of I_{BK} in human and rabbit SAN models

Simulations using different values of maximal conductance (g_{BK}) pointed out that contribution to the pacemaking modulation was negligible leading to a maximum increase of beating rate of 2.7% in the human SAN model. The small increase was mainly due to the shortening of DD (-3.6%) whereas APD and MDP were virtually unchanged. The analysis of DD phase showed that the presence of

I_{BK} led to a slightly higher inward net current, especially during the very early DD and during the late phase. The slightly enhanced contribution of I_{NaCa} and the decreased amplitude of I_{Kr} were synergically responsible for the increased inward I_{net} in the early DD; the faster activation of I_{CaL} increased I_{net} in the late DD.

The rabbit SAN model showed a similar increase in beating rate (+3.0%); differently from the human model, the change in rate was attributable to the shortening of APD without any variation of DD duration. As it concerns the underlying mechanisms, the I_{BK} directly affected the action potential phase thanks to its outward contribution and indirectly the DD. Indeed, DD duration was unchanged since a compensating effect of inward and outward current. As I_{SK} does, I_{BK} was responsible for a lower overshoot that affected I_{Kr} also during DD; in the early DD the lower contribution of that outward current caused a higher inward I_{net} , with respect to the original model. The compensation occurs in second part of DD, where I_{Na} and I_{NaCa} reached lower inward amplitudes.

The simulated effects of the inclusion of I_{BK} are characterized by lower extents and different mechanism compared to the experimental data obtained with administration of BK channels blockers. Imlach *et al.* (2010) reported heart rate reduction of -31% *in vivo* and -34% in isolated hearts in a mouse model for the administration of PAX 8 mg/Kg and 1 μ M respectively. Lai *et al.*, (2014) observed a strong decrease of beating rate (-56.%) in isolated SAN cells with a remarkable prolongation of DD and no significant changes in APD_{50} and MDP. According to the speculative suggested mechanisms by Lai *et al.*, (2014), I_{BK} contribution could enhance I_f and I_{Na} , by hyperpolarizing the membrane, or could involve Ca^{2+} inactivation. Our model suggested that I_{BK} mainly acts during AP and can indirectly affect DD via I_{Kr} and slight changes in inward currents as I_{NaCa} . The discrepancy among experimental data and simulated results deserve further investigation; among the possible hypothesis, PAX could be not highly specific for BK channels or there could be discrepancies due to the different species analyzed (mouse vs rabbit and human); moreover, the models could not adequately reproduce Ca^{2+} transient during the time interval where I_{BK} could play an important role in DD modulation.

4.3 Combining I_{SK} and I_{BK} in the SAN models

SK and BK channels are both Ca^{2+} sensitive, but they have different biophysical properties. The simulation of the simultaneous contribution of I_{SK} and I_{BK} was carried out in order to observe some behavior emerging from the interaction between the two currents. The extracted features showed that interaction were almost negligible since the total effect was close to the sum of two separated currents (see Table 4.6 and 4.7)

4.4 Optimized models

The inclusion of g_{SK} within the model brought the simulated features out of the physiological values and it made necessary to perform new optimization procedures.

When g_{SK} was assumed to be known (hypothesis 1), for $g_{SK} = 41.7 \mu S/\mu F$ the optimized model showed features far from the experimental range, suggesting that such a high value of conductance for I_{SK} is highly unlikely.

The inclusion of g_{SK} within the optimization procedure – g_{SK} assumed unknown, hypothesis 2– showed that models with $g_{SK} = 11.6$ and $23.6 \mu S/\mu F$ still have a good behavior, even if with a steeper DDR_{100} and a shrunked CaT. The increase of value of g_{SK} led to a higher number of parameter involved in remarkable changes. Among the main target of the optimization there are P_{CaT}, P_{CaL}, V_{dL} , and K_{NaCa} , involved in the regulation of the steepness of DDR_{100} during the early phase and the CaT, and g_{Kur} , that affects the APD.

4.5 Final Remarks

The presence of $I_{K,Ca}$ channels in human SAN tissue was reported by (Chandler *et al.*, 2009) through the gene expression characterization, but unfortunately no electrophysiological data acquired directly on human SAN cells are available. Our

model is based on data obtained with heterologous systems, e.g. HEK cells, *Xenopus* oocytes (Orio & Latorre, 2005; Orio *et al.*, 2006), and small animal models as rabbit (Chen *et al.*, 2013) and mouse (Zhang *et al.*, 2008; Imlach *et al.*, 2010; Lai *et al.*, 2014; Torrente *et al.*, 2017). In this perspective, we are exploiting our computational SAN model to obtain insights on how $I_{K,Ca}$ could work into the human cellular environment.

References

- Chandler NJ, Greener ID, Tellez JO, Inada S, Musa H, Molenaar P, DiFrancesco D, Baruscotti M, Longhi R, Anderson RH, Billeter R, Sharma V, Sigg DC, Boyett MR & Dobrzynski H (2009). Molecular architecture of the human sinus node insights into the function of the cardiac pacemaker. *Circulation* 119, 1562–1575.
- Chen W-T, Chen Y-C, Lu Y-Y, Kao Y-H, Huang J-H, Lin Y-K, Chen S-A & Chen Y-J (2013). Apamin modulates electrophysiological characteristics of the pulmonary vein and the Sinoatrial Node. *Eur J Clin Invest* 43, 957–963.
- Giles WR & Imaizumi Y (1988). Comparison of potassium currents in rabbit atrial and ventricular cells. *J Physiol* 405, 123–145.
- Hirschberg B, Maylie J, Adelman JP & Marrion NV (1998). Gating of Recombinant Small-Conductance Ca-activated K^+ Channels by Calcium. *J Gen Physiol* 111, 565–581.
- Imlach WL, Finch SC, Miller JH, Meredith AL & Dalziel JE (2010). A Role for BK Channels in Heart Rate Regulation in Rodents. *PLoS ONE*; DOI: 10.1371/journal.pone.0008698.
- Kennedy M, Bers DM, Chiamvimonvat N & Sato D (2017). Dynamical effects of calcium-sensitive potassium currents on voltage and calcium alternans. *J Physiol* 595, 2285–2297.
- Köhler M, Hirschberg B, Bond CT, Kinzie JM, Marrion NV, Maylie J & Adelman JP (1996). Small-Conductance, Calcium-Activated Potassium Channels from Mammalian Brain. *Science* 273, 1709–1714.
- Koumi S, Sato R & Hayakawa H (1994). Modulation of the delayed rectifier K^+ current by apamin in guinea-pig heart. *Eur J Pharmacol* 261, 213–216.

- Lai MH, Wu Y, Gao Z, Anderson ME, Dalziel JE & Meredith AL (2014). BK channels regulate sinoatrial node firing rate and cardiac pacing in vivo. *Am J Physiol - Heart Circ Physiol* 307, H1327–H1338.
- Lancaster B, Nicoll RA & Perkel DJ (1991). Calcium activates two types of potassium channels in rat hippocampal neurons in culture. *J Neurosci* 11, 23–30.
- Orio P & Latorre R (2005). Differential Effects of $\beta 1$ and $\beta 2$ Subunits on BK Channel Activity. *J Gen Physiol* 125, 395–411.
- Orio P, Torres Y, Rojas P, Carvacho I, Garcia ML, Toro L, Valverde MA & Latorre R (2006). Structural determinants for functional coupling between the beta and alpha subunits in the Ca^{2+} -activated K^{+} (BK) channel. *J Gen Physiol* 127, 191–204.
- R Latorre, A Oberhauser, P Labarca & Alvarez and O (1989). Varieties of Calcium-Activated Potassium Channels. *Annu Rev Physiol* 51, 385–399.
- Schreiber M & Salkoff L (1997). A novel calcium-sensing domain in the BK channel. *Biophys J* 73, 1355–1363.
- Severi S, Fantini M, Charawi LA & DiFrancesco D (2012). An updated computational model of rabbit sinoatrial action potential to investigate the mechanisms of heart rate modulation. *J Physiol* 590, 4483–4499.
- Tabak J, Tomaiuolo M, Gonzalez-Iglesias AE, Milescu LS & Bertram R (2011). Fast activating voltage- and calcium-dependent potassium (BK) conductance promotes bursting in pituitary cells: a dynamic clamp study. *J Neurosci Off J Soc Neurosci* 31, 16855–16863.
- Toro L, Wallner M, Meera P & Tanaka Y (1998). Maxi-KCa, a Unique Member of the Voltage-Gated K Channel Superfamily. *Physiology* 13, 112–117.
- Torrente AG, Zhang R, Wang H, Zaini A, Kim B, Yue X, Philipson KD & Goldhaber JI (2017). Contribution of small conductance K^{+} channels to sinoatrial node pacemaker activity: insights from atrial-specific $\text{Na}^{+}/\text{Ca}^{2+}$ exchange knockout mice. *J Physiol* 595, 3847–3865.
- Tuteja D, Xu D, Timofeyev V, Lu L, Sharma D, Zhang Z, Xu Y, Nie L, Vázquez AE, Young JN, Glatzer KA & Chiamvimonvat N (2005). Differential expression of small-conductance Ca^{2+} -activated K^{+} channels SK1, SK2, and SK3 in mouse atrial and ventricular myocytes. *Am J Physiol-Heart Circ Physiol*.
- Verkerk AO, Wilders R, Borren MMGJ van, Peters RJG, Broekhuis E, Lam K, Coronel R, Bakker JMT de & Tan HL (2007). Pacemaker current (I_f) in the human sinoatrial node. *Eur Heart J* 28, 2472–2478.

Xu Y, Tuteja D, Zhang Z, Xu D, Zhang Y, Rodriguez J, Nie L, Tuxson HR, Young JN, Glatter KA, Vázquez AE, Yamoah EN & Chiamvimonvat N (2003). Molecular Identification and Functional Roles of a Ca²⁺-activated K⁺ Channel in Human and Mouse Hearts. *J Biol Chem* 278, 49085–49094.

Zhang Q, Timofeyev V, Lu L, Li N, Singapuri A, Long MK, Bond CT, Adelman JP & Chiamvimonvat N (2008). Functional Roles of a Ca²⁺-Activated K⁺ Channel in Atrioventricular Nodes. *Circ Res* 102, 465–471.

Chapter 5

Pace-and-Drive of the Human Sinoatrial Node A Preliminary Computational Investigation

The content of this chapter is published in:

“Pace and drive of the human Sinoatrial Node – A preliminary Computational Investigation”

Alan Fabbri¹, Axel Loewe², Ronald Wilders³, Stefano Severi¹

Computing in Cardiology 2017, in press

¹*University of Bologna, Cesena, Italy*

²*Karlsruhe Institute of Technology (KIT), Karlsruhe, Germany*

³*Academic Medical Center (AMC), Amsterdam, The Netherlands*

Abstract

The sinoatrial node (SAN) is the natural pacemaker of our heart. How this small tissue is able to drive a remarkably larger number of intrinsically quiescent atrial cells is still debated; a computational investigation of the underlying mechanisms can help to better understand the SAN's ability to pace-and-drive the surrounding atrium.

Aim of this work is to elucidate how the human SAN action potential can successfully be captured by and propagate into the surrounding atrial tissue.

The Fabbri et al. and the Courtemanche et al. models were used to describe the human SAN and atrial cells respectively. The behaviour of two coupled regions was investigated varying the interregional conductivity (σ) and relative size. Simulations showed that it requires at least an isopotential SAN region 2.85 times wider than the atrial one. A 1D strand of homogeneously coupled SAN and atrial elements was used to identify an interval for σ showing pace-and-drive behaviour (100 SAN vs 100 atrial elements) and to investigate the source-sink interplay (10 and 50100 SAN vs 100 atrial elements). The 1D strand successfully drove the atrium for $\sigma = [0.08-36]$ S/m; a stronger source, with a higher number of SAN elements led to a wider σ range that allowed pace-and-drive behaviour, whereas a stronger sink did not affect the behaviour of the tissue.

This preliminary work shows the ability of a small human SAN region to pace-and-drive the surrounding atrial tissue. Further investigations are needed to explore different conductivity configurations, including spatial gradients.

5.1 Introduction

The sinoatrial node (SAN) is a small, specialized tissue located in the right atrium and responsible for the physiological heart rate in healthy subjects. Its self-oscillating action potential (AP) starts the chain of events that leads to the electrical activation and the subsequent mechanical contraction of the whole heart. When two or more cardiac cells are coupled, the behaviour of each cell is not only determined by its intrinsic properties governing membrane ion currents but also by the electrotonic currents that flow through the gap junctions shared with neighbouring cells. Experimental work by Jalife (1984) showed that two pacemaker centres beating at different frequencies mutually entrained and reached a common cycle length (CL) intermediate between the mean period of the fast and the slow one, once electrically coupled. A computational study by Joyner *et al.* (1983) showed that regional changes in membrane properties (e.g. plateau currents) affected the spatial distribution of the AP properties along the tissue due to the effects of electrotonic currents.

The propagation of the electrical signal from the SAN tissue to the atrial tissue was investigated in animal models, especially in rabbits, starting from the 1980s. The fair amount of experimental data provided a strong base for building computational models, which investigated the required level of coupling to successfully pace-and-drive the atrial tissue. Among them, Joyner & van Capelle, (1986) systematically explored the behaviour of two coupled regions and of 2D radially symmetric cardiac tissue slices composed of sinoatrial and atrial rabbit-specific cell models.

Recent studies by Chandler *et al.* (2011) and Csepe *et al.* (2016) shed light on the anatomical structure and conduction pathways of the human SAN. However, a computational model able to describe the propagation of the electrical stimulus from the SAN to the atrial human tissue is still lacking.

The aims of the present work are 1) characterizing the behaviour of two discrete electrically coupled SAN and atrial regions when varying the membrane surface and the gap junction conductivity, 2) identifying the range of conductivity

that yields a pace-and-drive behaviour in a homogeneous 1D strand, and 3) investigating the source-sink interplay by varying the number of SAN and atrial elements in the strand.

5.2. Methods

In order to investigate the mechanisms involved in the electrical propagation of the AP in human sinoatrial and atrial tissue, the human-specific cell models by Fabbri *et al.* (2017) and Courtemanche *et al.* (1998), for the sinoatrial node and for the atrial cells, respectively, were chosen.

5.2.1 Coupling of discrete sinoatrial node and atrial regions

The study about the electrical interaction between two discrete regions (SAN and atrial) was performed varying two parameters that describe the strength of the coupling, i.e. the conductivity (σ [S]) and the dimensions of the investigated region (k_{ratio} [-]).

In particular, k_{ratio} is defined as:

$$k_{\text{ratio}} = \frac{C_{\text{SAN,cell}} S_{\text{ATR}}}{C_{\text{ATR,cell}} S_{\text{SAN}}}$$

where $C_{\text{SAN,cell}} = 57$ pF (Fabbri *et al.*, 2017) and $C_{\text{ATR,cell}} = 100$ pF (Courtemanche *et al.*, 1998); The terms relative to the membrane surface, S_{SAN} and S_{ATR} , affect the calculation of the coupling current among the two tissue regions. In this sense, they represent the amount of membrane of one region that is involved in the coupling with the other.

The behaviour of the coupled-regions system was tested for σ between 10^{-8} and $5 \cdot 10^{-5}$ S and k_{ratio} between 0.057 (S_{SAN} ten times bigger than S_{ATR}) and 0.57 ($S_{\text{SAN}} = S_{\text{ATR}}$).

5.2.2 1D tissue strand

The monodomain model was adopted to describe the propagation of the electrical stimulus from the sinoatrial to the atrial tissue. The identification of a range of conductivity values that yields pace-and-drive behaviour was obtained through a mono-dimensional strand composed of 100 sinoatrial (1 cm) and 100 atrial cellular elements (1 cm); each element had a side length of 100 μm . We employed a constant value of conductivity σ_h [S/m] along the whole tissue, simulating an electrically homogenous strand.

The source-sink interplay was investigated adopting a number of SAN cells equal to 10, 50 and 100 against 100 or 200 atrial cells. The strength of the source and the sink was investigated by comparing the cycle length (CL) of the leftmost sinoatrial element (index #0) with the CL relative to an uncoupled setup ($\sigma_h = 0$). The conduction velocity (CV) was estimated measuring the time delay between the activation of the 25th and 75th atrial cells assuming a constant propagation velocity.

The Safety Factor (SF) is an index that provides quantification about the robustness of electrical propagation in the cardiac tissue. In more detail, SF quantifies the surplus of current delivered to a cell relative to the amount required to depolarize the membrane to threshold (Boyle & Vigmond, 2010).

The expression of SF used by Romero et al. (2009) is given by:

$$\text{SF} = \frac{C_m \Delta V_m + Q_{\text{out}}}{Q_{\text{in}}} \quad (5.2)$$

where Q_{in} and Q_{out} is the charge provided by the upstream and to downstream cell respectively. The charge is computed over the time of rise of the membrane voltage, from resting potential to the upstroke peak.

The Kirchoff's current law for cell N, without external current stimuli, provides the balance of the currents involved in the propagation of AP:

$$I_{in} - I_{out} = C_m \frac{\partial V_m}{\partial t} + I_{ion} \quad (5.3)$$

Integrating (5.3) over the rise time, and rearranging the terms:

$$\frac{C_m \Delta V_m + Q_{out} + Q_{ion}}{Q_{in}} = 1 \quad (5.4)$$

which combined with (5.2) yields

$$SF = 1 - \frac{Q_{ion}}{Q_{in}} \quad (5.5)$$

If Q_{ion} is inward, then $SF > 1$ and the AP successfully propagates; on the contrary if $SF < 1$ the propagation fails.

5.3 Results

5.3.1 Coupling of discrete sinoatrial node and atrial regions

The coupled-region system showed three distinct behaviours as can be seen in Figure 1: a) not-pace, where the automaticity of the sinoatrial node is completely lost, b) pace-but-not-drive, where the sinoatrial node keeps the automaticity but it is not able to activate the atrial region, and c) pace-and-drive, where the automatic sinoatrial region APs are successfully captured by the atrial tissue and propagate. $\sigma = 9 \cdot 10^{-8}$ S was the maximal value that led to the pace-but-not-drive behaviour irrespective of the value of k_{ratio} . For k_{ratio} equal to 0.057 and 0.1 the system switched from pace-but-not-drive to pace-and-drive upon increasing σ , whereas for k_{ratio} of 0.285 or higher, the not-pace behaviour followed the pace-but-not-drive one.

For $k_{\text{ratio}} = 0.1425$ (sinoatrial surface four times higher than the atrial one) the pace-and-drive behaviour was disrupted by a not-pace interval for $\sigma = [3-7] \cdot 10^{-8}$ S. The outward current provided by the SAN region in the not pace configuration did not allow the SAN to reach the threshold, stopping in this way the automaticity. For higher values the pace-and-drive behaviour was recovered with a SAN-like AP waveform of the atrial region.

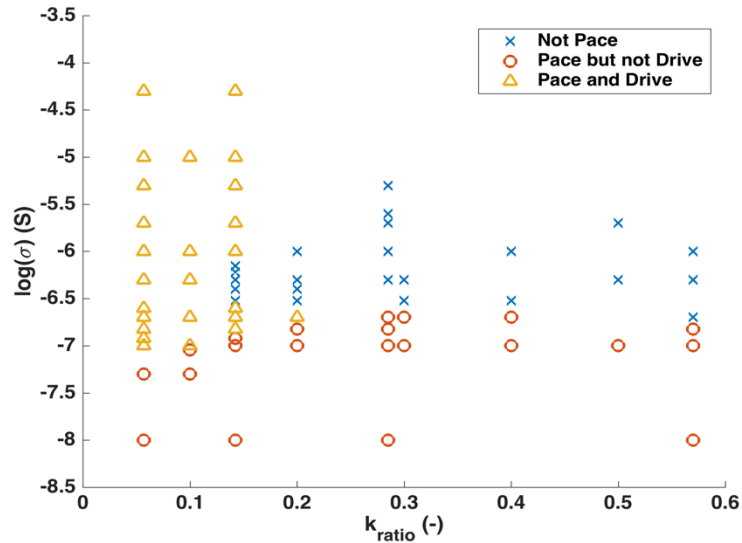


Figure 5.1 Results of the simulations for two coupled regions: SAN and atrial, varying the membrane surface (k_{ratio}) and the strength of the coupling (σ). Not-pace (crosses), pace-but-not-drive (circles) and pace-and-drive (triangles) behaviour was observed.

5.3.2 1D tissue strand

The mono-dimensional homogeneous strand composed of 100 SAN and 100 atrial elements showed a pace-and-drive behaviour for $\sigma_h = [0.08 - 36]$ S/m. Lower values of σ_h led to a pace-but-not-drive behaviour, whereas values above stopped the automaticity of the sinoatrial node (not-pace). Figures 2 and 3 compare the AP waveform and the time course of the fast sodium current (I_{Na}) at the transition between SAN and atrial regions for $\sigma_h = 1$ S/m. The SAN AP showed a progressive hyperpolarization (MDP = -66.6 for the last SAN element versus -58.9 mV in the uncoupled cell) due to the presence of the atrial tissue (see Fig. 2, panel A). The upstroke of the SAN elements close to the atrium was steeper due to a larger I_{Na} , almost negligible in cells far from the transitional zone (see Fig. 3, panel B). The atrial elements close to the SAN ones showed a depolarized resting potential in comparison with the single cell model ($V_{rest} \approx -66$ mV and a slight depolarization during the diastolic phase for the first atrial cell,

$V_{\text{rest,uncoupled}} \approx -81$ mV); the typical spike-notch-dome morphology was lost in the first atrial elements, which showed an intermediate waveform between sinus-nodal and atrial.

The atrial waveform and the resting potential were recovered after 10 elements (1 mm) from the transitional region (Fig. 3, panel A). A more hyperpolarized resting potential led to higher I_{Na} availability, remarkably higher than in the first atrial elements (Fig. 3, panel B).

An increase of the number of the sinoatrial elements led to a wider σ_h range yielding pace-and-drive behaviour. In particular, the upper bound of the interval

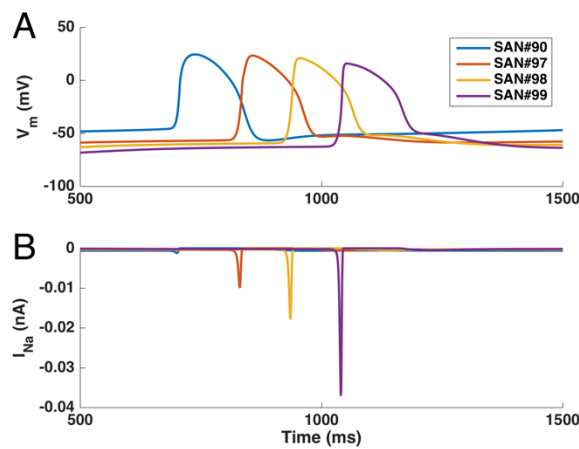


Figure 5.2 Comparison of A) AP waveform and B) I_{Na} time course of SAN elements close to the transitional zone for $\sigma_h = 1$ S/m. V_m and I_{Na} time courses are delayed by 100 ms for sake of clarity. Preceding SAN APs look like SAN#90.

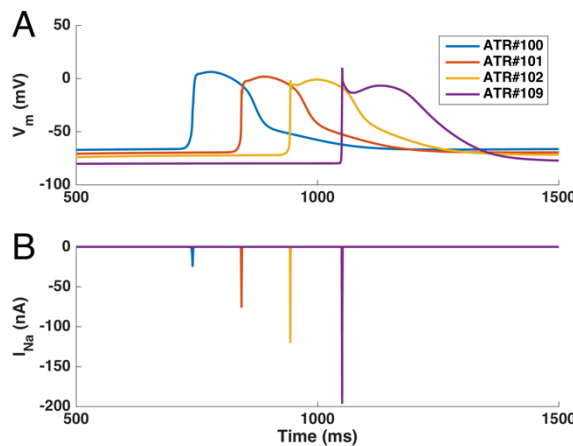


Figure 5.3 Comparison of A) AP waveform and B) I_{Na} time course of atrial elements close to the transitional zone for $\sigma_h = 1$ S/m. V_m and I_{Na} time courses are delayed by 100 ms for sake of clarity. Note the different ordinate scale of panel B compared to Figure 2. Following atrial APs look like ATR #109.

was shifted towards higher values, with $\sigma_h = 0.3, 9$ and 36 for a SAN tissue composed of 10, 50 and 100 elements, respectively. Furthermore, a higher number of SAN cells caused a lower CL, i.e. faster beating, at the same value of σ_h (e.g. for $\sigma_h = 0.15$ S/m, CL = 1001, 838 and 837 ms for 10, 50 and 100 SAN elements). In combination, longer CLs could be obtained using higher numbers of SAN elements ($CL_{\max} = 1738, 2100$ and 2726 ms) as depicted in the σ_h vs. CL plot in Figure 4. Changing the number of atrial elements from 100 to 200 did alter behaviour neither qualitatively nor quantitatively.

Estimated CV varied between 0.685 cm/s for $\sigma_h = 0.08$ S/m and $CV = 83.3$ cm/s for $\sigma_h = 35$ S/m.

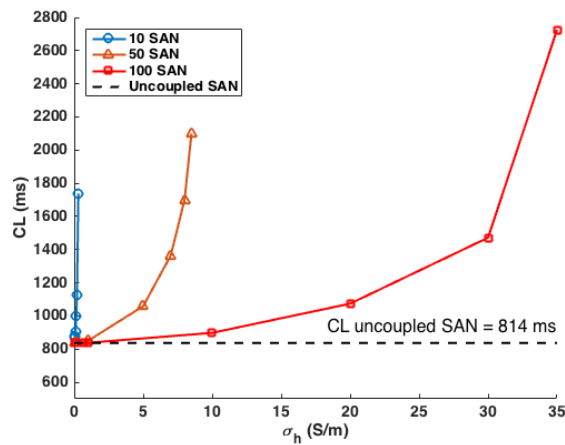


Figure 5.4 : Source-sink interplay. CL of SAN elements at different conductivity values for a homogeneous 1D strand composed of 10, 50 and 100 SAN against 100 atrial elements. The dashed line indicates the intrinsic CL of the SAN cell elements.

In this work the definition of SF reported in section 5.2.2 was applied to the 1D strands composed by 10,50, and 100 SAN and 100 atrial cells at several values of coupling (σ_h).

Figure 5.5 resumes the values of the computed SF for each simulation. $SF = 1$ represents the threshold that distinguishes successful propagation from failure. In all the three configurations the pace-but-not-drive (red ellipse) and the not pace (red rectangle) behavior showed $SF < 1$.

The strand composed by 10 SAN cells showed a sharp increase of SF during the transitions from pace-but-not-drive to pace-and-drive ($SF = 0.48$ at $\sigma_h = 0.06$ S/m, $SF = 2.28$ at $\sigma_h = 0.08$ S/m) and a drop from pace-and-drive to not pace ($SF = 2.06$ at $\sigma_h = 0.34$ S/m, $SF = 0.6$ at $\sigma_h = 0.35$ S/m).

The strands made by 50 and 100 SAN cells showed a sharp increase of SF during the transition from pace-but-not-drive to pace-and-drive ($SF = 0.51$ at $\sigma_h = 0.06$ S/m, $SF = 2.51$ at $\sigma_h = 0.08$ S/m in both the strands); SF progressively got close to the threshold for high levels of coupling and then became lower than 1 when the propagation failed ($SF = 1.12$ at $\sigma_h = 9.00$ S/m, $SF = 0.93$ at $\sigma_h = 9.50$ S/m for 50 SAN cells, $SF = 1.18$ at $\sigma_h = 37.00$ S/m, $SF = 0.98$ at $\sigma_h = 40.00$ S/m for 100 SAN cells).

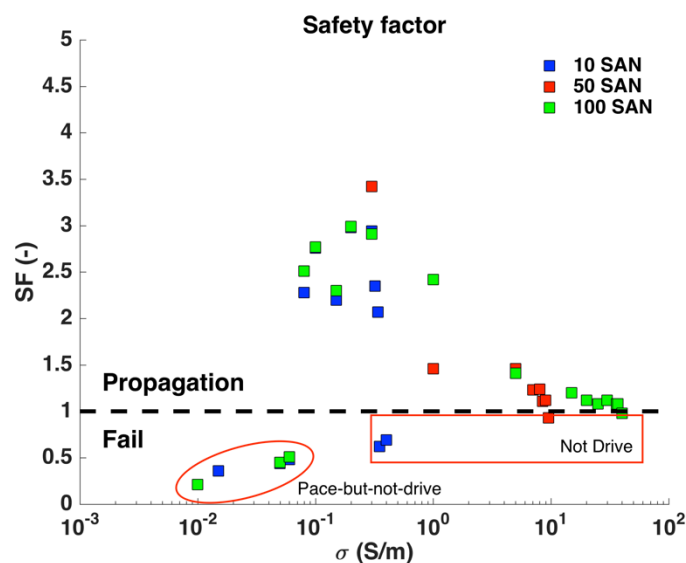


Figure 5.5 Safety factor and AP propagation: Comparison of the safety factor for three strand configurations: 10 SAN (blue squares), 50 SAN (red) and 100 SAN (green) cells coupled with 100 atrial cells. $SF = 1$ is the threshold that distinguishes between successful or failing AP propagation.

5.4 Discussion

The present work represents a preliminary investigation on the propagation of the AP from the sinoatrial node to the atrial tissue using human-specific computational membrane models.

The *in silico* experiments showed that the human SAN model is able to pace-and-drive the atrial tissue under specific conditions of electrotonic coupling and cell/tissue dimensions. The system of two discrete coupled regions showed pace-and-drive behaviour for $k_{\text{ratio}} \leq 0.2$. This value is obtained for a $S_{\text{SAN}}:S_{\text{ATR}}$ equal to 2.85:1. The assumption of isopotential region is satisfied by two coupled cells. In that case the $S_{\text{SAN}}:S_{\text{ATR}}$ ratio means that 4 SAN cells are needed to successfully excite the atrial one. If we extend the discussion to 2 isopotential tissues, the $S_{\text{SAN}}:S_{\text{ATR}} = 4:1$ means that the surface of the SAN region that participates to the coupling should be four times more extended than the atrial one. This result is in agreement with the study by Joyner & van Capelle (1986), who showed that the isopotential SAN region surface must be wider than the atrial one in order to successfully activate the latter (Figure 3 in [3], panels A and B).

The disruption of the pace-and-drive for $\sigma = [3-7] \cdot 10^{-8}$ S and the following recovery of the driving of the atrial region for higher values of coupling is intriguing. The behaviour showed by our simulations differs from the results obtained by Joyner & van Capelle (1986), where varying the strength of coupling, keeping the same dimensions of SAN or atrial region, did not show a recovery from not pace. Interestingly, in our simulations, the disruption distinguished two different kinds of pace-and-drive, the one with an atrial-like and another with a SAN-like waveform for the atrial region.

The analysis of the behaviour of a 1D strand composed of 100 SAN and 100 atrial elements with homogenous coupling revealed that the pace-and-drive region in the σ_h space is quite extended and also that the SAN elements are strong enough to drive the atrial tissue without being electrically shielded from the load generated by the atrium. However the conductivity σ_h corresponding to a physiological conduction velocity in the atrial tissue ($CV \approx 85$ cm/s) yields a too

long CL (= 2726 ms) compared to physiological heart rates. This discrepancy suggests a non-homogeneous conductivity *in vivo*.

The SAN elements located in the transitional zone showed a “peripheral-like” AP (Chandler *et al.*, 2009) even if the employed SAN AP model does not distinguish between central and peripheral cells. The enhanced contribution of I_{Na} due to the electrical load of the atrial tissue was responsible for the faster upstroke of the SAN elements close to the atrial ones.

The source-sink interplay plays an important role in excitation propagation, especially for the SAN that has to drive the remarkable electrical load generated by the surrounding atrial tissue. Our simulations point out that the range extension of the conductivity that allows the pace-and-drive behaviour highly depends on the number of the SAN elements (strength of the source). The carried out simulations with 100 and 200 atrial elements showed the same behaviour, at the same conditions of source strength. This result suggests that the further downstream 100 atrial elements do not substantially increase the electrical load of the sink.

The calculation of SF for the strands composed by 10, 50, 100 SAN and 100 atrial cells satisfied the criterion $SF > 1$ for a successful propagation. The strand made by 10 SAN cells showed a different behavior with respect the 50 and 100 SAN cells with a sharp drop of SF during the transition pace-and-drive and not pace. For increasing values of σ_h the 50 and 100 SAN cells strands showed a progressive decrease of SF and “distorsion” of the AP waveform, characterized by less pronounced peaks during the upstroke.

The focus on simple geometrical setups (two discrete coupled regions and a 1D strand), even if far from a physiological configuration allowed observing the fundamental electrical behaviour without confounding factors due to a complex geometry.

Another important aspect is the dependency of the results – e.g. range of the conductance for successful propagation, conduction velocity, source and sink interplay – from the computational atrial model adopted. Several human atrial AP models are available on the market (Nygren *et al.*, 1998; Koivumäki *et al.*, 2011; Grandi *et al.*, 2011) and a their major electrophysiological properties have been

compared by Wilhelms et al. (2013) showing different behaviors (e.g. rate-dependent differences in APD and AP upstroke). Further investigations using different atrial models can be helpful to test how the electrical propagation of AP is affected by the employed model in the simulations.

Next steps should take into account the cellular and gap junction heterogeneity, introducing differences in ion channel conductances and spatial gradients of coupling (Joyner & van Capelle, 1986; Inada *et al.*, 2014). An appropriate coupling configuration will be also helpful to obtain both a physiological conduction velocity and CL, not achievable in our 1D homogenous strand.

References

- Chandler N, Aslanidi O, Buckley D, Inada S, Birchall S, Atkinson A, Kirk D, Monfredi O, Molenaar P, Anderson R, Sharma V, Sigg D, Zhang H, Boyett M & Dobrzynski H (2011). Computer Three-Dimensional Anatomical Reconstruction of the Human Sinus Node and a Novel Paranodal Area. *Anat Rec Adv Integr Anat Evol Biol* 294, 970–979.
- Chandler NJ, Greener ID, Tellez JO, Inada S, Musa H, Molenaar P, DiFrancesco D, Baruscotti M, Longhi R, Anderson RH, Billeter R, Sharma V, Sigg DC, Boyett MR & Dobrzynski H (2009). Molecular architecture of the human sinus node insights into the function of the cardiac pacemaker. *Circulation* 119, 1562–1575.
- Courtemanche M, Ramirez RJ & Nattel S (1998). Ionic mechanisms underlying human atrial action potential properties: insights from a mathematical model. *Am J Physiol - Heart Circ Physiol* 275, H301–H321.
- Csepe TA, Zhao J, Hansen BJ, Li N, Sul LV, Lim P, Wang Y, Simonetti OP, Kilic A, Mohler PJ, Janssen PML & Fedorov VV (2016). Human sinoatrial node structure: 3D microanatomy of sinoatrial conduction pathways. *Prog Biophys Mol Biol* 120, 164–178.
- Fabbri A, Fantini M, Wilders R & Severi S (2017). Computational analysis of the human sinus node action potential: model development and effects of mutations. *J Physiol* 595, 2365–2396.
- Inada S, Zhang H, Tellez JO, Shibata N, Nakazawa K, Kamiya K, Kodama I, Mitsui K, Dobrzynski H, Boyett MR & Honjo H (2014). Importance of Gradients in Membrane Properties and Electrical Coupling in Sinoatrial Node Pacing. *PLOS ONE* 9, e94565.

- Jalife J (1984). Mutual entrainment and electrical coupling as mechanisms for synchronous firing of rabbit sino-atrial pace-maker cells. *J Physiol* 356, 221–243.
- Joyner RW & van Capelle FJ (1986). Propagation through electrically coupled cells. How a small SA node drives a large atrium. *Biophys J* 50, 1157–1164.
- Joyner RW, Picone J, Veenstra R & Rawling D (1983). Propagation through electrically coupled cells. Effects of regional changes in membrane properties. *Circ Res* 53, 526–534.

General Conclusion

“One of the first questions to ask of a model [...] is what questions does it answer best”.

Denis Noble & Yoram Rudy

In their review on models of ventricular action potentials, Noble and Rudy (2001) explained “[...] *the philosophy of modeling as applied to the heart.*”

For each model they asked the following questions:

- 1) What was the purpose of the model? What kind of question was it seeking to answer?*
- 2) What were the gaps? Were there clues in the earlier models to what were to become central questions for later models?*
- 3) How were the models used? What were their successes and failures?*

The above-mentioned questions can be made for each kind of cardiac cell model, and the human SAN model developed in this PhD Dissertation is not an exception.

The overall question that gave birth to this investigation is: *what do simulations tell us about pacemaking in human SAN cells?*

Nowadays mathematical models of SAN are quite comprehensive and able to describe mechanisms at the base of pacemaking in animals, e.g. guinea pigs and rabbits. That is not true for human SAN.

The first gap that has to be faced is the shortage of human-specific electrophysiological data. There are few works that report measurement on adult human SAN relative to AP waveform and Ca^{2+} transient (Verkerk *et al.*, 2007, 2013); furthermore, only few currents as I_f (Verkerk *et al.*, 2007), I_{Kr} and I_{Ks} (Danielsson *et al.*, 2013) were electrophysiologically characterized in human. Thus, the disclosure “of molecular architecture” of human SAN through the quantification of mRNA by Chandler *et al.* (2009) is crucial to add information about the quantity of ion channels present within the membrane.

The development of the human SAN model, therefore, started from the state-of-art rabbit SAN by Severi *et al.* (2012) and the available human specific data were included. Optimization techniques, strongly constraint by experimental data, filled what was missing from wet experiments. The result was the model proposed in **Chapter 1**, able to reproduce the main characteristics of the AP waveform and the Ca^{2+} transient reported in literature.

I_f plays a primary role in pacemaking initiation and modulation in rabbit; the measurement acquired in voltage clamp protocol by (Verkerk *et al.*, 2007) showed that it was way smaller compared to the rabbit one. One on hand, the inclusion of human I_f in the rabbit model suddenly slowed down the rate of the “humanized” model, on the other hand the simulated human I_f and the net current of human model were comparable. As remarkable result, the sensitivity analysis showed that small changes of I_{CaL} , in particular the parameters that control its activation (V_{dL} and k_{dL}) strongly affected the DD, and thus the beating rate, whereas the APD was strongly dependent on I_{Kr} .

Chapter 2 focused on the capability of the major actors of “membrane clock” (I_f) and “ Ca^{2+} clock” (I_{NaCa} and SR) to finely modulate the beating rate; moreover

the autonomic modulation contribution was assessed. I_f achieved an effective control of rate acting exclusively on the slope of DD, without affect any other biomarker. I_{NaCa} , on the contrary, regulated the rate modifying important biomarkers as MDP, AP, APD, DDR. Modulation of SR activity, responsible for the cyclic release of Ca^{2+} , was not able to cause remarkable changes.

Since no experimental data about human on the effects of autonomic stimulation were available, the developed model was used to gain theoretical insights about the biophysical mechanism. Simulation relative to the administration of 10 nM ACh indicated that I_f and $I_{K,ACh}$ are the main players in the beating rate vagal-induced slowdown. The adrenergic stimulation, mimicked through the administration of 1 μ M, highlighted the principal role for I_f and I_{CaL} . The model was also capable to reproduce the physiological range of rate (40 – 180 beats min^{-1}) with an adequate autonomic stimulation.

Ion channel mutations are able to strongly affect the heart rate and they represent a link between electrophysiology and clinical practice. For that reason, they represented a good test-bed to validate the model (**Chapter 3**). Simulations showed a qualitative behavior in agreement with the macroscopic changes of heart rate for HCN4 (9 mutations), SCN5A (6 mutations) and KCNQ1 (3 mutations) reported in clinics. The simulations in presence of autonomic modulation showed that working rate (low,basal,high) is able to change the entity of the effect of the ion channel mutation.

The inclusion of I_{SK} and I_{BK} currents into the human and rabbit SAN models tested how a new current could affect the beating rate (**Chapter 4**). These two currents were selected since they are Ca^{2+} activated, providing clues about how changes in intracellular Ca^{2+} could affect the membrane potential. Intriguingly, even they are mainly outward currents, activated during AP, they can indirectly affect the DD through the involvement of I_{Kr} . The comparison of the effects in the two different models allowed also investigating the model dependence of the effects.

Finally, **Chapter 5** focused on tissue scale level, investigating on electrical propagation of the stimulus originating from SAN in a mono-dimensional strand. The coupling between SAN and atrial cells showed the capability of the SAN model to successfully pace and drive the atrial tissue for an extended range of conductivities. The presence of the hyperpolarized sink (atrial cells) highlighted also the capability of the model to show different AP morphologies, using the same parameters, thanks to the different activation of I_{Na} current. The source-sink interplay was also explored showing a link between pacing robustness and the number of SAN cells that composed the source.

The developed human AP model was able to reproduce experimental data and provided theoretical insights on pacemaking. The experimental conditions on which data were collected constrained important parameters/variables of the models; Verkerk *et al.* (2007) measured SAN AP and characterized I_f with a fixed concentration of intracellular Na^+ (5 nM). This influenced the development of human SAN, which left the dynamical Na^+ balance of the parent model.

Changing extracellular electrolytes concentration also affected the model behavior. Recalling “the failures” indicated by Noble and Rudy, the proposed model stopped its automaticity when the extracellular Ca^{2+} was set to *in vivo* values (i.e. $[Ca^{2+}]_o=1.2$ mM).

The SAN model developed, tested and discussed in this PhD Dissertation represents a tool to investigate pacemaking in human SAN. Even if a part of parameters was updated, the legacy of the rabbit parent model is still present.

Since a limited set of experimental data is available, the carried out simulations can be used as predictions and/or can provide insights that must be tested and verified with experiments in laboratory. Here, the circle between experiments and models can be closed: indeed, models can highlight open question to be addressed with experiments and experiments, in turn, can confirm the predictions or point out inconsistencies/limitations of mathematical models.

It is through the iterative interaction between experiment and simulation that we will gain that understanding”

Denis Noble & Yoram Rudy

References

- Chandler NJ, Greener ID, Tellez JO, Inada S, Musa H, Molenaar P, DiFrancesco D, Baruscotti M, Longhi R, Anderson RH, Billeter R, Sharma V, Sigg DC, Boyett MR & Dobrzynski H (2009). Molecular architecture of the human sinus node insights into the function of the cardiac pacemaker. *Circulation* 119, 1562–1575.
- Danielsson C, Brask J, Sköld A-C, Genead R, Andersson A, Andersson U, Stockling K, Pehrson R, Grinnemo K-H, Salari S, Hellmold H, Danielsson B, Sylvén C & Elinder F (2013). Exploration of human, rat, and rabbit embryonic cardiomyocytes suggests K-channel block as a common teratogenic mechanism. *Cardiovasc Res* 97, 23–32.
- Noble D & Rudy Y (2001). Models of cardiac ventricular action potentials: iterative interaction between experiment and simulation. *Philos Trans R Soc Lond Math Phys Eng Sci* 359, 1127–1142.
- Severi S, Fantini M, Charawi LA & DiFrancesco D (2012). An updated computational model of rabbit sinoatrial action potential to investigate the mechanisms of heart rate modulation. *J Physiol* 590, 4483–4499.
- Verkerk AO, van Borren MMGJ & Wilders R (2013). Calcium transient and sodium-calcium exchange current in human versus rabbit sinoatrial node pacemaker cells. *Sci World J* 2013, e507872.
- Verkerk AO, Wilders R, Borren MMGJ van, Peters RJG, Broekhuis E, Lam K, Coronel R, Bakker JMT de & Tan HL (2007). Pacemaker current (I_f) in the human sinoatrial node. *Eur Heart J* 28, 2472–2478.

Appendix 1: Model Parameters and Equations

MODEL PARAMETERS

Cell compartments

$C = 57$ pF : Cell capacitance

$L_{\text{cell}} = 67$ μm : Cell length

$L_{\text{sub}} = 0.02$ μm : Distance between jSR and surface membrane (submembrane space)

$R_{\text{cell}} = 3.9$ μm : Cell radius

$V_{\text{i part}} = 0.46$: Part of cell volume occupied with myoplasm

$V_{\text{j sr part}} = 0.0012$: Part of cell volume occupied by junctional SR

$V_{\text{nsr part}} = 0.0116$: Part of cell volume occupied by network SR

$V_{\text{cell}} = \pi \cdot R_{\text{cell}}^2 \cdot L_{\text{cell}}$: Cell volume

$V_{\text{sub}} = 2 \cdot \pi \cdot L_{\text{sub}} \cdot \left(R_{\text{cell}} - \frac{L_{\text{sub}}}{2} \right) \cdot L_{\text{cell}}$: Submembrane space volume

$V_{\text{i}} = V_{\text{i part}} \cdot V_{\text{cell}} - V_{\text{sub}}$: Myoplasmic volume

$V_{\text{j sr}} = V_{\text{j sr part}} \cdot V_{\text{cell}}$: Volume of junctional SR (Ca^{2+} release store)

$V_{\text{nsr}} = V_{\text{nsr part}} \cdot V_{\text{cell}}$: Volume of network SR (Ca^{2+} release store)

Fixed ion concentrations, mM

$\text{Ca}_o = 1.8$: Extracellular Ca^{2+} concentration

$\text{K}_i = 140$: Intracellular K^+ concentration

$\text{K}_o = 5.4$: Extracellular K^+ concentration

$\text{Na}_o = 140$: Extracellular Na^+ concentration

$\text{Na}_i = 5$: Intracellular Na^+ concentration

$\text{Mg}_i = 2.5$: Intracellular Mg^{2+} concentration

Variable ion concentrations, mM

C_{ai} : Intracellular Ca^{2+} concentration

C_{ajsr} : Ca^{2+} concentration in the junctional SR

C_{ansr} : Ca^{2+} concentration in the network SR

Ionic values

$F = 96485 \frac{C}{mol}$: Faraday constant

$R = 8314.472 \frac{J}{(kmol K)}$: Universal gas constant

$T = 310 K$: Absolute temperature for 37°C

$RTonF = \frac{R \cdot T}{F} = 26.72655 mV$

$E_{Na} = RTonF \cdot \ln \frac{Na_o}{Na_i}$: Reversal potential for Na^+

$E_{mh} = RTonF \cdot \ln \frac{Na_o + 0.12 \cdot Ko}{Na_i + 0.12 \cdot Ki}$: Reversal potential for fast Na^+ channel

$E_K = RTonF \cdot \ln \frac{Ko}{Ki}$: Reversal potential for K^+

$E_{Ks} = RTonF \cdot \ln \frac{Ko + 0.12 \cdot Na_o}{Ki + 0.12 \cdot Na_i}$ Reversal potential for slow rectifier K^+ channel

$E_{Ca} = 0.5 \cdot RTonF \cdot \ln \frac{Ca_o}{Ca_{sub}}$: Reversal potential for Ca^{2+}

Sarcolemmal ion currents and their conductances

I_f : Hyperpolarization-activated current ($g_{fNa} = 0.00268 \mu S$, $g_{fK} = 0.00159 \mu S$)

I_{CaL} : L-type Ca^{2+} current ($P_{CaL} = 0.4578 \frac{nA}{mM}$)

I_{CaT} : T-type Ca^{2+} current ($P_{CaT} = 0.04132 \frac{nA}{mM}$)

I_{Kr} : Delayed rectifier K^+ current, rapid component ($g_{Kr} = 0.00424 \mu S$)

I_{Ks} : Delayed rectifier K^+ current, slow component ($g_{Ks} = 0.00065 \mu S$)

I_{KACh} : ACh-activated K^+ current ($g_{KACh} = 0.00345 \mu S$)

I_{to} : Transient outward K^+ current ($g_{to} = 3.5 \cdot 10^{-3} \mu S$)

I_{Na} : Fast Na^+ current ($g_{Na} = 0.0223\mu S$)

I_{NaK} : Na^+/K^+ pump current ($i_{NaK_{max}} = 0.08105$ nA)

I_{NaCa} : Na^+/Ca^{2+} exchanger current ($K_{NaCa} = 3.343$ nA)

Modulation of sarcolemmal ion currents by ions

$Km_{fCa} = 0.000338$ mM : Dissociation constant of Ca^{2+} -dependent I_{CaL}
inactivation

$Km_{Kp} = 1.4$ mM : Half-maximal K_o for I_{NaK}

$Km_{Nap} = 14$ mM : Half-maximal Na_i for I_{NaK}

$\alpha_{fCa} = 0.0075$ s⁻¹ : Ca^{2+} dissociation rate constant for I_{CaL}

Na^+/Ca^{2+} exchanger (NaCa) function

$K1ni = 395.3$ mM: Intracellular Na^+ binding to first site on NaCa

$K1no = 1628$ mM: Extracellular Na^+ binding to first site on NaCa

$K2ni = 2.289$ mM: Intracellular Na^+ binding to second site on NaCa

$K2no = 561.4$ mM: Extracellular Na^+ binding to second site on NaCa

$K3ni = 26.44$ mM : Intracellular Na^+ binding to third site on NaCa

$K3no = 4.663$ mM: Extracellular Na^+ binding to third site on NaCa

$Kci = 0.0207$ mM : Intracellular Ca^{2+} binding to NaCa transporter

$Kcni = 26.44$ mM : Intracellular Na^+ and Ca^{2+} simultaneous binding to NaCa

$Kco = 3.663$ mM: Extracellular Ca^{2+} binding to NaCa transporter

$Qci = 0.1369$: Intracellular Ca^{2+} occlusion reaction of NaCa

$Qco = 0$: Extracellular Ca^{2+} occlusion reaction of NaCa

$Qn = 0.4315$: Na^+ occlusion reaction of NaCa

Ca^{2+} diffusion

$\tau_{difCa} = 5.469 \cdot 10^{-5}$ s : Time constant of Ca^{2+} diffusion from the subsarcolemmal space to the myoplasm

$\tau_{tr} = 0.04$ s : Time constant of Ca^{2+} transfer from the network to junctional SR

SERCA pump

$K_{up} = 286 \text{ nM}$: Half-maximal Ca_i for Ca^{2+} uptake into the network SR

$P_{up} = 5 \frac{\text{mM}}{\text{s}}$: Rate constant for Ca^{2+} uptake by SERCA pump into the network SR

$\text{slope}_{up} = 50 \text{ nM}$: slope factor for Ca^{2+} uptake by SERCA pump into the network SR

RyR function

$kiCa = 500 \frac{1}{\text{mM s}}$: RyR Ca-dependent inactivation rate

$kim = 5 \text{ s}^{-1}$: RyR repriming rate

$koCa = 10000 \frac{1}{\text{mM}^2 \text{ s}}$: RyR Ca-activation rate

$kom = 660 \text{ s}^{-1}$: RyR deactivation rate

$ks = 1.48 \cdot 10^8 \text{ s}^{-1}$: Ca^{2+} diffusion rate

$EC50_{SR} = 0.45 \text{ mM}$: EC50 for Ca_{jSR} -dependent activation of SR Ca release

$HSR = 2.5$: Hill coefficient for Ca_{jSR} -dependent activation of SR calcium release

$MaxSR = 15$: parameter for maximum SR Ca^{2+} release

$MinSR = 1$: parameter for minimum SR Ca^{2+} release

Ca^{2+} and Mg^{2+} buffering

$CM_{tot} = 0.045 \text{ mM}$: Total calmodulin concentration

$CQ_{tot} = 10 \text{ mM}$: Total calsequestrin concentration

$TC_{tot} = 0.031 \text{ mM}$: Total concentration of the troponin- Ca^{2+} site

$TMC_{tot} = 0.062 \text{ mM}$: Total concentration of the troponin- Mg^{2+} site

$kb_{CM} = 542 \text{ s}^{-1}$: Ca^{2+} dissociation constant for calmodulin

$kb_{CQ} = 445 \text{ s}^{-1}$: Ca^{2+} dissociation constant for calsequestrin

$kb_{TC} = 446 \text{ s}^{-1}$: Ca^{2+} dissociation constant for the troponin- Ca^{2+} site

$kb_{TMC} = 7.51 \text{ s}^{-1}$: Ca^{2+} dissociation constant for the troponin- Mg^{2+} site

$kb_{TMM} = 751 \text{ s}^{-1}$: Mg^{2+} dissociation constant for the troponin- Mg^{2+} site

$kf_{CM} = 1.64 \cdot 10^6 \frac{1}{\text{mM s}}$: Ca^{2+} association constant for calmodulin

$kf_{CQ} = 175 \frac{1}{\text{mM s}}$: Ca^{2+} association constant for calsequestrin

$kf_{TC} = 88800 \frac{1}{\text{mM s}}$: Ca^{2+} association constant for the troponin- Ca^{2+} site

$kf_{TMC} = 227700 \frac{1}{\text{mM s}}$: Ca^{2+} association constant for the troponin- Mg^{2+} site

$kf_{TMM} = 2277 \frac{1}{\text{mM s}}$: Mg^{2+} association constant for the troponin- Mg^{2+} site

MODEL EQUATIONS

Membrane potential

$$\frac{dV}{\text{dtime}} = \frac{-I_{\text{tot}}}{C}$$

$$I_{\text{tot}} = I_f + I_{\text{CaL}} + I_{\text{CaT}} + I_{\text{Kr}} + I_{\text{Ks}} + I_{\text{KACh}} + I_{\text{to}} + I_{\text{Na}} + I_{\text{NaK}} + I_{\text{NaCa}} + I_{\text{Kur}}$$

Ion currents

x_{∞} : steady-state for gating variable x

τ_x : time constant for gating variable x (s)

α_x and β_x : opening and closing rates for channel gate x (s^{-1})

Hyperpolarization-activated, “funny current” (I_f)

$$I_f = i_{f\text{Na}} + i_{f\text{K}}$$

$$I_{f\text{Na}} = y \cdot g_{f\text{Na}} \cdot (V - E_{\text{Na}})$$

$$I_{f\text{K}} = y \cdot g_{f\text{K}} \cdot (V - E_{\text{K}})$$

$$y_{\infty} = \begin{cases} 0.01329 + \frac{0.99921}{1 + e^{\frac{V+97.134}{8.1752}}}, & \text{if } V < -80 \\ 0.0002501 \cdot e^{\frac{-V}{12.861}}, & \text{otherwise} \end{cases}$$

$$\tau_y = \frac{1}{\frac{0.36 \cdot (V + 148.8)}{e^{0.066 \cdot (V+148.8)} - 1} + \frac{0.1 \cdot (V + 87.3)}{1 - e^{-0.2 \cdot (V+87.3)}}} - 0.054$$

$$\frac{dy}{dtime} = \frac{y_\infty - y}{\tau_y}$$

L-type Ca²⁺ current (I_{CaL})

$$I_{CaL} = I_{siCa} + I_{siK} + I_{siNa}$$

$$I_{siCa} = \frac{2 \cdot P_{CaL} \cdot V}{RTONF \cdot \left(1 - e^{\frac{-2V}{RTONF}}\right)} \cdot \left(Ca_{sub} - Ca_o \cdot e^{\frac{-2V}{RTONF}}\right) \cdot dL \cdot fL \cdot fCa$$

$$I_{siK} = \frac{0.000365 \cdot P_{CaL} \cdot V}{RTONF \cdot \left(1 - e^{\frac{-V}{RTONF}}\right)} \cdot \left(Ki - Ko \cdot e^{\frac{-V}{RTONF}}\right) \cdot dL \cdot fL \cdot fCa$$

$$I_{siNa} = \frac{0.0000185 \cdot P_{CaL} \cdot V}{RTONF \cdot \left(1 - e^{\frac{-V}{RTONF}}\right)} \cdot \left(Nai - Nao \cdot e^{\frac{-V}{RTONF}}\right) \cdot dL \cdot fL \cdot fCa$$

$$dL_\infty = \frac{1}{1 + e^{\frac{-(V+16.45)}{4.32}}}$$

$$\alpha_{dL} = \frac{-0.02839 \cdot (V + 41.8)}{e^{\frac{-(V+41.8)}{2.5}} - 1} - \frac{0.0849 \cdot (V + 6.8)}{e^{\frac{-(V+6.8)}{4.8}} - 1}$$

$$\beta_{dL} = \frac{0.01143 \cdot (V + 1.8)}{e^{\frac{V+1.8}{2.5}} - 1}$$

$$\tau_{dL} = \frac{0.001}{\alpha_{dL} + \beta_{dL}}$$

$$\frac{ddL}{dtime} = \frac{dL_{\infty} - dL}{\tau_{dL}}$$

$$fCa_{\infty} = \frac{Km_{fCa}}{Km_{fCa} + Ca_{sub}}$$

$$\tau_{fCa} = \frac{0.001 \cdot fCa_{\infty}}{\alpha_{fCa}}$$

$$\frac{dfCa}{dtime} = \frac{fCa_{\infty} - fCa}{\tau_{fCa}}$$

$$fL_{\infty} = \frac{1}{1 + e^{\frac{V+37.4+shift_{fL}}{5.3+k_{fL}}}}$$

$$\tau_{fL} = 0.001 \cdot \left(44.3 + 230 \cdot e^{-\left(\frac{V+36}{10}\right)^2} \right)$$

$$\frac{dfL}{dtime} = \frac{fL_{\infty} - fL}{\tau_{fL}}$$

T-type Ca²⁺ current (I_{CaT})

$$I_{CaT} = \frac{2 \cdot P_{CaT} \cdot V}{RTONF \cdot \left(1 - e^{\frac{-2 \cdot V}{RTONF}}\right)} \cdot \left(Ca_{sub} - Ca_0 \cdot e^{\frac{-2 \cdot V}{RTONF}} \right) \cdot dT \cdot fT$$

$$dT_{\infty} = \frac{1}{1 + e^{\frac{-(V+38.3)}{5.5}}}$$

$$\tau_{dT} = \frac{0.001}{1.068 \cdot e^{\frac{V+38.3}{30}} + 1.068 \cdot e^{\frac{-(V+38.3)}{30}}}$$

$$\frac{ddT}{dtime} = \frac{dT_{\infty} - dT}{\tau_{dT}}$$

$$fT_{\infty} = \frac{1}{1 + e^{\frac{V+58.7}{3.8}}}$$

$$\tau_{fT} = \frac{1}{16.67 \cdot e^{\frac{-(V+75)}{83.3}} + 16.67 \cdot e^{\frac{V+75}{15.38}}}$$

$$\frac{dfT}{dtime} = \frac{fT_{\infty} - fT}{\tau_{fT}}$$

Rapidly activating delayed rectifier K⁺ current (I_{Kr})

$$I_{Kr} = g_{Kr} \cdot (V - E_K) \cdot (0.9 \cdot paF + 0.1 \cdot paS) \cdot piy$$

$$paF_{\infty} = paS_{\infty} = pa_{\infty} = \frac{1}{1 + e^{\frac{-(V+10.0144)}{7.6607}}}$$

$$\tau_{paS} = \frac{0.84655354}{4.2 \cdot e^{\frac{V}{17}} + 0.15 \cdot e^{\frac{-V}{21.6}}}$$

$$\tau_{paF} = \frac{1}{30 \cdot e^{\frac{V}{10}} + e^{\frac{-V}{12}}}$$

$$\frac{dpaS}{dtime} = \frac{pa_{\infty} - paS}{\tau_{paS}}$$

$$\frac{dpaF}{dtime} = \frac{pa_{\infty} - paF}{\tau_{paF}}$$

$$\tau_{piy} = \frac{1}{100 \cdot e^{\frac{-V}{54.645}} + 656 \cdot e^{\frac{V}{106.157}}}$$

$$p_{iy\infty} = \frac{1}{1 + e^{\frac{V+28.6}{17.1}}}$$

$$\frac{dp_{iy}}{dtime} = \frac{p_{iy\infty} - p_{iy}}{\tau_{p_{iy}}}$$

Slowly activating delayed rectifier K^+ current (I_{Ks})

$$I_{Ks} = g_{Ks} \cdot (V - E_{Ks}) \cdot n^2$$

$$n_{\infty} = \sqrt{\frac{1}{1 + e^{\frac{-(V+0.6383)}{10.7071}}}}$$

$$\tau_n = \frac{1}{\alpha_n + \beta_n}$$

$$\alpha_n = \frac{28}{1 + e^{\frac{-(V-40)}{3}}}$$

$$\beta_n = 1 \cdot e^{\frac{-(V-5)}{25}}$$

$$\frac{dn}{dtime} = \frac{n_{\infty} - n}{\tau_n}$$

ACh-activated K^+ current ($I_{K,ACh}$)

$$I_{K,ACh} = \begin{cases} g_{K,ACh} \cdot (V - E_K) \cdot \left(1 + e^{\frac{V+20}{20}}\right) \cdot a, & \text{if } ACh > 0 \\ 0, & \text{otherwise} \end{cases}$$

$$\alpha_a = \frac{3.5988 - 0.025641}{1 + \frac{0.0000012155}{(\text{ACh})^{1.6951}}} + 0.025641$$

$$\beta_a = 10 \cdot e^{0.0133 \cdot (V+40)}$$

$$a_\infty = \frac{\alpha_a}{\alpha_a + \beta_a}$$

$$\tau_a = \frac{1}{\alpha_a + \beta_a}$$

$$\frac{da}{d\text{time}} = \frac{a_\infty - a}{\tau_a}$$

Transient outward K⁺ current (I_{to})

$$I_{to} = g_{to} \cdot (V - E_K) \cdot q \cdot r$$

$$q_\infty = \frac{1}{1 + e^{\frac{V+49}{13}}}$$

$$\tau_q = 0.001 \cdot 0.6 \cdot \left(\frac{65.17}{0.57 \cdot e^{-0.08 \cdot (V+44)} + 0.065 \cdot e^{0.1 \cdot (V+45.93)}} + 10.1 \right)$$

$$\frac{dq}{d\text{time}} = \frac{q_\infty - q}{\tau_q}$$

$$r_\infty = \frac{1}{1 + e^{\frac{-(V-19.3)}{15}}}$$

$$\tau_r = 0.001 \cdot 0.66 \cdot 1.4 \cdot \left(\frac{15.59}{1.037 \cdot e^{0.09 \cdot (V+30.61)} + 0.369 \cdot e^{-0.12 \cdot (V+23.84)}} + 2.98 \right)$$

$$\frac{dr}{d\text{time}} = \frac{r_\infty - r}{\tau_r}$$

Na⁺ current (I_{Na})

$$I_{\text{Na}} = g_{\text{Na}} \cdot m^3 \cdot h \cdot (V - E_{\text{mh}})$$

$$m_{\infty} = \frac{1}{1 + e^{\frac{-(V+42.0504)}{8.3106}}}$$

$$E0_m = V + 41$$

$$\alpha_m = \frac{200 \cdot E0_m}{1 - e^{-0.1 \cdot E0_m}}$$

$$\beta_m = 8000 \cdot e^{-0.056 \cdot (V+66)}$$

$$\tau_m = \frac{1}{\alpha_m + \beta_m}$$

$$\frac{dm}{dtime} = \frac{m_{\infty} - m}{\tau_m}$$

$$h_{\infty} = \frac{1}{1 + e^{\frac{V+69.804}{4.4565}}}$$

$$\alpha_h = 20 \cdot e^{-0.125 \cdot (V+75)}$$

$$\beta_h = \frac{2000}{320e^{-0.1(V+75)} + 1}$$

$$\tau_h = \frac{1}{\alpha_h + \beta_h}$$

$$\frac{dh}{dtime} = \frac{h_{\infty} - h}{\tau_h}$$

Na⁺/K⁺ pump current (I_{NaK})

$$I_{\text{NaK}} = I_{\text{NaKmax}} \cdot \left(1 + \left(\frac{K_{mKp}}{K_o}\right)^{1.2}\right)^{-1} \cdot \left(1 + \left(\frac{K_{mNap}}{N_{ai}}\right)^{1.3}\right)^{-1} \cdot \left(1 + e^{\frac{-(V-E_{Na}+110)}{20}}\right)^{-1}$$

Na⁺/Ca²⁺ exchanger current (I_{NaCa})

$$I_{\text{NaCa}} = \frac{K_{\text{NaCa}} \cdot (x_2 \cdot k_{21} - x_1 \cdot k_{12})}{x_1 + x_2 + x_3 + x_4}$$

$$x_1 = k_{41} \cdot k_{34} \cdot (k_{23} + k_{21}) + k_{21} \cdot k_{32} \cdot (k_{43} + k_{41})$$

$$x_2 = k_{32} \cdot k_{43} \cdot (k_{14} + k_{12}) + k_{41} \cdot k_{12} \cdot (k_{34} + k_{32})$$

$$x_3 = k_{14} \cdot k_{43} \cdot (k_{23} + k_{21}) + k_{12} \cdot k_{23} \cdot (k_{43} + k_{41})$$

$$x_4 = k_{23} \cdot k_{34} \cdot (k_{14} + k_{12}) + k_{14} \cdot k_{21} \cdot (k_{34} + k_{32})$$

$$k_{43} = \frac{N_{ai}}{K_{3ni} + N_{ai}}$$

$$k_{12} = \frac{\frac{Ca_{\text{sub}}}{K_{ci}} \cdot e^{\frac{-Q_{ci} \cdot V}{RTONF}}}{d_i}$$

$$k_{14} = \frac{\frac{N_{ai}}{K_{1ni}} \cdot N_{ai}}{K_{2ni}} \cdot \left(1 + \frac{N_{ai}}{K_{3ni}}\right) \cdot e^{\frac{Q_n \cdot V}{2 \cdot RTONF}}}{d_i}$$

$$k_{41} = e^{\frac{-Q_n \cdot V}{2 \cdot RTONF}}$$

$$d_i = 1 + \frac{C_{a_{sub}}}{K_{ci}} \cdot \left(1 + e^{\frac{-Q_{ci} \cdot V}{RTONF}} + \frac{N_{ai}}{K_{cni}} \right) + \frac{N_{ai}}{K_{1ni}} \cdot \left(1 + \frac{N_{ai}}{K_{2ni}} \cdot \left(1 + \frac{N_{ai}}{K_{3ni}} \right) \right)$$

$$k_{34} = \frac{N_{ao}}{K_{3no} + N_{ao}}$$

$$k_{21} = \frac{\frac{C_{ao}}{K_{co}} \cdot e^{\frac{Q_{co} \cdot V}{RTONF}}}{d_o}$$

$$k_{23} = \frac{\frac{\frac{N_{ao}}{K_{1no}} \cdot N_{ao}}{K_{2no}} \cdot \left(1 + \frac{N_{ao}}{K_{3no}} \right) \cdot e^{\frac{-Q_n \cdot V}{2 \cdot RTONF}}}{d_o}$$

$$k_{32} = e^{\frac{Q_n \cdot V}{2 \cdot RTONF}}$$

$$d_o = 1 + \frac{C_{ao}}{K_{co}} \cdot \left(1 + e^{\frac{Q_{co} \cdot V}{RTONF}} \right) + \frac{N_{ao}}{K_{1no}} \cdot \left(1 + \frac{N_{ao}}{K_{2no}} \cdot \left(1 + \frac{N_{ao}}{K_{3no}} \right) \right)$$

Ultra-rapid activating delayed rectifier K^+ current (I_{Kur})

$$I_{Kur} = g_{Kur} \cdot r_{Kur} \cdot s_{Kur} \cdot (V - E_K)$$

$$\frac{dr_{Kur}}{dt_{ime}} = \frac{r_{Kur\infty} - r_{Kur}}{\tau_{r_{Kur}}}$$

$$r_{Kur\infty} = \frac{1}{1 + e^{-8.6 \frac{V+6}{V+6}}}$$

$$\tau_{r_{Kur}} = \frac{0.009}{1 + e^{\frac{V+5}{12}}} + 0.0005$$

$$\frac{ds_{Kur}}{dt_{ime}} = \frac{s_{Kur\infty} - s_{Kur}}{\tau_{s_{Kur}}}$$

$$S_{Kur\infty} = \frac{1}{1 + e^{-\frac{V+7.5}{10}}}$$

$$\tau_{s_{Kur}} = \frac{0.59}{1 + e^{-\frac{V+60}{10}}} + 3.05$$

Ca²⁺ release flux (J_{rel}) from SR via RyRs

$$J_{SRCarel} = k_s \cdot O \cdot (Ca_{j_{sr}} - Ca_{sub})$$

$$diff = Ca_{j_{sr}} - Ca_{sub}$$

$$kCaSR = MaxSR \cdot \frac{MaxSR - MinSR}{1 + \left(\frac{EC50_{SR}}{Ca_{j_{sr}}}\right)^{HSR}}$$

$$koSRCa = \frac{koCa}{kCaSR}$$

$$kiSRCa = kiCa \cdot kCaSR$$

$$\frac{dR}{dtime} = kim \cdot RI - kiSRCa \cdot Ca_{sub} \cdot R - (koSRCa \cdot Ca_{sub}^2 \cdot R - kom \cdot O)$$

$$\frac{dO}{dtime} = koSRCa \cdot Ca_{sub}^2 \cdot R - kom \cdot O - (kiSRCa \cdot Ca_{sub} \cdot O - kim \cdot I)$$

$$\frac{dI}{dtime} = kiSRCa \cdot Ca_{sub} \cdot O - kim \cdot I - (kom \cdot I - koSRCa \cdot Ca_{sub}^2 \cdot RI)$$

$$\frac{dRI}{dtime} = kom \cdot I - koSRCa \cdot Ca_{sub}^2 \cdot RI - (kim \cdot RI - kiSRCa \cdot Ca_{sub} \cdot R)$$

$$P_{tot} = R + O + I + RI$$

Intracellular Ca²⁺ fluxes

$J_{Ca_{dif}}$: Ca²⁺ diffusion flux from submembrane space to myoplasm

J_{up} : Ca²⁺ uptake by the SR

J_{tr} : Ca²⁺ diffusion flux from the network to junctional SR

$$J_{Ca_{dif}} = \frac{Ca_{sub} - Cai}{\tau_{difCa}}$$

$$J_{up} = \frac{P_{up}}{1 + e^{\frac{-Cai + K_{up}}{slope_{up}}}}$$

$$J_{tr} = \frac{Ca_{nsr} - Ca_{jsr}}{\tau_{tr}}$$

Ca²⁺ buffering

f_{CMi} : Fractional occupancy of calmodulin by Ca²⁺ in myoplasm

f_{CMS} : Fractional occupancy of calmodulin by Ca²⁺ in subspace

f_{CQ} : Fractional occupancy of calsequestrin by Ca²⁺

f_{TC} : Fractional occupancy of the troponin-Ca²⁺ site by Ca²⁺

f_{TMC} : Fractional occupancy of the troponin-Mg²⁺ site by Ca²⁺

f_{TMM} : Fractional occupancy of the troponin-Mg²⁺ site by Mg²⁺

$$\frac{df_{TC}}{dtime} = \delta_{f_{TC}}$$

$$\delta_{f_{TC}} = kf_{TC} \cdot Cai \cdot (1 - f_{TC}) - kb_{TC} \cdot f_{TC}$$

$$\frac{df_{TMC}}{dtime} = \delta_{f_{TMC}}$$

$$\delta_{f_{TMC}} = kf_{TMC} \cdot Cai \cdot (1 - (f_{TMC} + f_{TMM})) - kb_{TMC} \cdot f_{TMC}$$

$$\frac{df_{TMM}}{dtime} = \delta_{f_{TMM}}$$

$$\delta_{f_{TMM}} = kf_{TMM} \cdot Mgi \cdot (1 - (f_{TMC} + f_{TMM})) - kb_{TMM} \cdot f_{TMM}$$

$$\frac{df_{CMi}}{dtime} = \delta_{f_{CMi}}$$

$$\delta_{f_{CMi}} = kf_{CM} \cdot Cai \cdot (1 - f_{CMi}) - kb_{CM} \cdot f_{CMi}$$

$$\frac{df_{CMs}}{dtime} = \delta_{f_{CMs}}$$

$$\delta_{f_{CMs}} = kf_{CM} \cdot Ca_{sub} \cdot (1 - f_{CMs}) - kb_{CM} \cdot f_{CMs}$$

$$\frac{df_{CQ}}{dtime} = \delta_{f_{CQ}}$$

$$\delta_{f_{CQ}} = kf_{CQ} \cdot Ca_{jsr} \cdot (1 - f_{CQ}) - kb_{CQ} \cdot f_{CQ}$$

Dynamics of Ca^{2+} concentrations in cell compartments

$$\frac{dCai}{dtime} = \frac{1 \cdot (J_{Cadif} \cdot V_{sub} - J_{up} \cdot V_{nsr})}{V_i} - (CM_{tot} \cdot \delta_{f_{CMi}} + TC_{tot} \cdot \delta_{f_{TC}} + TMC_{tot} \cdot \delta_{f_{TMC}})$$

$$\frac{dCa_{sub}}{dtime} = \frac{J_{SRCarel} \cdot V_{jsr}}{V_{sub}} - \left(\frac{i_{siCa} + i_{CaT} - 2 \cdot i_{NaCa}}{2 \cdot F \cdot V_{sub}} + j_{Ca_{dif}} + CM_{tot} \cdot \delta_{fCMs} \right)$$

$$\frac{dCa_{nsr}}{dtime} = J_{up} - \frac{J_{tr} \cdot V_{jsr}}{V_{nsr}}$$

$$\frac{dCa_{jsr}}{dtime} = J_{tr} - (J_{SRCarel} + CQ_{tot} \cdot \delta_{fCQ})$$

Rate Modulation Experiments

Acetylcholine 10 nM

I_f : shift of y_∞ and τ_y by -5 mV.

I_{CaL} : reduction of the maximal conductance by 3%.

SERCA pump: decrease of P_{up} by 7%.

I_{KACh} activation.

Isoprenaline 1 μ M

I_f : shift of y_∞ and τ_y by 7.5 mV.

I_{NaK} : increase of $I_{NaK,max}$ by 20%.

I_{CaL} : increase of the maximal conductance by 23%; shift of dL_∞ and τ_{dL} by -8 mV reduction of the slope factor k_{dL} by 27%.

I_{Ks} : increase of g_{Ks} by 20%; shift of n_∞ and τ_n by -14 mV.

SERCA pump: increase of P_{up} by 25

Appendix 2: automatic optimization procedure

Parameters selected for automatic optimization

g_{Kur} = maximal conductance of I_{Kur}

K_{NaCa} = maximal current of NCX

K_{up} = Ca^{2+} concentration for half-maximal activity of SERCA pump

P_{CaT} = permeability of T-type Ca^{2+} current

P_{CaL} = permeability of L-type Ca^{2+} current

k_{dL} = slope factor of L-type voltage-dependent activation gate dL

V_{dL} = half maximal activation voltage of voltage-dependent activation gate dL

τ_{difCa} = time constant of Ca^{2+} diffusion from the submembrane to myoplasm

k_s = maximal rate of calcium release from RyR channels

$k_{f,CM}$ = Ca^{2+} association constant for calmodulin

$k_{f,CQ}$ = Ca^{2+} association constant for calsequestrin

$I_{NaK,max}$ = maximal Na^+/K^+ pump current

Action potential features used to constrain model parameters

Experimental data on APA, MDP, CL, V_{max} , APD₂₀, APD₅₀, APD₉₀, DDR₁₀₀, and CL prolongation induced by Cs^+ of single isolated human SAN cells as reported by Verkerk *et al.* (2007) were used to constrain model parameters. Data on CL prolongation induced by Cs^+ are from only one cell. We arbitrarily adopted an SEM of 10% of the experimentally observed CL prolongation.

Calcium transient features used to constrain model parameters

Experimental data on diastolic $[Ca^{2+}]$, systolic $[Ca^{2+}]$, TD₂₀, TD₅₀, and TD₉₀ of a single isolated human SAN cell as reported by Verkerk *et al.* (2013) were used to constrain model parameters.

Because the experimental data on the calcium transient are from only one cell, we arbitrarily set the SEM of each of the calcium transient features to 40% in our optimization procedure.

Cost function

In our optimization procedure, we minimized the overall cost function $FCost$, which was defined as

$$FCost = \sum_i Cost_i$$

in which $Cost_i$ denotes the individual contribution of feature i to the overall cost.

$Cost_i$ is described as follows (Figure A1):

$$\left\{ \begin{array}{l} Cost_i = \frac{|Feature_{i,Exp} - Feature_{i,Sim}| - SEM_i}{SEM_i} weight_i \quad \text{if } |Feature_{i,Exp} - Feature_{i,Sim}| > SEM \\ 0 \quad \text{otherwise} \end{array} \right.$$

We set $weight_i = 2$ for MDP, CL, and CL prolongation induced by Cs^+ , whereas $weight_i$ was set to 1 for all other features.

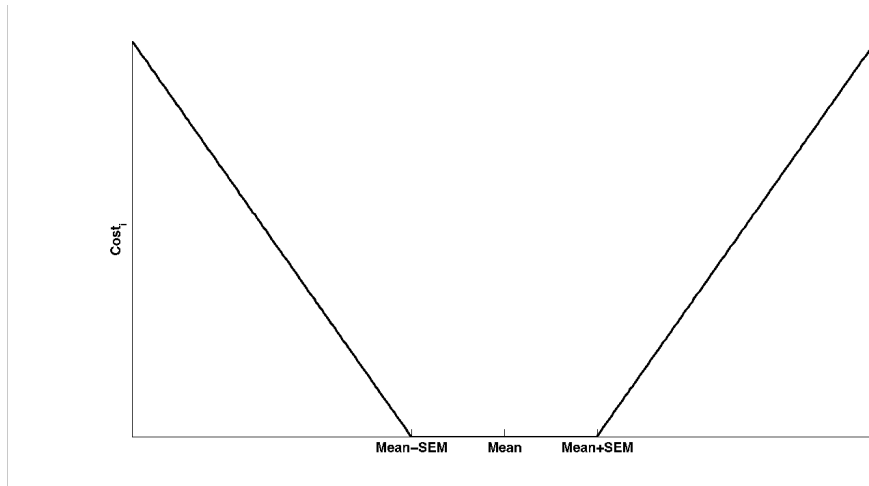


Figure A1. Contribution $Cost_i$ of feature i to the overall cost function (FCost).

Search method and stop criterion

The initial values of the selected parameters were obtained starting from the parent (rabbit) model through a manual tuning in order to achieve a beating rate and action potential morphology close to the experimental human data. Such initial values were then employed to perform the above-mentioned finer automatic optimization.

The minimization of the overall cost function $FCost$ was based on the Nelder-Mead simplex method (Lagarias *et al.*, 1998). The automatic optimization procedure stopped upon convergence of $FCost$ to a local minimum.

Parameter constraining

In order to determine if the parameters are well constrained we followed the approach by Sarkar & Sobie (2010). In this work the authors exploited the extended Bayes theorem in order to define a range for parameters, for which a population of models is able to reproduce behaviour in agreement with experimental data. The parameter constraining is performed increasing the number of the features to satisfy: the higher is the number of the selected features, the lower is the number of compatible set of parameters. In a similar way, we selected MDP, CL, APD₉₀ and DDR₁₀₀, among the available 13 extracted features, to be within the target range (i.e. mean \pm SEM of experimental values) and obtained the ranges in Table A1.

Table A1: Nominal values and ranges for the optimized parameters

Parameters	Units	Nominal	Range (min-max)
g_{Kur}	μS	$1.539 \cdot 10^{-4}$	$0.9895 - 1.633 \cdot 10^{-4}$
P_{CaT}	nA/mM	0.04132	0.04132 - 0.05191
P_{CaL}	nA/mM	0.4578	0.3475 - 0.5262
V_{dL}	mV	-16.45	-20.97 - -13.73
k_{dL}	mV	4.337	3.892 - 4.401
$I_{NaK,max}$	nA	0.08105	0.0623 - 0.1063
K_{NaCa}	nA	3.343	2.733 - 4.964
K_{up}	nM	286.1	204.6 - 356.2
k_s	s^{-1}	$1.480 \cdot 10^8$	$1.460 - 1.847 \cdot 10^8$
τ_{difCa}	s	$5.469 \cdot 10^{-5}$	$5.469 - 7.951 \cdot 10^{-5}$
k_{fCM}	mM/s	$1.642 \cdot 10^6$	$1.164 - 1.839 \cdot 10^6$
k_{fCQ}	mM/s	175.4	155.2 - 194.6

The collected values show an adequately constrained range for the optimized parameters. To achieve this result, we exploited *a priori* knowledge during the optimization procedure, e.g. we avoided unphysiological values (negative conductances or values too far from data reported in literature) assigning high scores to their cost function.

The achievement of more than one parameter set that falls into experimental ranges could suggest the robustness of the model, which is able to adequately compensate parameter changes, without adopting parameters far from the physiological range.

Ringraziamenti

Se da bambino mi aveste chiesto “cosa vuoi fare da grande?”, vi avrei risposto che avrei voluto comprare una Ferrari e fare l’astronauta oppure lo scienziato... Beh, oggi, nel 2018, ho una Citroen C4 del 2005, che non uso perché è in Italia, e una bicicletta di seconda mano che ho comprato qualche mese fa in un negozio ad Utrecht. Ah, non sono nemmeno diventato un astronauta, ma alla fine di questo cammino lungo tre anni e un po’, sono diventato qualcosa di simile ad uno scienziato, e dico simile perché ho ancora tanto da imparare.

Quelli del dottorato, sono stati anni memorabili, che hanno lasciato il segno: la valigia diventa un’estensione del tuo corpo, perché non vedi l’ora di andare a qualche congresso in giro per il mondo; incontri tanti ragazzi che vengono da parti diverse del mondo con la tua stessa passione; poi, almeno per me è stato così, inizi a capire che stai diventando davvero adulto e che i conti a fine mese devono tornare.

Questi anni sono stati memorabili anche per le persone che ho incontrato e a cui sono grato.

Un grazie di cuore va a Stefano Severi, “il Prof” che in questi anni è stato la mia guida e che è sempre stato disponibile per discutere di quello che stavo facendo, dando indicazioni preziose.

Nel giugno del 2015, ad un congresso, ho avuto il piacere di conoscere di persona Ronald Wilders. Ronald è sempre stato un riferimento importante durante tutto il mio percorso di dottorato e mi auguro che continuerà ad esserlo anche in futuro.

Grazie ad Arie Verkerk che, assieme a Ronald, mi ha ospitato nel suo laboratorio di elettrofisiologia cardiaca all’AMC di Amsterdam e che mi ha fatto vedere dal vivo quello che sino ad allora avevo solo letto su libri o articoli.

Grazie alle persone del mio nuovo dipartimento, Medical Physiology dell’UMC di Utrecht. A Teun DeBoer, Mark Vos e Marcel van der Heyden che hanno avuto fiducia in me e che mi hanno permesso di conciliare l’avventura che ho appena iniziato con quella che sto concludendo. Grazie ad Alex e ad Elise, i miei compagni di ufficio, ai dottorandi e agli studenti, che rendono più piacevole il tempo trascorso a lavoro.

Quando diventi un dottorando, anche se sei “tecnicamente” ancora uno studente, senti in qualche modo che sei passato dall’“altra parte della barricata”. Lo senti

perché quelli che fino a poco prima ti facevano lezione o seminari diventano persone con cui collabori e con cui ti confronti. Queste persone per me sono Michelangelo, Claudia, Chiara, Enrico ed Elisa. Grazie per le cose che ho imparato e che spero di continuare ad imparare da voi.

Axel, collaborare con te è stato un piacere, spero di avere occasione di farlo anche in futuro. Yannick, sono contento ci sia stata l'occasione di conoscerti! Grazie per la tua super-ospitalità a Karlsruhe nonostante fossi in un periodo super impegnato!

Madda, Jo, Paola, noi siamo i 4 dell'Ave Maria! Insieme abbiamo iniziato questa avventura e ormai siamo prossimi al traguardo. Senza di voi le giornate in via Cavalcavia sarebbero state più dure. Con questo però non voglio fare torto a Claudio, che per le sue "super battute" ha intitolato pure un premio che ogni giorno ci contendiamo in pausa pranzo.

Valeria, Giulia anche voi siete diventate un pezzo di via Cavalcavia e conoscervi giorno dopo giorno mi ha fatto piacere.

Simone, sei arrivato in ufficio come tesista e ne sei uscito come amico! Assieme abbiamo condiviso il fardello simultaneo di scrivere la tesi e ci siamo divertiti durante partite di calcetto!

Danilo, Simone Moretti, Alex, Paglio, Bob, Ahmed, Chiara ed Andrea, "quelli di Apice", Marilisa, Cresc, Cinzia, Giulia, Michele, "gli elettronici". Senza di voi la pausa pranzo non è la stessa cosa. Ogni giorno si parla di discorsi semiseri, ovviamente nerd, e si prova a strappare a Claudio il "premio Claudio" per la peggior battuta, di cui ogni giorno parte detentore per diritto.

Cri, Sara voi siete un punto di riferimento per me ed è bello ascoltare sia i vostri discorsi sull'università sia su quello che sta fuori.

Maurizio, il guardiano del LIB, grazie per il supporto che mi hai dato e per i discorsi sulla formula 1!

Grazie a Sonia, Roberto, Alex e Marina per tutti i pacchi che avete ritirato per me e per la gentilezza che avete sempre avuto!

Alice, sei una persona in cui ripongo la mia stima e la mia fiducia, sei un'amica. Mi hai visto in giorni no, in giorni in cui mi ero perso; mi hai sempre dato la tua opinione e non semplicemente quello che mi volevo sentire dire. Per questo te ne sarò sempre grato!

Mamma, Babbo, grazie! Mi avete visto crescere, molto spesso seduto davanti ad una scrivania. Studiare richiede impegno e dedizione e lo avete sempre capito. Grazie per avermi sempre sostenuto.

Luca, “Bro”, grazie per tutte le volte che mi sfotti quando mi prendo troppo sul serio e per le corsette che ci siamo fatti l’estate scorsa, quando torno vedrai che ti faccio mangiare la polvere!

Nonna, grazie per tutto il tempo che abbiamo passato insieme. So che per te è dura sapermi lontano, ma sappi che il mondo di oggi è davvero piccolo e ti posso venire a trovare quando meno te lo aspetti.

Grazie ai ragazzi di Biltstraat 196, la mia nuova famiglia qui ad Utrecht. Grazie per i momenti spensierati che abbiamo passato, e che passeremo insieme, tra una partita a biliardo, un film in salotto, le gite in giro per l’Olanda e le super cene!

Paola, a te va il “grazie” più grande. Forse te lo avrei dovuto dire più spesso, tempo fa... mi hai sopportato per dieci anni e più, abbiamo combattuto tante battaglie assieme e gran parte le abbiamo vinte; poi le nostre strade si sono divise e non festeggeremo assieme anche questo traguardo. Non so se le nostre strade si incontreranno un giorno, ma lo spero... ti auguro il meglio, convinto che quel meglio tu lo raggiunga per la forza che dimostri ogni giorno. Se oggi sono qui a difendere questa tesi è anche (tanto) merito tuo, che sei importante nella mia vita sia come persona sia come collega. Grazie per questi anni!

Acknowledgments

When I was a kid my ambitions were to buy a Ferrari and to become an astronaut or a scientist...

Well, today, in 2018, I have a Citroen C4, 2005 model, which I can't use since it's in Italy and a second hand bike I bought few month ago in a shop in Utrecht.

And, no, I'm not an astronaut, but at the end of this three years journey, I've become something similar to a scientist, and I'm saying similar because there is still a lot of things I have to learn.

These three years have been memorable, and they left a mark on me: the luggage becomes a sort of a part of your body because you are looking forward to go to a congress, somewhere in the world; you meet people from different countries but with your same passion. Finally, at least for me, you get aware that you're becoming an adult and there are duties that must be fulfilled.

Those years have been memorable also for the people I met,

A great "thank you" goes to Stefano Severe, "il Prof", who has been my mentor, always available to discuss about my project, with valuable suggestions.

In June 2015, at a congress in Milan, I had the pleasure to meet Ronald Wilders. Ronald have been of precious help during my PhD.

Thanks to Arie Verkerk who hosted me in his cardiac electrophysiology lab, together with Ronald, and who showed me things that I've just read in books.

Thanks to my new colleagues from the Medical Physiology department at the UMC in Utrecht. Thanks to Teun DeBoer, Mark Vos and Marcel van der Heyden that trusted me and let make me possible to start a new adventure and to finish my PhD journey. Thanks to Alex and Elise, my office mates, to all the PhD students and guys that are doing their internship, that make the working days more pleasant.

When you become a PhD student, the label "student" is still there, but you feel somehow to have moved on the other side. You feel it because you collaborate and discuss with people that were your teacher not so long time ago. Michelangelo, Claudia, Chiara, Enrico and Elisa you are that kind of people for me. Thanks for everything I learnt from you and I hope to keep learning.

Axel, working with you has been a pleasure, and I hope to have the chance to do it also in the future.

Yannick. I'm really glad to have met you! We really had good time during the summer in Italy! Thank you for being a super-nice host in Karlsruhe even though you had super busy days for your master thesis!

Madda, Jo, Paola, we are "i 4 dell'Ave Maria"! We started and we are going to finish together this adventure. Days in via Cavalcavia would have been tougher without you. I can not forget to mention Claudio, (Fabbri Junior!) who has a prize entitled with his name thanks to his (bad) jokes!

Valeria, Giulia, you also became a part of via Cavalcavia and it was nice to know you better day by day.

Simone, you entered the office as a student and you left it as a friend! We shared the burden of writing down the thesis and we had much fun playing five-a-side football!

Danilo, Simone Moretti, Alex, Paglio, Bob, Ahmed, Chiara and Andrea,—“the Apice people—, Marilisa, Cresc, Cinzia, Giulia, Michele, “the electronics guys”. Without you lunch time is not the same. Everyday we talk about funny things, mainly nerd things, and we try to steal from Claudio the “Claudio prize” for the worst joke.

Cri, Sara, you are a landmark and it's nice to talk with you about inside and outside university topics.

Maurizio, the LIB keeper, thanks for your help and for the chats about Formula 1!

Thanks to Sonia, Roberto, Alex and Marina for all the packages you picked up and for your kindness.

Alice, I put my trust in you, you are a friend. You saw me in bad days, in days I have lost myself; you always gave me your honest opinion and not just what I wanted to hear. I'm grateful for that!

Mum, Dad, thanks! You saw me growing up. Often sat down in front of a desk. Studying demands commitment and dedication and you always have been aware of it. Thanks for your support.

Luca, “Bro”, thanks for everytime you make joke of me when I take myself too seriously. Thanks also for the runs we did last summer; when I’ll be back you’ll bite the dust!

Grandma, thanks for the time we spent together. I know it’s hard for you that I’m living faraway now, but it’s a small world and I can come to visit you when you don’t expect it!

Thanks to the “Biltsraat people”, my new family here in Utrecht. Thanks for the funny moments we had, and we will have, between a pool table game, a movie in the leaving room, the journeys around Netherlands and for the super dinners!

Paola, the biggest “thanks” is for you! I should have told you it more often... You “have been standing” me for more than ten years; we fought many clashes side by side and we won most of them. Then our path divided us and we won’t celebrate together this achievement. I don’t know if our paths will join again one day, but I hope so...

I wish you all the best, because I’m sure you can achieve everything you want thanks to the strength you show everyday. If I’m here defending my PhD, it also because of you.

You are important in my life both as a person and as a colleague. Thanks for all these years!

